

Nanocomposites for Engineering Applications

Guest Editors: Alan K. T. Lau, Debes Bhattacharyya,
and Carrie H. Y. Ling





Nanocomposites for Engineering Applications

Journal of Nanomaterials

Nanocomposites for Engineering Applications

Guest Editors: Alan K. T. Lau, Debes Bhattacharyya,
and Carrie H. Y. Ling



Copyright © 2008 Hindawi Publishing Corporation. All rights reserved.

This is a special issue published in volume 2008 of “Journal of Nanomaterials.” All articles are open access articles distributed under the Creative Commons Attribution License, which permits unrestricted use, distribution, and reproduction in any medium, provided the original work is properly cited.

Editor-in-Chief

Michael Z. Hu, Oak Ridge National Laboratory, USA

Advisory Board

James H. Adair, USA
C. Jeffrey Brinker, USA
Taeghwan Hyeon, Korea
Nathan Lewis, USA

Ed Ma, USA
Alon V. McCormick, USA
Gary L. Messing, USA
Zhonglin Wang, USA

Enge Wang, China
N. Xu, China
Jackie Ying, USA

Associate Editors

Alan K. T. Lau, Hong Kong
Xuedong Bai, China
Donald A. Bansleben, USA
Theodorian Borca-Tasciuc, USA
Christian Brosseau, France
Siu Wai Chan, USA
Sang-Hee Cho, South Korea
Chun Xiang Cui, China
Ali Eftekhari, Iran
Claude Estournes, France
Alan Fuchs, USA
Lian Gao, China
Hong cheng Gu, China
Michael Harris, USA

Justin Holmes, Ireland
David Hui, USA
Wanqin Jin, China
Rakesh K. Joshi, USA
Do Kyung Kim, South Korea
Burtrand I. Lee, USA
Jun Li, Singapore
Shijun Liao, China
Gong-Ru Lin, Taiwan
J. -Y. Liu, USA
Jun Liu, USA
Songwei Lu, USA
Sanjay Mathur, Germany
Nobuhiro Matsushita, Japan

Sherine Obare, USA
P. Panine, France
Donglu Shi, USA
Bohua Sun, South Africa
Maryam Tabrizian, Canada
Theodore T. Tsotsis, USA
Y. Wang, USA
Xiaogong Wang, China
Michael S. Wong, USA
Ching Ping Wong, USA
Ping Xiao, UK
Zhi-Li Xiao, USA
Doron Yadlovker, Israel
Kui Yu, Canada

Contents

Nanocomposites for Engineering Applications, Alan K. T. Lau, Debes Bhattacharyya, and Carrie H. Y. Ling
Volume 2009, Article ID 140586, 1 page

Electric and Adsorption Characteristics of Nanocrystalline V-(N, He) Coatings, Alexey G. Guglya, Viktor G. Kolobrodov, and Ruslan L. Vasilenko
Volume 2009, Article ID 912676, 6 pages

The Effect of Nanosized Carbon Black on the Physical and Thermomechanical Properties of Al_2O_3 -SiC-SiO₂-C Composite, Mohamad Hassan Amin, Mohsen Amin- Ebrahimabadi, and Mohamad Reza Rahimpour
Volume 2009, Article ID 325674, 5 pages

Nanosize Copper Dispersed Ionic Liquids As an Electrolyte of New Dye-Sensitized Solar Cells, Fu-Lin Chen, I.-Wen Sun, H. Paul Wang, and C.-H. Huang
Volume 2009, Article ID 472950, 4 pages

Applications of Cu@C Nanoparticles in New Dye-Sensitized Solar Cells, Chang-Yu Liao, H. Paul Wang, F.-L. Chen, C.-H. Huang, and Y. Fukushima
Volume 2009, Article ID 698501, 4 pages

Sensing of Ethanol with Nanosize Fe-ZnO Thin Films, G.-H. Kuo, H. Paul Wang, H. H. Hsu, James Wang, Y. M. Chiu, C.-J. G. Jou, T. F. Hsu, and F.-L. Chen
Volume 2009, Article ID 316035, 3 pages

Surface Enamel Remineralization: Biomimetic Apatite Nanocrystals and Fluoride Ions Different Effects, Norberto Roveri, Elisa Battistella, Claudia Letizia Bianchi, Ismaela Foltran, Elisabetta Foresti, Michele Iafisco, Marco Lelli, Alberto Naldoni, Barbara Palazzo, and Lia Rimondini
Volume 2009, Article ID 746383, 9 pages

Fabrication and Transport Properties of Manganite-Polyacrylamide-Based Composites, Viorel Sandu, Stelian Popa, Ion Ivan, Carmen Plapcianu, Elena Sandu, Camelia Mihailescu, and Florica Doroftei
Volume 2009, Article ID 429430, 5 pages

Antibacterial Properties of Nanosilver PLLA Fibrous Membranes, Lin Li, Yi Li, Jiashen Li, Lei Yao, Arthur F. T. Mak, Frank Ko, and Ling Qin
Volume 2009, Article ID 168041, 5 pages

Fracture Toughness of Vapor Grown Carbon Nanofiber-Reinforced Polyethylene Composites, A. R. Adhikari, E. Partida, T. W. Petty, R. Jones, K. Lozano, and C. Guerrero
Volume 2009, Article ID 101870, 6 pages

Processing and Structure of Carbon Nanofiber Paper, Zhongfu Zhao, Jihua Gou, and Aurangzeb Khan
Volume 2009, Article ID 325769, 7 pages

Bulk Behavior of Ball Milled AA2124 Nanostructured Powders Reinforced with TiC, Hanadi G. Salem, Sherif El-Eskandarany, Amr Kandil, and Hassan Abdul Fattah
Volume 2009, Article ID 479185, 12 pages

Editorial

Nanocomposites for Engineering Applications

Alan K. T. Lau,¹ Debes Bhattacharyya,² and Carrie H. Y. Ling³

¹ Department of Mechanical Engineering, The Hong Kong Polytechnic University, Hong Kong

² Department of Mechanical Engineering, Centre for Advanced Composite Materials, The University of Auckland, Auckland 1142, New Zealand

³ Department of Mechanical Engineering, Stanford University, Stanford, CA 94305, USA

Correspondence should be addressed to Alan K. T. Lau, mmktlau@polyu.edu.hk

Received 16 July 2009; Accepted 16 July 2009

Copyright © 2009 Alan K. T. Lau et al. This is an open access article distributed under the Creative Commons Attribution License, which permits unrestricted use, distribution, and reproduction in any medium, provided the original work is properly cited.

Advanced polymer-based nanocomposite materials have gained popularity for wide engineering applications with improving virtually all types of products and commercialization of products that exploit their unique mechanical, thermal, and electrical properties. However, these properties present new challenges to understand, predict, and manage potential adverse effects, such as toxicity impacts exposure to human lives and environment. Thus, widespread applications of nanomaterials induce enormous potentials positively and negatively for human exposure and environmental release. Federal budget also emphasizes these implications and it is expected that the total annual budget for various sectors from the National Nanotechnology Initiatives will increase substantially in the coming years.

The applications of nanostructure resins for biological applications have been conducted in vitro and in vivo environments in research in the past few years. The evaluation involved how the resins can bond for biocompatibility to bone for repair after breaking, teeth for filling, other various types of tissues for wound healing, and so on. Natural and synthetic polymeric materials have been found to be suitable for tissue engineering applications. For an example, silk (like cocoon or spider) fiber /biodegradable polymer biocomposites have been used for tissue engineering (scaffolding) for bone repair. Many researches have also demonstrated the use of nano structural materials as reinforcements, such as nano apatite, nanoclay, and nanofibers (polymer-based or carbon nanotubes) to enhance the mechanical properties and thermal stability of bio compatible polymers for artificial joints and scaffolding. Tissue engineering is one such aspect that utilizes both engineering and life science disciplines to either maintain existing tissue structures or to enable tissue

growth. Furthermore, tissue-engineered organs can be used in testing procedures, reducing or eliminating the need for animal subjects. Nano biotechnology is an interdisciplinary field resulting from the interfaces between biotechnology, materials science, and nanotechnology.

This special issue “Nanocomposites for Engineering Applications” covers a wide range of papers contributed by authors around the world on the nanocomposites and their structural and mechanical properties. This aim is to provide a platform for scientists and researchers to exchange and share ideas and findings in the field.

*Alan K. T. Lau
Debes Bhattacharyya
Carrie H. Y. Ling*

Acknowledgments

The editors would like to express their sincere appreciation and thanks to all the authors and co authors for their scientific contribution to this special issue. We convey our gratitude to all the reviewers for their time and dedication.

Research Article

Electric and Adsorption Characteristics of Nanocrystalline V-(N, He) Coatings

Alexey G. Guglya, Viktor G. Kolobrodov, and Ruslan L. Vasilenko

NSC Kharkov Institute of Physics and Technology, National Academy of Sciences of Ukraine, 1, Akademicheskaya Street, 61108 Kharkov, Ukraine

Correspondence should be addressed to Alexey G. Guglya, guglya@kipt.kharkov.ua

Received 17 June 2008; Accepted 22 January 2009

Recommended by Alan K. T. Lau

This paper studies the structure, temperature dependences of electric resistance, and adsorption properties of nanoporous three-component V-(N, He) coatings. The coatings were produced using the technique of ion beam assisted deposition, in particular, deposition of vanadium onto a titanium substrate simultaneously bombarding it with $N_2 + He$ ions of 30 keV. It is shown, in contrast to V-N composites that have negative TCR (temperature coefficient of resistance), that the V-(N, He) coatings have negative TCR only in the temperature range of 250 to 350°C. A specific surface of pores and adsorption characteristics of V-(N, He) composites depend on preliminary treatment of a titanium surface. A coating deposited onto an untreated substrate has specific surface of 25.5 m²/g. The preliminary irradiation of titanium with $N_2 + He$ beam up to a dose of 6×10^{17} ion/cm² provides the increase in surface area up to 57.6 m²/g. The preliminary ion bombardment provides a considerable increase in hydrogen adsorption capacity of coatings. Especially, such impact is noticeable at the room temperature, when the amount of hydrogen absorbed by a coating that was applied onto a treated surface is more than three times of that absorbed by a coating that was deposited onto nonexposed titanium.

Copyright © 2009 Alexey G. Guglya et al. This is an open access article distributed under the Creative Commons Attribution License, which permits unrestricted use, distribution, and reproduction in any medium, provided the original work is properly cited.

1. Introduction

Presently scientists believe that solid-state hydrogen storage devices used for the vehicles should have high net capacity, short fueling time and low desorption temperature. In this regard proper consideration is given to metal hydrides and chemical hydrides that are used for these purposes though have definite drawbacks due to properties degradation, heavy weight and problems of waste disposal.

Alongside with hydride candidates for hydrogen storage much attention is given to highly porous structures, in particular, carbon-based nanomaterials, fullerenes, glass microspheres and powder materials. Besides, the microporous structures can be created in a form of coatings using plasma technique.

Actually, the presence of a gas component within a deposited flow and a high degree of process nonequilibrium are required to form a porous coating. It was shown recently [1, 2] that in case of ion beam assisted deposition the

composites with low phase formation Gibbs energy have nanocrystalline structure whose intercrystal space is filled with nanopores. It has also been established that such (VN) structures have high heat-resistance and can withstand temperatures up to 500°C and these are not subjected to blister formation at irradiation with helium ions whose dose amounts to 2×10^{17} ions/cm² [3]. Moreover, such type of treatment provides transformation of a closed porosity into the open one.

On the other hand, many papers are available that study the hydrogen behavior in materials suitable for the first wall of thermonuclear reactor [4–7]. In particular it was established that presence of admixtures in a form of soluble gases within a crystal lattice of structural materials creates conditions for hydrogen capture. The bonding energy, for example for C–H pair reaches 2.8 eV [7]. In addition it was shown that helium contained in such materials, especially in the form of vacancy $He_n V_m$ clusters, also forms a network of active hydrogen bonding centers [8–10].

Thus, the above analysis shows that the fine-dispersed admixtures that are present in a coating in the form of soluble and insoluble gases can create in combination with open nanoporosity the conditions for capturing the hydrogen in large amounts.

The purpose of this research is to obtain a porous nanocrystalline vanadium nitride-based coating, to study its structure, electrophysical characteristics, and hydrogen adsorption capacity.

2. Experimental Technique

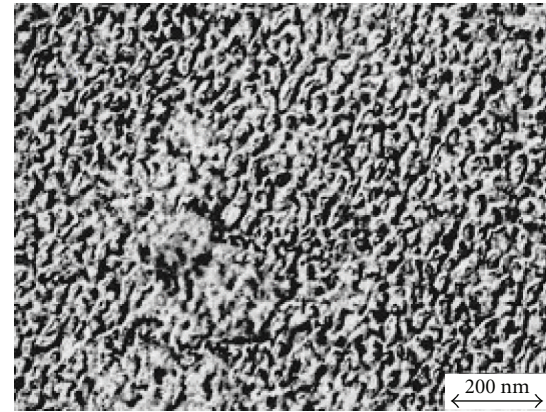
The coatings were created using ion beam assisted deposition plant ARGO-1 [11]. Vanadium was evaporated from electron beam module onto NaCl monocrystals and onto titanium foil substrate $100\ \mu\text{m}$ thick. The films were deposited at simultaneous bombardment with nitrogen and helium ions of 30 keV at gas components ratio 1:1. The ion current density was 1×10^{14} ion/cm² · s. The substrate temperature was 300°C. The metal evaporation rate was controlled using quartz resonator removed from an ion bombardment zone and it was equal to 0.1–0.15 nm/s. The coatings were 100 nm thick. The resistance was controlled continuously at depositing the coatings and at their further annealing. A coating structure was studied using the electron microscope JEM-100CX.

Prior to applying a coating in order to create vacancy porosity in titanium foil it was bombarded with N₂ + He ions of the same energy in a dose of up to 6×10^{17} ions/cm² at 300°C. A specific surface of the pores was measured using the method described in paper [12]. The interaction of hydrogen with a studied material was investigated through measurement of isochors adsorption. A dosed amount of hydrogen was injected from a calibrated capacity into a chamber and dependence of P on T was measured for each fixed amount of gas released into the chamber.

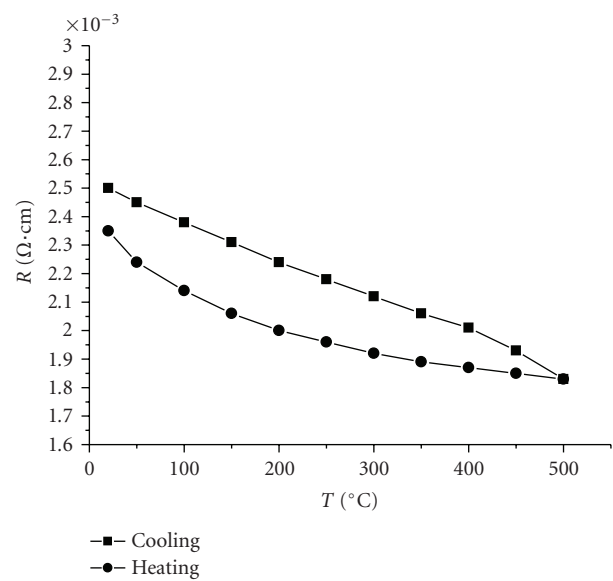
3. Research Results and Discussion

The studies of the initial stage of formation of VN composites including temperature coefficient of resistance (TCR) [1, 13] showed that the state of their grain boundary as well as TCR sign depend on Gibbs energy value of a given nitride. The Gibbs energy for vanadium nitride is equal to 70 cal/mol [14]. As a result the formation of the given nitride is accompanied by the formation of an ample amount of intercrystal nanopores (Figure 1(a)). The formed nanopores lead to the increase in specific resistance of a nitride and to the appearance of a hopping mechanism of conductivity and as a result of a negative TCR value (Figure 1(b)).

The structure of vanadium films that were deposited at bombardment with mixed N₂ + He beam differs from that shown in Figure 1(a). As a result fcc VN [13] structure formation also takes place. The main difference is that the addition of helium leads to the formation of the equiaxed and fine-dispersed porosity (Figure 2(a)). The average size of pores is equal to 15 nm, while the size of pores in vanadium nitride coatings is equal to 50 nm [1]. The pores in V-(N,



(a)



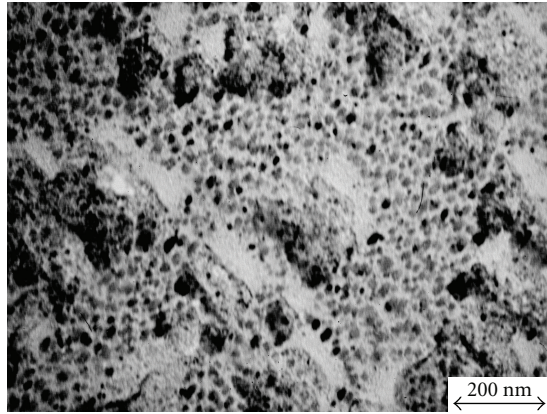
(b)

FIGURE 1: (a) Structure V-N composite; (b) resistivity as a function of temperature.

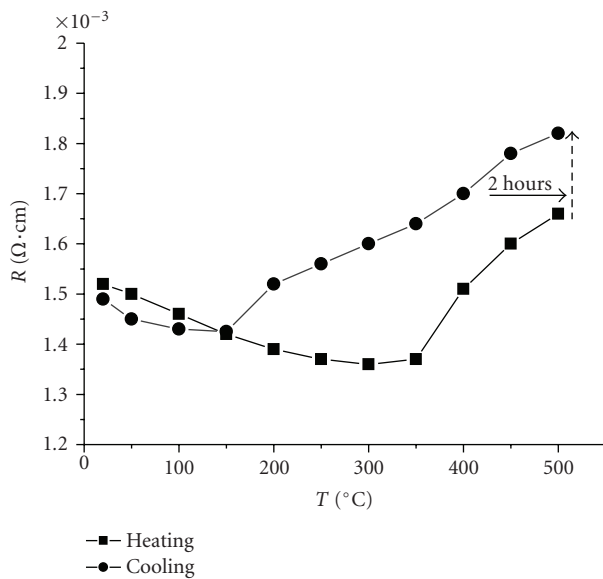
He) composite were evenly distributed across the material thickness.

The increase in the amount of equiaxed internal pores can be explained by presence of helium in a bombarding ion beam. The energy of helium migration in vanadium is not high. It is equal to 0.13 eV [15]. Due to this as the formation of coatings progresses helium leaves the volume of grains and accumulates in triple grain junctions. At the same time the implanted nitrogen will form a vanadium nitride VN_{1-x} lattice. The availability of pressure inside the gas-filled pores will define their equiaxiality.

Due to the high energy of bombarding gas ions the formation of a structure and phase composition of a coating has a double-stage character. At the stage of nucleation when the surface of grain nuclei contacts the deposited metal atoms the change in their sizes, distribution density and phase composition takes place. At the stage of coating growth whose thickness is within the depth of ion pass



(a)



(b)

FIGURE 2: (a) Structure V-(N, He) composite; (b) resistivity as a function of temperature.

(50 to 80 nm) the bombardment is continued and due to this the component composition of a composite also continues to change [16]. At the stage of growth of V-(N, He) coating the dangling bonds in a VN_{1-x} lattice are filled with nitrogen. The helium implanted at vanadium deposition leads to the increase in concentration of gas components in the pores and increases pressure in them.

The availability of gas pores in V-(N, He) also leads to the change in dependences of a value of electric resistance on annealing temperature (Figure 2(b)) in comparison with the analogous curves for V-N (Figure 1(b)). A special interest presents the change of TCR sign in the temperature range of 250 to 350°C. A two-hour annealing at 500°C increases the specific resistance in contrast to V-N composite. However, at cooling this value returns to the initial one. The electron microscopic study revealed no changes in the material structure. On the other part the change in TCR sign can be

explained by the change of electroconductivity mechanism in the studied temperature range.

A hopping mechanism of conductivity prevails in a VN_{1-x} composite that contains vacancy or near-vacancy pores. In this case the rise in temperature leads to the reduction of electron barriers and to the decrease in electric resistance of materials. As soon as the pores are filled with helium the rise in temperature will inevitably lead to the increase in gas pressure. The pores of ~15 nm can be described as “imperfect.” The relation between a pore radius “ r ” and pressure “ P ” in a pore can be described by the expression (see [17])

$$P = \frac{\mu b}{r} + \frac{2\gamma}{r}, \quad (1)$$

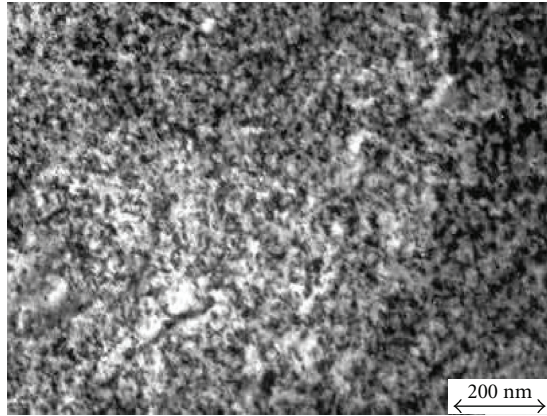
where μ is a shear modulus, b is a Burgers vector, and γ is a surface energy.

The calculations based on the results of our previous work [11] show that at depositing the V-(N, He) coating approximately 10 at.% of helium are implanted in its lattice. Actually in the long run all helium is condensed in the pores and therefore the internal pressure may reach 10^3 - 10^4 MPa. At annealing with increase in temperature up to 500°C the pressure may increase 3 times in comparison with that at a room temperature [17, 18]. Such increase in pressure will inevitably lead to the increase in stress in the area adjacent to a pore and to the increase in specific electric resistance of a material on the whole, which we observed in our experiments.

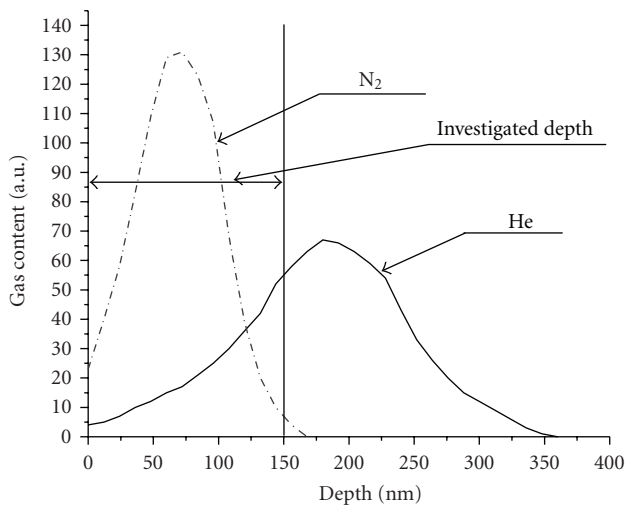
The measurement data showed that specific adsorption surface of studied samples was equal to 25.5 m²/g for a coating deposited onto unirradiated titanium substrate (sample No1). The specific surface of a coating deposited onto irradiated titanium substrate was 57.6 m²/g (sample No2).

A phase composition of a titanium foil that was subjected to a preliminary bombardment with $\text{N}_2 + \text{He}$ ion beam is a titanium nitride (TiN_{1-x}). A crystalline lattice contains equispaced defective areas that have a dark contrast (Figure 3(a)). It is assumed that these areas have helium vacancy clusters of a small size (He_nV_m , $n, m = 2-10$). Figure 3(b) shows the simulated curves of distribution of the implanted nitrogen and helium ions. The estimated level of damages in the investigated area is ~20 dpa [19].

Figure 4(b) shows experimental P - T dependences at differed hydrogen inlet doses for a sample No1. For the sake of comparison Figure 4(a) shows the analogous dependences for a titanium substrate in its initial state. The P - T plots are characterized by availability of inflection points for all lines of titanium substrate with a coating and without it. It is seen that at interaction of hydrogen with a titanium substrate the temperature at which two straight lines are intersected for each curve is not dependent on pressure value (Figure 4(a)). For substrates with a coating the slope of curves changes at 200°C (Figure 4(b)) in case of low pressure (≈ 0.1 MPa). With increase of pressure in the chamber the intersection points shift to the area of lower temperatures. From our point of view the presence of an intersection point on P - T line implies the change in interaction mechanism of hydrogen



(a)



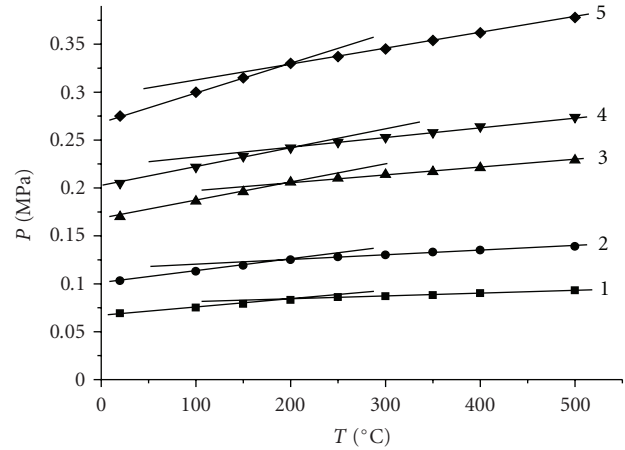
(b)

FIGURE 3: (a) Titanium structure irradiated by $N_2 + He$ ions; (b) nitrogen and helium distribution.

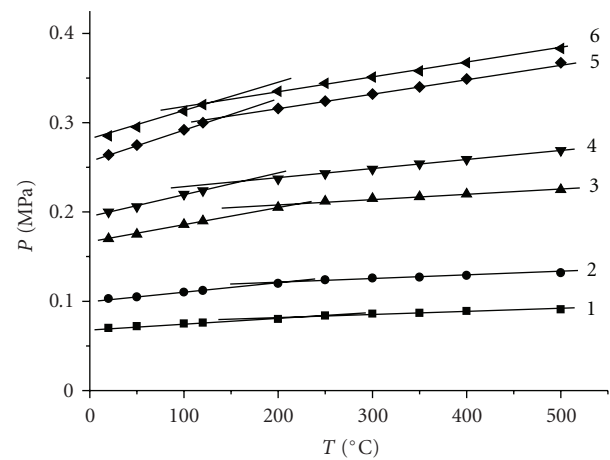
and studied material. Possibly, the titanium and porous film structure absorb hydrogen in small amounts at the initial section of curves. Further this absorption is intensified and this can be caused by onset of hydride formation in the intermetallic phase of compounds. The attention should be paid to the fact that with increase in pressure the angle between two straight-line sections of the P - T lines becomes larger and it means that the pressure produces definite impact on formation of these compounds.

Proceed from the P - T dependences the isotherms of hydrogen absorption by the samples No1 and No2 (Figures 5(a) and 5(b)) can be easily calculated. In the studied temperature and pressure ranges the hydrogen strictly obeys the ideal gas laws. For the sake of comparison of different measurement data the value of absorbed hydrogen was reduced to ncm^3/g , that is, to the volume of hydrogen at normal conditions ($P = 760 \text{ mm Hg}$, $T = 0^\circ C$).

The figures show that the porous structure plays main role at $20^\circ C$. With increase in pressure up to $\approx 0.175 \text{ MPa}$



(a)



(b)

FIGURE 4: Pressure in the chamber as a function of temperature for (a) Ti; (b) Ti with V-(N, He) coating for different quantity of hydrogen injection: 1– 38.6 ncm^3 ; 2– 57.9 ncm^3 ; 3– 95.5 ncm^3 ; 4– 112.3 ncm^3 ; 5– 155.7 ncm^3 ; 6– 185.2 ncm^3 .

the increase in absorption value is not significant, however at $\approx 0.275 \text{ MPa}$ the absorption rate is essentially increasing. At pressure of $\approx 0.3 \text{ MPa}$ the hydrogen absorption isotherms reach a saturation level. It should be noted that the isotherm of hydrogen absorption by the sample No2 reaches a saturation level at absorption value that exceeds that for sample No1 actually by factor of 2. The isotherms of hydrogen absorption by the samples No 1 and 2 are characterized by a higher degree of absorption at temperatures of $300^\circ C$ and $500^\circ C$ in comparison with $20^\circ C$ in the whole pressure interval and the rate of growth of absorption value is increasing in the interval of $0.1 \dots 0.125 \text{ MPa}$. The increase in the rate of growth is more pronounced for the sample No2 that has a larger specific surface.

The obtained data show that the active hydrogen accumulators are the result of the porosity of the coating obtained through the ion beam assisted deposition but also that preliminary created by ion implantation. In addition it should be noted that the activity of the preliminary

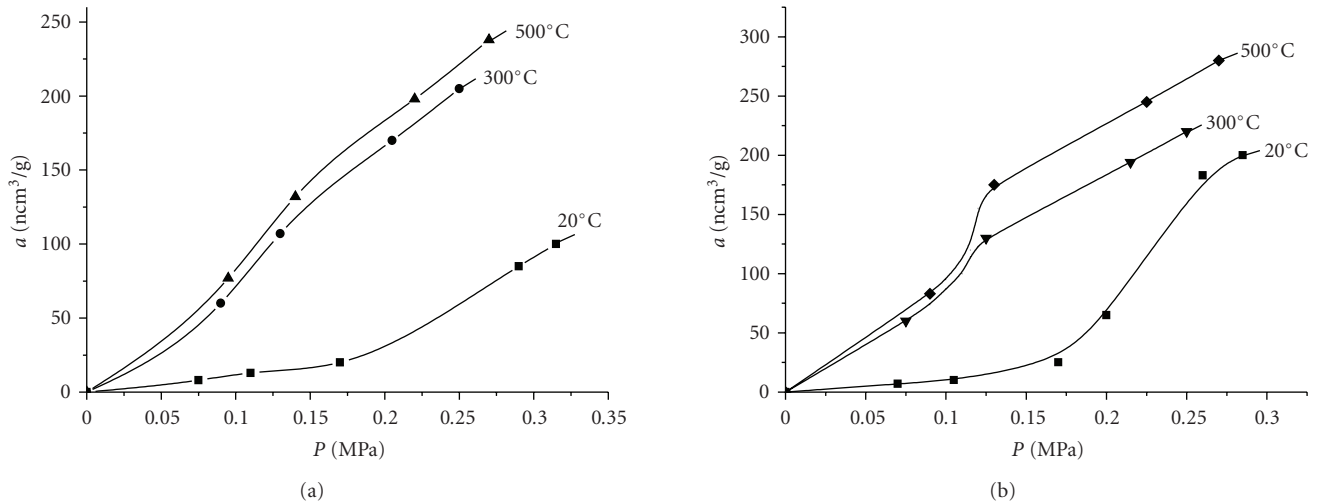


FIGURE 5: Isotherms of hydrogen adsorption of V-(N, He) coatings on titanium substrate: (a) not irradiated previously, (b) irradiated.

created porosity depends both on the hydrogen temperature and pressure. At low temperatures the implantation based porosity contributes more to hydrogen absorption than at high temperatures (compare Figures 5(a) and 5(b)).

For the comparison the absorption of hydrogen by a titanium substrate at hydrogen pressure of 0.25 MPa is no more than 4.4 ncm³/g. It is seen that the hydrogen-related activity of titanium is much lower in comparison with that of the created porous structures. This means that the porosity of a coating and substrate play a key role in absorption of hydrogen at a room temperature. At a higher temperature the increase in the hydrogen absorption may take place due to two factors, in particular, hydride formation in the intermetallide TiV phases and hydrogen capture with nitride traps that were formed during ion beam assisted deposition of coatings.

4. Conclusions

The results of the research show that the ion beam assisted deposition can be used to obtain nanostructural porous structures. The bombardment of the deposited vanadium coating with the mixed beam of nitrogen and helium ions stimulates the formation of nitride phases whose intercrystal spaces contain equiaxial pores. It is quite possible that the volume of pores is occupied by the helium-vacancy clusters. The electric resistance of such materials exceeds that of powder vanadium nitrides by factor of 10. A sign of the temperature coefficient of resistance changes from a negative to the positive one in the temperature range of 250 to 350°C.

The results of adsorption studies showed that the obtained structures have a rather developed specific surface. It has been established that the main contribution to the process of hydrogen storage at low temperatures is made by the created porous structure. At elevated temperatures the absorption capacity of the intermetallide and nitride phases may increase. The preliminary ion bombardment with the mixed N₂ + He beam contributes to the formation of a surface

porous layer which is an additional factor contributing to the increase in the adsorption capacity of porous materials.

References

- [1] A. G. Guglya, *Nanocrystalline Cr-N and V-N coatings. The receiving and investigation*, Doctoral thesis, Kharkov Institute of Physics and Technology, Kharkov, Ukraine, 2006.
- [2] A. G. Guglya, "Electrophysical and structural and phase characteristics of thin-film composites Cr-N and V-N," *The Journal of Kharkov National University*, vol. 664, no. 2(27), pp. 73–78, 2005 (Russian).
- [3] A. G. Guglya, I. Neklyudov, and R. Vasilenko, "Effect of helium ion irradiation on the structure and electrical resistivity of nanocrystalline Cr-N and V-N coatings," *Radiation Effects and Defects in Solids*, vol. 162, no. 9, pp. 643–649, 2007.
- [4] S. K. Erements, "Deuterium trapping in low-Z coatings," *Journal of Nuclear Materials*, vol. 111–112, pp. 590–597, 1982.
- [5] K. Saiki, H. Tanaka, and S. Tanaka, "Surface composition change of TiC and SiC under hydrogen ion bombardment," *Journal of Nuclear Materials*, vol. 128–129, pp. 744–748, 1984.
- [6] K. L. Wilson and A. E. Pontau, "Deuterium trapping and release in titanium-based coatings for TFTR," *Journal of Nuclear Materials*, vol. 93–94, part 2, pp. 569–574, 1980.
- [7] K. Sato, S. Yamaguchi, Y. Fujino, et al., "Deuterium retention in TiC crystals prepared by chemical vapor deposition and floating zone methods," *Journal of Nuclear Materials*, vol. 128–129, pp. 698–702, 1984.
- [8] S. T. Picraux, J. Böttiger, and N. Rud, "Enhanced hydrogen trapping due to He ion damage," *Journal of Nuclear Materials*, vol. 63, no. 1, pp. 110–114, 1976.
- [9] A. E. Pontau, M. I. Baskes, K. L. Wilson, et al., "Deuterium retention in helium-damaged stainless steel: detrapping energy," *Journal of Nuclear Materials*, vol. 111–112, pp. 651–653, 1982.
- [10] R. Schulz, R. Benrisc, and B. M. Scherzer, "Trapping and mutual release of D and 3He in molybdenum," *Journal of Nuclear Materials*, vol. 93–94, part 2, pp. 608–616, 1980.
- [11] A. G. Guglya, I. G. Marchenko, D. G. Malykhin, and I. M. Neklyudov, "Production of Cr-N films by ion beam-assisted deposition technology: experiment and computer

- simulation,” *Surface and Coatings Technology*, vol. 163-164, pp. 286–292, 2003.
- [12] S. J. Gregg and K. S. W. Sing, *Adsorption, Surface Area, and Porosity*, Academic Press, London, UK, 1967.
- [13] R. Vasilenko, A. G. Guglya, and M. Litvinenko, “The influence of treatment on conductivity V-N films, received during high energy nitrogen ion bombardment,” *Metalofisika i Noveishie Tehnologii*, vol. 28, no. 9, pp. 1167–1176, 2006 (Russian).
- [14] Y. Baba and T. A. Sasaki, “Nitride formation at metal surfaces by Ar⁺ ion bombardment in nitrogen atmosphere,” *Materials Science & Engineering A*, vol. 115, pp. 203–207, 1989.
- [15] W. D. Wilson and R. A. Jonson, *Interatomic Potentials and Simulation of Lattice Defects*, Plenum Press, London, UK, 1972.
- [16] V. I. Bendikov, A. G. Guglya, I. G. Marchenko, D. G. Malykhin, and I. M. Neklyudov, “Mechanisms of forming the Cr-N composite in the unsteady-state stage of ion beam-assisted deposition process,” *Vacuum*, vol. 70, no. 2-3, pp. 331–337, 2003.
- [17] H. Trinkaus, “Energetics and formation kinetics of helium bubbles in metals,” *Radiation Effects and Defects in Solids*, vol. 78, no. 1–4, pp. 189–211, 1982.
- [18] W. Jäger, R. Manzke, H. Trinkaus, R. Zeller, J. Fink, and G. Crecelius, “The density and pressure of helium in bubbles in metals,” *Radiation Effects and Defects in Solids*, vol. 78, no. 1–4, pp. 315–325, 1982.
- [19] J. F. Ziegler, J. P. Biersack, and K. Littmark, *The Stopping and Range of Ions in Matter*, Pergamon Press, New York, NY, USA, 1985.

Research Article

The Effect of Nanosized Carbon Black on the Physical and Thermomechanical Properties of $\text{Al}_2\text{O}_3\text{-SiC-SiO}_2\text{-C}$ Composite

Mohamad Hassan Amin, Mohsen Amin-Ebrahimabadi, and Mohamad Reza Rahimpour

Department of Ceramics, Materials and Energy Research Centre (MERC), Meshkin-Dasht Road, Karaj 3177983634, Iran

Correspondence should be addressed to Mohamad Hassan Amin, doctoramin@gmail.com

Received 24 September 2008; Accepted 22 January 2009

Recommended by Alan K. T. Lau

The effects of using nanosized carbon black in the range of 0–10 weight percentages on the physical and thermomechanical properties of $\text{Al}_2\text{O}_3\text{-SiC-SiO}_2\text{-graphite}$ refractory composites were investigated. Nanosized carbon black addition improved the relative heat resistance and oxidation resistance of composites. The bulk density of the composites is reduced with increasing carbon black (CB) content. Increase in CB content first causes an increase in the apparent porosity, but at more than 3 wt% amount of CB, a decrease of apparent porosity was observed. The cold crushing strength (CCS) increased with increasing CB content in samples fired at 800°C and in samples fired at 1500°C when the content is increased to 3 wt%, but the CCS decreased with increasing CB content in samples fired at 1500°C when the CB content was less than 3 wt%. The composite without CB exhibits the highest value of CCS at firing temperature of 1500°C .

Copyright © 2009 Mohamad Hassan Amin et al. This is an open access article distributed under the Creative Commons Attribution License, which permits unrestricted use, distribution, and reproduction in any medium, provided the original work is properly cited.

1. Introduction

$\text{Al}_2\text{O}_3\text{-SiC-SiO}_2$ refractory composites have been widely used as a castable refractory in several applications in the iron and steel making industry. However, Al_2O_3 -based castables have poor resistance to corrosion (especially in a basic slag environment) and spalling [1]. The growing demand and application of these castable materials encourage researchers and producers to investigate their physical, chemical, and thermomechanical properties.

The successful development of oxide carbon bricks in the 1970 s, by adding carbon to oxide brick formulations, suggested that introducing carbon (graphite) into current oxide based castables would give improved properties [1]. In recent years, one of the most significant trends in refractory technology has been associated to the development of carbon-containing refractory castables. $\text{Al}_2\text{O}_3\text{-SiC-SiO}_2\text{-C}$ refractory composites are commonly used in the iron and steel making industry, especially in blast furnace iron/slag runners. With the advent of quality steel making processes, it became essential to opt for good quality refractories, especially monolithic castables which

were suitable in the presence of molten slag and metal [2]. The use of graphite as a carbon source has many advantages in refractory applications [3]. It has a high melting point and promotes the improvement of the corrosion resistance of the refractory, mainly due to its lower wettability by metal and slag. Thermal shock resistance of the refractory is improved due to the low thermal expansion, high thermal conductivity, and low modulus of elasticity promoted by the graphite addition. On the other hand, these composites have a few disadvantages, such as oxidation of graphite and reduction of fracture strength and Young's modulus because of the presence of graphite flakes.

Recent research has revealed that replacing graphite flakes with nanocarbon powder such as in situ formation of nanofibres in the matrix of C-containing refractories can markedly improve the refractories properties and performance [4, 5]. In spite of these studies, the influence of nanosized carbon black on properties of $\text{Al}_2\text{O}_3\text{-SiC-SiO}_2\text{-graphite}$ refractory composites is not yet clearly understood. This will be addressed in the present paper by measuring behavior of a typical $\text{Al}_2\text{O}_3\text{-SiC-SiO}_2\text{-graphite}$ castable.

2. Experimental Procedure

Alumina–SiC–SiO₂–graphite refractory composites were obtained from a mixture of tabular alumina grains (Alfa-tab-30, Silkem, Slovenia), with grain sizes up to 5 mm, reactive alumina (PFR 20, Pechiney, France), silicon carbide (EC6-F220, Treibacher, Austria-Brazil), microsilica (971, Elkem Co., Norway). All composites contained 2 wt% natural Chinese flake graphite (Great Wall Group) with an average flake size of 100 μm, an ash content of 5 wt% and density of 2.26 gr/cm³. A modified Andreasen grain size distribution (Dinger and Funk) [6], with maximum grain size of 5 mm and modulus $n = 0.8$, was used for all the composites and the tabular alumina fractions were varied to obtain the specified grain size distribution. The composite mixed with amounts of 0, 1, 2, 3, 4, 5, 6, 7, 8, 9, and 10 wt% nanoparticles of carbon black (CB), with average size about 20 nm, and liquid phenolic Novalac resin was used as binder in amount of 0.1% weight also for all composites.

Raw materials were weighed (each batch 10 kg) and then dry mixed for 4 minutes in a Hobart mixer. After water addition, wet mixing was continued for another 4 minutes. The mixture was poured into the moulds of 50 mm × 50 mm × 50 mm without vibration. After demoulding, the samples were cured for 24 hours at room temperature and cured samples were dried at 110°C/18 h. Then, all compositions were heat-treated in a reducing atmosphere up to 1450°C for 5 hours to remove the volatile species and to minimize their influence.

Bulk density and apparent porosity of samples measured according to ASTM C20-97, and cold crushing strength (CCS) of the samples was measured according to ASTM C133-97.

Relative heat resistance was determined by the method according to [7]. In this method, prismatic samples are subjected to abrupt thermal cycling with heating to 850°C and cooling on water-cooled plate. After the chosen number of cycles, the samples are tested for bending strength. Relative heat resistance R_{rel} is evaluated by the formula

$$R_{rel} = \left[\frac{\sigma_F^{3C} (\sigma_F^{7C} + 0.1)}{\sigma_F} \right]^{1/2}, \quad (1)$$

where σ_F is ultimate bending strength after gradual roasting at 850°C, σ_F^{3C} is ultimate bending strength after three heating-cooling cycles, and σ_F^{7C} is ultimate bending strength after seven heating-cooling cycles. The values of σ_F , σ_F^{3C} and σ_F^{7C} were determined for three pairs of samples. Samples that withstood thermal cycling were tested for ultimate bending strength.

The samples were oxidized isothermally at 1500°C for 5 hours, in an electric furnace by natural convection of air and fraction of weight loss was calculated (Ox%) according to the equation:

$$Ox\% = \frac{I.C - R.C}{I.C} \times 100, \quad (2)$$

where I.C is the initial weight of carbon before oxidation, and R.C is the weight of residual carbon after complete

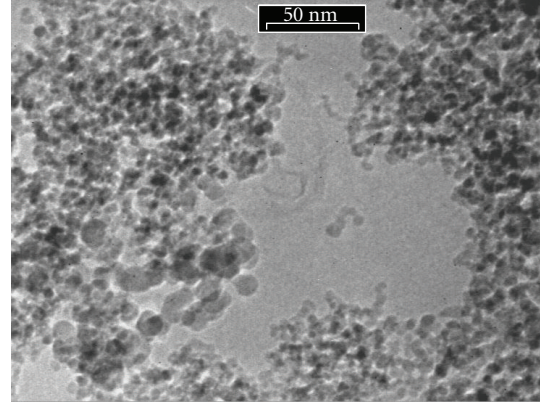


FIGURE 1: Typical electron micrographs of used CB.

oxidation. Carbon contents of samples were determined using the high-frequency combustion-infrared absorption method (CS-400, LECO). Observation of the microstructure was performed on polished faces using a scanning electron microscope or SEM (LEO-460) equipped with an energy dispersive spectroscopy (EDS) system (beryllium window). Transmission electron microscopy images were obtained using a Philips TEM operating at the voltage of 200 kV.

3. Results and Discussion

Figure 1 shows the transmission electron microscope (TEM) image of used CB. It is seen that nanoparticles are in spherical shape. Size measurement on the electron micrographs gave values in the range 5–30 nm, with an average size around 20 nm.

Figure 2 shows the dependence of the relative heat resistance of composites on amounts of CB as additive.

The results showed that the relative heat resistance of composites increased with the amount of carbon black. This can be correlated with the filling of pores and voids by CB particles beside gels; so that the structure of the castable is not compacted and stresses can be relaxed under the influence of heating cycles [7]. Castable without CB contains two sources of gel content, namely, alumina gel (the hydration product of hydratable alumina) and silica gel, which fills the pores and voids; however, castables containing CB show the higher relative heat resistance owing to the filling of pores and voids by CB particles beside gels, resulting in compact structure, because the large density difference between CB and oxide raw materials. This result is attributed to the ability of the compressible carbon phase to absorb the expansion of alumina grains. The probability of any cracks formed fails to propagate because of the grain mismatch and consequent poor bonding between CB and ceramic phase [3].

The above claim was confirmed by investigating the microstructure investigation, as shown in Figure 3. Figure 3(a) exhibits an SEM photomicrograph of a composite without CB additive. Some minor phases can be observed between the alumina grains. These phases have a tendency to occupy of porous. Figure 4 shows the typical elemental

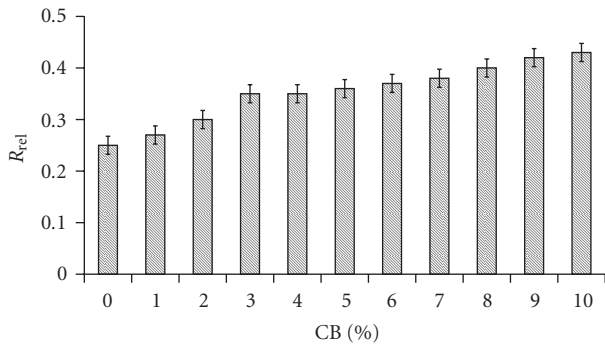
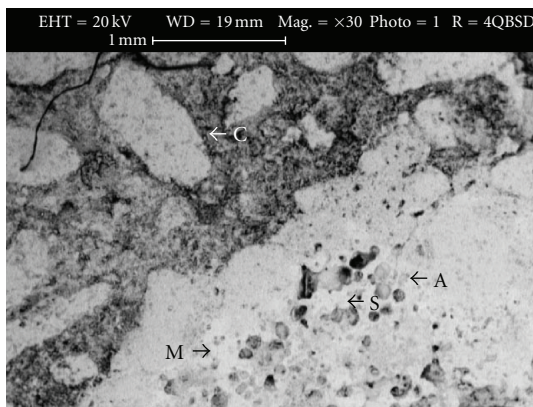
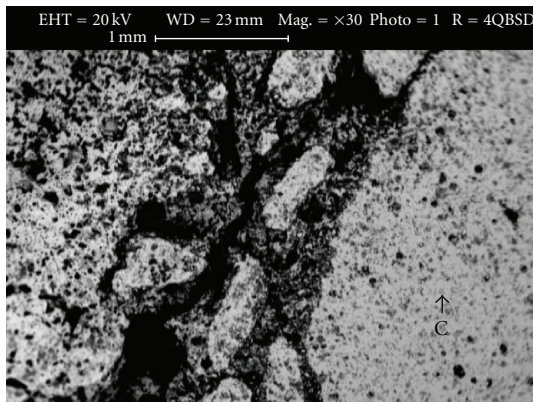


FIGURE 2: Dependence of the relative heat resistance of composites versus the amount of CB. Bars refer to standard deviation.



(a)



(b)

FIGURE 3: SEM micrographs of composites ($\times 30$), (a) sample without CB and (b) sample containing 7 wt% CB.

analysis patterns of these phases. EDS analysis of phases A and S confirms that these phases are based on alumina and silica, respectively, and phase M has similar stoichiometric composition of mullite. The Al and Si elements are not observed in the X-ray spectroscopy of the phases C in Figures 3(a) and 3(b). It is concluded that these phases are just based on carbon.

Figure 5 shows the effect of CB content on the composite's apparent porosity and density. As can be seen, the bulk density of the composites is reduced with increasing CB content in samples, due to the lower density of the CB compared with the density of the other components.

Increase in CB content first causes an increase in the apparent porosity, but at larger amounts of CB, a decrease of apparent porosity was observed. The porosity is reduced by the influence of CB addition, which improves the packing efficiency. On the other hand, the porosity is increased by the oxidation of carbon and CO and CO₂ gases exiting from the body in the low amount of CB; but gas pressure of CO evolved during C oxidation prevents further oxidation [8]. This claim was confirmed by the measuring of the amount of residual carbon in samples on weight percent of CB as additive, as shown in Figure 6.

Figure 6 shows the oxidation percentage and mass% change of the residual carbon content (R.C) of composite with CB addition after heating at 1500°C for 5 hours in natural air. For the sample without CB, the content graphite was almost completely oxidized; however, for the sample with CB, a large unoxidized zone was still observed. The enhancement of gas pressure was considered to occur by the oxidation of carbon turning to CO and CO₂. As a result, the pores were filled with condensed gases, and O₂ would be expected to diffuse only a short distance. Consequently, carbon reacted with oxygen just at the original carbon site or the pores nearby and oxidation of carbon was reduced. It is considered that the enhancement of gas pressure can effectively suppress the diffusion of oxygen into the refractories, and the oxidation rate was decreased. This result confirmed that the addition of CB effectively improved the oxidation resistance of the refractories.

When used in blast furnace iron/slag runners, refractory composite castables are subjected to a high impact of iron/slag melt during tapping of blast furnace. The effect of this phenomenon on the refractory lining of runners is crushing of the lining, especially at the impact area of the main trough and the tilting runner. Thus knowledge of crushing behaviour is very important to prevent structural spalling and extensive cracking. To establish how the CB content influences the cold crushing strength (CCS) of refractory composite castables, CCS was measured after heat treatment at 800°C and 1500°C.

Figure 7 shows the variation of CCS as a function of the CB content at different firing temperature. It can be seen that the CCS increased with increasing CB content in samples fired at 800°C, but in samples fired at 1500°C, an increase in CB content first causes a decrease in the CCS; however, when the content is increased to 3 wt%, the CCS increases gradually as the CB content increases.

Ceramic matrix composites fracture occurs by one of the following mechanisms, depending on the pore structure: catastrophic fracture in dense and tough specimens, with the formation of one or several transcrystallite cracks; stepped fracture in specimens with a high concentration of microcracks and pores, with the formation of numerous transcrystallite cracks; gradual slow fracture in specimens

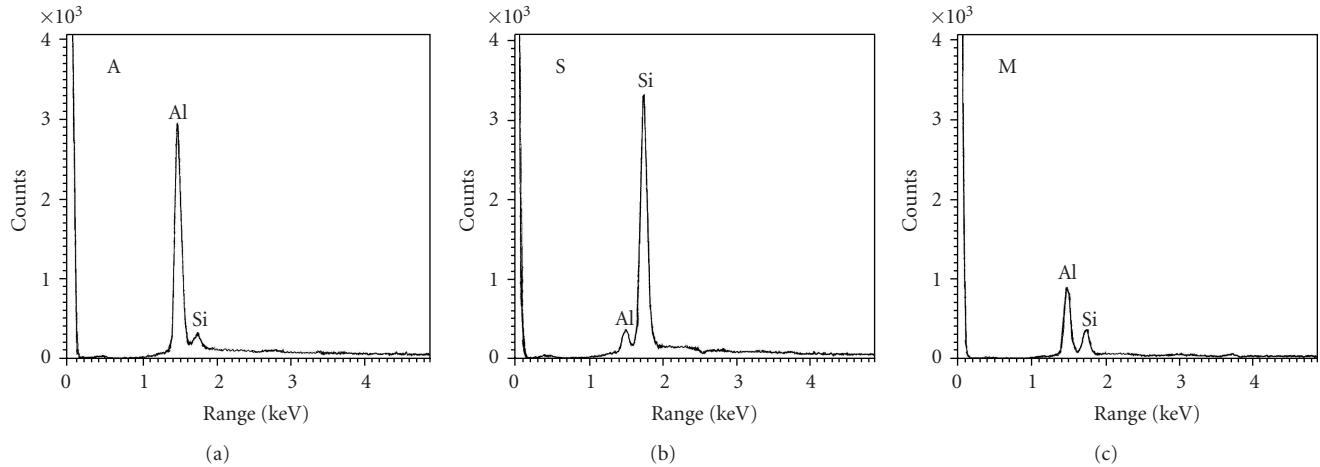


FIGURE 4: X-ray spectroscopy of the minor phases in Figure 2.

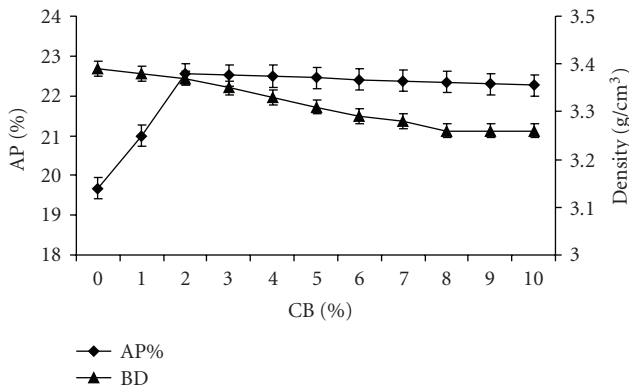


FIGURE 5: The effect of various amounts of CB on apparent porosity (AP) and bulk density (BD) of composite. Bars refer to standard deviation.

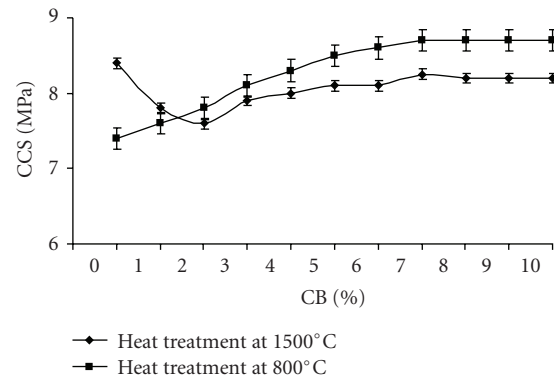


FIGURE 7: The CCS of composite versus CB% as additive after heat treatment at 800°C and 1500°C. Bars refer to standard deviation.

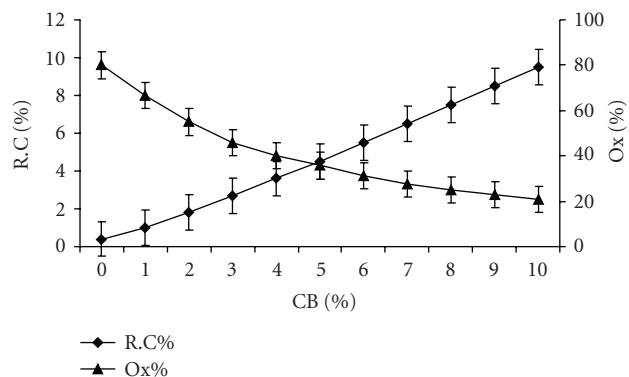


FIGURE 6: The residual carbon content (R.C) of composite (wt%) and Ox% versus CB% as additive. Bars refer to standard deviation.

with low strength. The formation of cracks on the surface of the castables depends on their composition.

The increase in CCS in samples fired at 800°C with CB% is almost linear, following a typical composite mixture rule. This can be correlated with the filling of pores and voids by

CB particle in castables containing CB (see Figure 3(b)). It seems that, in this situation, the ceramic matrix composites fracture occurs by gradual slow fracture in specimens with low strength. One of the reasons invoked to explain this effect is crack deflection along the nanosized carbon black particles, so the average stress intensity at its tip is reduced, because the stress is no longer always normal to the crack plane.

The composite without CB exhibits the highest value of CCS at firing temperature of 1500°C due to the formation of mullite phase (see Figure 3(a)) that causes the growth of elongated needle-shaped mullite crystals which strengthens the structure at high temperatures [9]. Because of the high reactivity of microsilica and reactive alumina, the formation of mullite phase occurs at temperatures above 1300°C, and the porosity is reduced so there is a significant amount of increase in CCS compared to specimens fired at 800°C.

Also, by comparing Figures 5 and 7, one can immediately see the correlation between the apparent porosity and CCS of specimens fired at 1500°C. Therefore, the variation of the CCS values of specimens fired at 1500°C can also be represented as function of the apparent porosity. Increase

in CB content of specimens fired at 1500°C, first causes an increase in the apparent porosity and, as a result, the CCS value decreased because fracture occurs by stepped fracture mechanism, with the formation of numerous transcrystallite cracks. But at a larger amount of CB, the CCS decreases with the increasing of CB%. The reason for this variation of the CCS values can be attributed to the decrease of porosity. Pores are usually quite deleterious to the strength of ceramics not only because they reduce the cross-sectional area over which the load is applied, but more importantly because they act as stress concentrators. Typically the strength and porosity have been related by following empirical relationship:

$$\sigma_p = \sigma_0 e^{-BP}, \quad (3)$$

where P , σ_p , and σ_0 are, respectively, the volume fraction porosity and the strength of the specimen with and without porosity; B is a constant that depends on the distribution and morphology of the pores [10].

4. Conclusions

Based on the above results, the following conclusions were drawn when nanosized carbon black was added as an additive to the Al_2O_3 -SiC-SiO₂-C refractory composites.

- (1) The relative heat resistance of composites increased with the amount of carbon black because in the presence of CB, the pores and voids were filled by CB particles beside gels, so that the structure of the castable is not compacted and stresses can be relaxed under the influence of heating cycles.
- (2) The bulk density of the composites is reduced with increasing CB content in samples due to the lower density of the CB compared with the density of the other components.
- (3) Increase in CB content first causes an increase in the apparent porosity, because of oxidation of carbon and exiting of CO and CO₂ gases from the body. At more than 3 wt% amount of CB, a decrease of apparent porosity was observed, because the addition of nanosized carbon black improves the oxidation resistance of Al_2O_3 -SiC-SiO₂-C refractory composites, and the pores were filled with CB.
- (4) The addition of CB effectively improved the oxidation resistance of the refractories, because CB plays a role as antioxidant.
- (5) The CCS increased with increasing CB content in samples fired at 800°C and in samples fired at 1500°C when the content is increased to 3 wt%, because the crack deflected along the nanosized carbon black particles, so the average stress intensity at its tip is reduced.
- (6) The composite without CB exhibits the highest value of CCS at firing temperature of 1500°C, due to the formation of mullite phase that causes the growth of elongated needle-shaped mullite crystals which strengthens the structure at high temperatures.
- (7) The CCS decreased with increasing CB content in samples fired at 1500°C when the CB content was less than 3 wt%, the reason for this variation of the CCS values can be attributed to the increasing of porosity.

References

- [1] S. Zhang and W. E. Lee, "Carbon containing castables: current status and future prospects," *British Ceramic Transactions*, vol. 101, no. 1, pp. 1–8, 2002.
- [2] S. Mukhopadhyay and P. K. Das Poddar, "Effect of preformed and in situ spinels on microstructure and properties of a low cement refractory castable," *Ceramics International*, vol. 30, no. 3, pp. 369–380, 2004.
- [3] E. M. M. Ewais, "Carbon based refractories," *Journal of the Ceramic Society of Japan*, vol. 112, no. 1310, pp. 517–532, 2004.
- [4] S. Tamura, T. Ochiai, S. Takanaga, T. Kanai, and H. Nakamura, "Nano-tech refractories—1. The development of the nano structural matrix," in *Proceedings of the Unified International Technical Conference on Refractories (UNITECR '03)*, pp. 517–520, Kyoto, Japan, October 2003.
- [5] N. Kido, K. Yamamoto, M. Kamiide, et al., "Carbon nanofiber—a new trial for magnesia based bricks," in *Proceedings of the Unified International Technical Conference on Refractories (UNITECR '03)*, pp. 264–267, Kyoto, Japan, October 2003.
- [6] J. E. Funk and D. R. Dinger, "Particle size control for high-solids castable refractories," *American Ceramic Society Bulletin*, vol. 73, no. 10, pp. 66–69, 1994.
- [7] N. M. Khalil, "Heat resistance and thermomechanical behaviour of ultralow and zero cement castables," *British Ceramic Transactions*, vol. 103, no. 1, pp. 37–41, 2004.
- [8] A. Yamaguchi, "Affects of oxygen and nitrogen partial pressure on stability of metal, carbide, nitride, and oxide in carbon-containing refractories," *Taikabutsu Overseas*, vol. 7, no. 1, pp. 4–13, 1987.
- [9] M. F. M. Zawrah and N. M. Khalil, "Effect of mullite formation on properties of refractory castables," *Ceramics International*, vol. 27, no. 6, pp. 689–694, 2001.
- [10] M. Barsoum, *Fundamentals of Ceramics*, McGraw-Hill, New York, NY, USA, 1997.

Research Article

Nanosize Copper Dispersed Ionic Liquids As an Electrolyte of New Dye-Sensitized Solar Cells

Fu-Lin Chen,¹ I.-Wen Sun,^{1,2} H. Paul Wang,^{2,3} and C.-H. Huang³

¹Department of Chemistry, National Cheng Kung University, Tainan City 701, Taiwan

²Sustainable Environment Research Center, National Cheng Kung University, Tainan City 701, Taiwan

³Department of Environmental Engineering, National Cheng Kung University, Tainan City 701, Taiwan

Correspondence should be addressed to H. Paul Wang, wanghp@mail.ncku.edu.tw

Received 6 October 2008; Accepted 22 January 2009

Recommended by Alan K. T. Lau

To enhance the electrical conductivity of the electrolyte for a newly developed dye-sensitized solar cell (DSSC), metallic copper (Cu) encapsulated within the carbon shell (Cu@C) nanoparticles dispersed in a room temperature ionic liquid (RTIL) (e.g., [bmim⁺][PF₆⁻]) has been studied in the present work. By the pulsed-field gradient spin-echo NMR method, the self-diffusion coefficients of cations and anions of the RTIL have been determined. The self-diffusion coefficient of the [bmim⁺] cations in the RTIL dispersed with 0.08% of Cu@C nanoparticles is increased by 35%. The electrical conductivity of the Cu@C dispersed RTIL is also increased by 65% (1.0 → 2.3 ms/cm). It is very clear the nanosize Cu@C dispersed RTIL with a relatively greater diffusion coefficient and electrical conductivity can be a very effective electrolyte especially utilized in DSSCs.

Copyright © 2009 Fu-Lin Chen et al. This is an open access article distributed under the Creative Commons Attribution License, which permits unrestricted use, distribution, and reproduction in any medium, provided the original work is properly cited.

1. Introduction

Crystalline silicon solar cells have relatively high efficiencies, nevertheless, limited by the high manufacturing cost and long payback period [1, 2]. On the contrary, organic solar cells have arisen more attentions simply due to the high possibility of creating extremely lightweight, easily integration, low-cost, and flexible solar cells [3]. One of the drawbacks on the performance of dye-sensitized solar cells (DSSCs) is the mediocre stability of the liquid electrolyte in the cells.

Room temperature ionic liquids (RTILs) are of increasing interest and importance in clean industrial processes such as liquid solvents for chemical reactions and extractions and in electrochemical applications as electrolytes for DSSCs, fuel cells and lithium batteries [4, 5]. Room temperature ionic liquids can also be utilized in gas sensors and biosensors [6]. To increase photovoltaic properties and stability of a DSSC, a composite ionic liquid electrolyte of mixing silica nanoparticles in the 1-methyl-3-propylimidazolium iodide (MPII) has been used to replace the conventional electrolyte [7–9]. An ionic liquid electrolyte containing dispersed carbon nanoparticles, carbon nanotubes, or titanium

oxide nanoparticles in the 1-methyl-3-methylimidazolium bis(trifluoromethylsulfonyl) imide had a better photocurrent density and voltage [10].

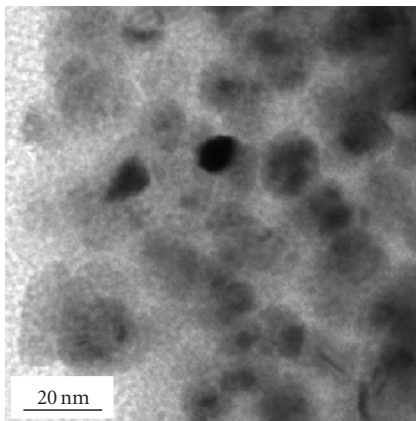
In the separate experiments, size-controllable Cu@C nanoparticles were synthesized by carbonization of Cu²⁺-starch or -cyclodextrins complexes at 673–873 K [11]. In the present work, a very small amount of Cu@C nanoparticles with particle sizes as small as 7–20 nm were dispersed in the RTIL. Their self-diffusion coefficients were determined by pulsed-field gradient spin-echo NMR.

2. Experimental

The RTILs were synthesized by the modified procedures reported by Cammarata et al. [12], Tokuda et al. [13, 14] and Yeon et al. [15]. The nanosize Cu (7, 14, and 20 nm in diameter) encapsulated in the carbon shell (Cu@C) was obtained by carbonization of the Cu²⁺-starch complexes at 673 K for two hours. The ¹H NMR chemical shifts and self-diffusion coefficients were measured using a double-layer tube in which deuterium oxide-d₂ (Aldrich) and the sample were filled in the inner tube (closed system) and outer tube,

TABLE 1: The self-diffusion coefficient and electrical conductivity of the Cu@C dispersed RTIL ([bmim⁺] [PF₆⁻]) measured at 300 K.

| Cu size (nm) | Cu@C (wt%) | Self-diffusion coefficients (10 ⁻¹² m ² s ⁻¹) | | Electrical conductivity (ms/cm) | Viscosity (cp) |
|--------------|------------|--|---------------------------------|------------------------------------|----------------|
| | | [bmim ⁺] | [PF ₆ ⁻] | | |
| | 0 | 5.1 | 5.3 | 2.0 | 178 |
| 7 | 0.08 | 6.4 | 5.5 | 3.1 | 168 |
| 14 | 0.08 | 6.7 | 5.5 | 3.4 | 165 |
| 20 | 0.08 | 6.9 | 5.6 | 3.3 | 164 |

FIGURE 1: The TEM image of the Cu@C (Cu size = 14 nm) dispersed in the RTIL ([bmim⁺] [PF₆⁻]).

respectively [16]. Electrolyte conductivities of the Cu@C dispersed RTIL were measured on the Suntex sc-170 at 300 K. Images of the Cu@C dispersed RTIL were also determined by high resolution transmission electron microscopy (TEM) (Philips CM-200).

The K-edge X-ray absorption near edge structure (XANES) and extended X-ray absorption fine structure (EXAFS) spectra of copper in the Cu@C (0.08%) dispersed RTIL were collected on the Wiggler beam line at the Taiwan National Synchrotron Radiation Research Center. The electron storage was operated at 1.5 GeV (current of 300 mA). The beam energy was calibrated by the adsorption edge of a copper foil at energy of 8979 eV. The EXAFS data were analyzed using the UWXAFS 3.0 and FEFF 8.0 simulation programs [17, 18]. The background of the X-ray absorption spectra was justified by the AUTOBK program [17]. The isolated EXAFS data were normalized to the edge jump and converted to the wavenumber scale. The Fourier transform of the spectra was performed on the k^3 -weighted EXAFS oscillations in the range of 3.5 to 11.5 Å⁻¹. Empirical fits of model compounds have an error of ±0.01 Å in radius and ±10% in coordination number (CN) for the first shell atoms.

3. Results and Discussion

Table 1 shows the self-diffusion coefficients of the [bmim⁺] cations and [PF₆⁻] anions in the Cu@C dispersed RTIL determined by ¹H and ¹⁹F nuclei NMR spectroscopy at

300. The diffusion coefficient of the [bmim⁺] cations in the RTIL dispersed with 0.08% of Cu@C nanoparticles is increased by 25–35% if compared with the plain RTIL. Dispersion and insertion of the Cu@C nanoparticles (Cu sizes = 7–20 nm) in the matrix of the RTIL may cause a reduction of the ionic bonding energy between its cations ([bmim⁺]) and anions ([PF₆⁻]), leading to an increase of the self-diffusion coefficient of the [bmim⁺] cations from 5.1 to 6.9 × 10⁻¹² m²s⁻¹ and a decrease of the RTIL's viscosity from 178 to 164 centipoise (cp). It seems that the Cu@C nanoparticles interact more preferably with the [bmim⁺] cations of the RTIL as the self-diffusion coefficient of the [PF₆⁻] anions influenced by the dispersed Cu@C nanoparticles is relatively insignificant.

In Table 1, in addition to the increase of the self-diffusion coefficients of the [bmim⁺] cations in the RTIL dispersed with the Cu@C nanoparticles, an increase (up to 70%) of the RTIL's electrical conductivity is also found. It is worth noting that the uniform-size Cu@C nanoparticles are well dispersed in the RTIL (see Figure 1). The metallic copper (Cu) having sizes of 7–20 nm is encapsulated in the carbon shell which is consisted of diamond and graphite carbons with a sp³/sp² of 0.5–0.7 (determined by Raman spectroscopy [11]). The greater electrical conductivity of the ionic liquid electrolyte for the new DSSC may be attributed to the electron-rich carbon shell surfaces of the Cu@C nanoparticles that interact with the [bmim⁺] cations in the RTIL.

Molecular-scale data of Cu coated with the carbon shell dispersed in the RTIL in terms of the bond distance and coordination number (CN) of near neighbor atoms can be determined by EXAFS spectroscopy. An over 99% reliability of the EXAFS data fitting for copper species in the RTIL is shown in Table 2. Their Debye-Waller factors are less than 0.01. In the RTIL, Cu (7–20 nm) in the Cu@C nanoparticles has Cu–Cu bond distances of 2.530–2.535 Å, and its CNs increase from 6.2 to 8.7 as the Cu sizes increase.

Figure 2 shows the XANES spectra of copper in the Cu@C nanoparticles dispersed RTIL. Their preedge XANES spectra exhibit a very weak 1s-to-3d transition (8975–8980 eV) which is forbidden by the selection rule in the case of perfect octahedral symmetry. A shoulder at (8984–8988 eV) and an intense band at (8995–9002 eV) is due to the 1s to 4p transition that indicates the existence of the Cu(II) species. The XANES spectrum of copper in the Cu@C is very similar to that in the Cu@C dispersed in the RTIL. Nevertheless, about 11% of Cu originally in the core of the core-shell Cu@C nanoparticles (dispersed in the RTIL) is

TABLE 2: Structure parameters of copper in the Cu@C (0.08%) dispersed RTIL ([bmim⁺] [PF₆⁻]).

| Size (nm) | Shell | Bond distance (Å) | Coordination number | Dybe-Weller factor (σ^2) |
|-----------|-------|-------------------|---------------------|-----------------------------------|
| 7 | Cu–Cu | 2.533 | 6.2 | 0.0079 |
| 14 | Cu–Cu | 2.535 | 6.3 | 0.0081 |
| 20 | Cu–Cu | 2.530 | 8.7 | 0.0075 |

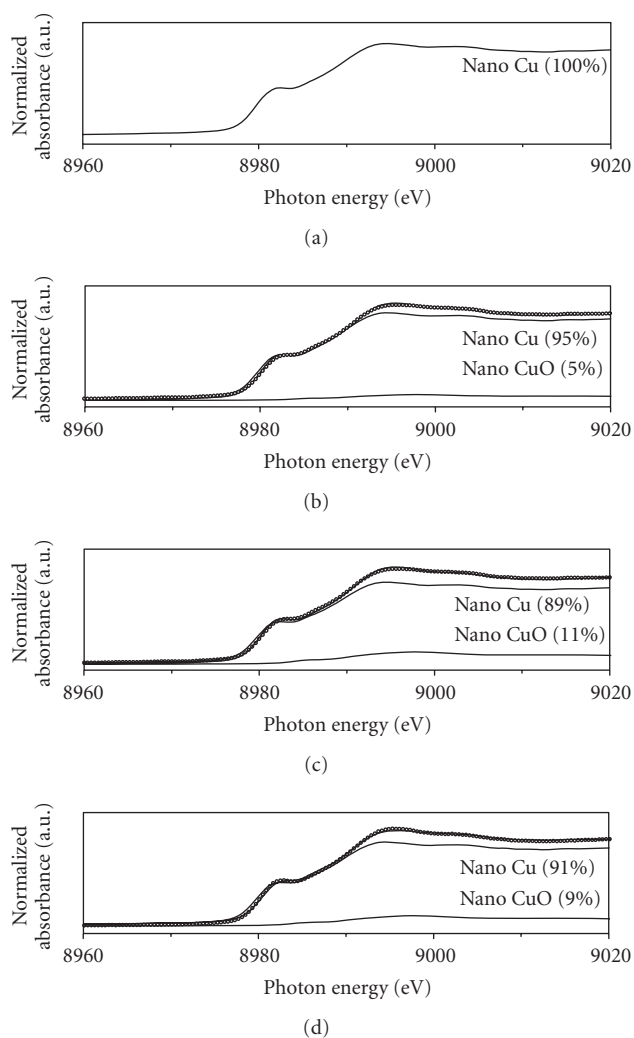


FIGURE 2: The least-square fitted XANES spectra of copper in (a) nanosize Cu and Cu@C (0.08%) having Cu sizes of (b) 7, (c) 14, and (d) 20 nm dispersed in the RTIL ([bmim⁺] [PF₆⁻]).

oxidized to CuO. Note that the fraction of surface Cu atoms to the total atoms for the Cu nanoparticle having a size of 7 nm is 11%. It is very likely that in the RTIL the encapsulated Cu may involve in oxidation with residual oxygen in the RTIL on the surfaces of the Cu nanoparticles. The CuO layer on the surfaces of the core Cu in the Cu@C may also facilitate the electron transport limited to the surfaces of the carbon shell for a better efficiency.

4. Conclusion

Dispersion of a very small amount (0.08%) of Cu@C nanoparticles in the RTIL can increase the diffusion coefficient of the cations in the RTIL by 35%. The diffusion coefficient of the anions in the Cu@C dispersed RTIL is relatively less influenced. An increase (up to 70%) of the Cu@C dispersed RTIL's electrical conductivity is also found. The greater electrical conductivity of the ionic liquid electrolyte for the new DSSC may be attributed to the electron-rich carbon shell surfaces of the Cu@C nanoparticles that interact with the [bmim⁺] cations in the RTIL. The CuO layer on the surfaces of the core Cu in the Cu@C may also facilitate the electron transport limited to the surfaces of the carbon shell for a better efficiency.

Acknowledgments

This research was supported by the Taiwan National Science Council, Bureau of Energy, and the Excellence Project of the National Cheng Kung University. We thank J. F. Lee and Y. M. Yang of the Taiwan Synchrotron Radiation Research Center (SRRC) for their EXAFS experimental assistances. The beam time provided by the SRRC is also appreciated.

References

- [1] G. G. Wallace, P. C. Dastoor, D. L. Officer, and C. O. Too, "Conjugated polymers: new materials for photovoltaics," *Chemical Innovation*, vol. 30, no. 4, pp. 14–22, 2000.
- [2] J. Chen, D. L. Officer, J. M. Pringle, D. R. MacFarlane, C. O. Too, and G. G. Wallace, "Photoelectrochemical solar cells based on polyterthiophenes containing porphyrins using ionic liquid electrolyte," *Electrochemical and Solid-State Letters*, vol. 8, no. 10, pp. A528–A530, 2005.
- [3] B. O'Regan and M. Grätzel, "A low-cost, high-efficiency solar cell based on dye-sensitized colloidal TiO₂ films," *Nature*, vol. 353, no. 6346, pp. 737–740, 1991.
- [4] N. Papageorgiou, Y. Athanassov, M. Armand, et al., "The performance and stability of ambient temperature molten salts for solar cell applications," *Journal of the Electrochemical Society*, vol. 143, no. 10, pp. 3099–3108, 1996.
- [5] H. Matsumoto, T. Matsuda, T. Tsuda, R. Hagiwara, Y. Ito, and Y. Miyazaki, "The application of room temperature molten salt with low viscosity to the electrolyte for dye-sensitized solar cell," *Chemistry Letters*, vol. 30, no. 1, p. 26, 2001.
- [6] S.-F. Ding, M.-Q. Xu, G.-C. Zhao, and X.-W. Wei, "Direct electrochemical response of Myoglobin using a room temperature ionic liquid, 1-(2-hydroxyethyl)-3-methyl imidazolium tetrafluoroborate, as supporting electrolyte," *Electrochemistry Communications*, vol. 9, no. 2, pp. 216–220, 2007.
- [7] F. Zhaofu, K. Daibin, Z. Dongbin, et al., "A supercooled imidazolium iodide ionic liquid as a low-viscosity electrolyte for dye-sensitized solar cells," *Inorganic Chemistry*, vol. 45, no. 26, pp. 10407–10409, 2006.
- [8] W. Ning, L. Honge, L. Jianbao, and L. Xin, "Improved quasi-solid dye-sensitized solar cells by composite ionic liquid electrolyte including layered α -zirconium phosphate," *Applied Physics Letters*, vol. 89, no. 19, Article ID 194104, 3 pages, 2006.
- [9] K. Daibin, W. Peng, I. Seigoe, and M. Grätzel, "Stable mesoscopic dye-sensitized solar cells based on tetracyanoborate

- ionic liquid electrolyte,” *Journal of the American Chemical Society*, vol. 128, no. 24, pp. 7732–7733, 2006.
- [10] H. Usui, H. Matsui, N. Tanabe, and S. Yanagida, “Improved dye-sensitized solar cells using ionic nanocomposite gel electrolytes,” *Journal of Photochemistry and Photobiology A*, vol. 164, no. 1–3, pp. 97–101, 2004.
- [11] C.-H. Huang, H. Paul Wang, and C.-Y. Liao, “Nanosize Copper Encapsulated Carbon Thin Films on a Dye-sensitized Solar Cell Cathode,” *Journal of Nanoscience and Nanotechnology*, 2009, (in press).
- [12] L. Cammarata, S. G. Kazarian, P. A. Salter, and T. Welton, “Molecular states of water in room temperature ionic liquids,” *Physical Chemistry Chemical Physics*, vol. 3, no. 23, pp. 5192–5200, 2001.
- [13] H. Tokuda, K. Hayamizu, K. Ishii, Md. A. B. Hasan-Susan, and M. Watanabe, “Physicochemical properties and structures of room temperature ionic liquids. 1. Variation of anionic species,” *Journal of Physical Chemistry B*, vol. 108, no. 42, pp. 16593–16600, 2004.
- [14] H. Tokuda, K. Hayamizu, K. Ishii, Md. A. B. Hasan-Susan, and M. Watanabe, “Physicochemical properties and structures of room temperature ionic liquids. 2. Variation of alkyl chain length in imidazolium cation,” *Journal of Physical Chemistry B*, vol. 109, no. 13, pp. 6103–6110, 2005.
- [15] S.-H. Yeon, K.-S. Kim, S. Choi, H. Lee, H. S. Kim, and H. Kim, “Physical and electrochemical properties of 1-(2-hydroxyethyl)-3-methyl imidazolium and *N*-(2-hydroxyethyl)-*N*-methyl morpholinium ionic liquids,” *Electrochimica Acta*, vol. 50, no. 27, pp. 5399–5407, 2005.
- [16] H. Tokuda, S. Tsuzuki, Md. A. B. Hasan-Susan, K. Hayamizu, and M. Watanabe, “How ionic are room-temperature ionic liquids? An indicator of the physicochemical properties,” *Journal of Physical Chemistry B*, vol. 110, no. 39, pp. 19593–19600, 2006.
- [17] A. L. Ankudinov, B. Ravel, J. J. Rehr, and S. D. Conradson, “Real-space multiple-scattering calculation and interpretation of X-ray-absorption near-edge structure,” *Physical Review B*, vol. 58, no. 12, pp. 7565–7576, 1998.
- [18] E. A. Stern, M. Newville, B. Ravel, Y. Yacoby, and D. Haskel, “The UWXAFS analysis package: philosophy and details,” *Physica B*, vol. 208-209, pp. 117–120, 1995.

Research Article

Applications of Cu@C Nanoparticles in New Dye-Sensitized Solar Cells

Chang-Yu Liao,¹ H. Paul Wang,^{1,2} F.-L. Chen,³ C.-H. Huang,¹ and Y. Fukushima¹

¹Department of Environmental Engineering, National Cheng Kung University, Tainan City 70101, Taiwan

²Sustainable Environment Research Center, National Cheng Kung University, Tainan City 70101, Taiwan

³Department of Chemistry, National Cheng Kung University, Tainan City 70101, Taiwan

Correspondence should be addressed to H. Paul Wang, wanghp@mail.ncku.edu.tw

Received 6 October 2008; Accepted 22 January 2009

Recommended by Alan K. T. Lau

To enhance the efficiency of a newly developing dye-sensitized solar cell (DSSC), the Cu@C (Cu size = 7 and 20 nm) core-shell nanoparticles-dispersed molten salt-conjugated electrolyte has been studied. Experimentally, the efficiencies (η) of the DSSC are in the range of 2.70–4.09% with a short-circuit photocurrent density (J_{SC}) of 5.775–9.910 mA/cm². Interestingly, it is found that dispersion of 1% of the Cu@C (Cu size = 7 nm) nanoparticles in the molten salt-(1,2-dimethyl-3-propylimidazolium iodide (DMPII)) conjugated electrolyte results in an enhancement (about 11%) of the η (4.06%). Greater fractions (3–10%) of the Cu@C nanoparticles dispersed in the molten salt cause a poor performance (lower J_{SC} and η) of the DSSC possibly due to interference of the internal electron transportation routes in the DSSC by oxidation of Cu with I₂ originally in the electrolyte.

Copyright © 2009 Chang-Yu Liao et al. This is an open access article distributed under the Creative Commons Attribution License, which permits unrestricted use, distribution, and reproduction in any medium, provided the original work is properly cited.

1. Introduction

Dye-sensitized solar cells with advantages of low manufacturing cost and comparable light-to-electricity conversion efficiency to conventional silicon-based photovoltaic cells have been considered as the next-generation clean energy sources [1]. However, incorporation of liquid solvents such as acetonitrile and iodide/triiodide redox mediators in the cell has been facing problems, for instance, solvent evaporation (reducing life-time), inconvenience in the module sealing, and carcinogenic concerning of chemicals used in the electrolyte. Alternatively, a quasisolid-like composite electrolyte turns out to be a solution of those problems [2–8]. Hiroki et al. found that incorporation of carbon materials in a molten salt could improve the electric conductivity of the quasisolid-like electrolyte, which also had better photon conversion efficiency [3]. In the present work, Cu@C (copper encapsulated in the carbon shell) nanoparticles were dispersed in a molten salt (1,2-dimethyl-3-propylimidazolium iodide (DMPII)) as a nanocomposite electrolyte utilized in DSSCs. X-ray absorption near edge structure (XANES) spectroscopy was also used to reveal speciation of copper in the Cu@C nanoparticles dispersed in the molten salt.

2. Experimental

The core-shell (Cu@C) nanoparticles were synthesized via carbonization of Cu²⁺-starch complexes at 673 K for 12 hours. By TEM and XRD, it is clear that the Cu@C nanoparticles have the (core) metallic copper (Cu) sizes of 7–20 nm. The Cu@C nanoparticles (0.3–10 wt%) were dispersed in the DMPII (Solaronix SA, Switzerland) (0.6 M) in an electrolyte which contains 0.1 M of LiI (Aldrich, USA), 0.05 M of I₂ (Riedel-de Haën, Germany), and 0.5 M of 4-*tert*-butylpyridine (Aldrich, USA) in acetonitrile (Mallinckrodt, USA).

To fabricate the photoelectrode of the DSSC, 6 g of nanosize TiO₂ (P25 nanograde, Degussa, Germany) were mixed with a solution containing 0.1 mL of Triton X-100 (Sigma-Aldrich, USA), 0.2 mL of acetylacetone (Fluka, Switzerland), and 10 mL of deionized water to yield a TiO₂ paste. Three drops of the TiO₂ paste were spread on the Scotch magic tape-(3M) masked fluorine-doped tin oxide substrate (8 ohm/square, Solaronix SA, Switzerland) (2.5 cm × 2.5 cm) by the doctor-blade method. The as-coated glass was dried and scratched out for a working area of 0.25 cm², preheated at 323 K for 15 minutes, and calcined at 723 K for

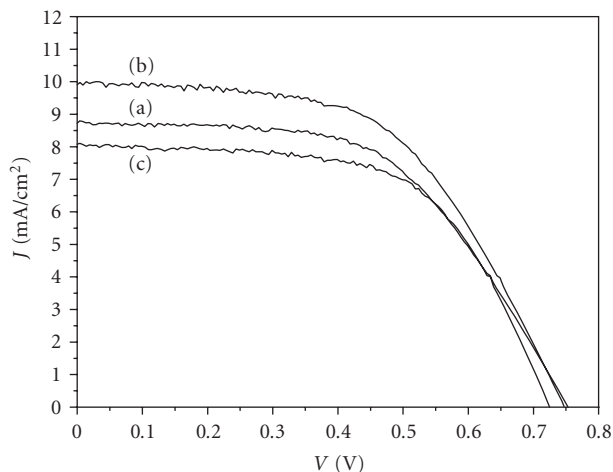


FIGURE 1: Photocurrent density (J) of the DSSC containing (a) 0, (b) 1, and (c) 3% of the Cu@C nanoparticles (Cu size = 7 nm) dispersed in the molten salt.

30 minutes. The TiO₂-coated glass was immersed in a 3×10^{-4} M of N3 (*cis*-di(thiocyanato)-*N,N'*-bis(2,2'-bipyridyl-4,4'-dicarboxylate) ruthenium(II), ruthenium 535, Solaronix SA, Switzerland) anhydrous ethanol solution for 24 hours in the dark. The stained photoelectrode was dried in N₂ for the assemblage of the DSSC.

The counterelectrode was prepared by distribution of three drops of H₂PtCl₆·6H₂O (Alfa Aesar, USA) on the conducting tin oxide electrode (10 ohm/square, RITEK, Taiwan) with a spin-coater (SP-M1-S, APISC, Taiwan) at 1500 rpm for 15 seconds. The electrode was preheated at 323 K for 10 minutes and calcined at 658 K for 10 minutes.

The photoelectrode and counterelectrode were sandwiched together with a 60 μm thick hot-melt thermal foil (SO-SX1170, Solaronix SA, Switzerland) as a spacer. The Cu@C dispersed electrolyte was introduced into the cell and sealed with AB epoxy that was cured for 30 minutes. A 300 W xenon arc lamp solar simulator (no. 91160A, Oriel, USA) conjugated with an AM 1.5 Globe filter (no. 59044, Oriel, USA) was employed to measure the I - V characteristics of the quasisolid-state DSSC. The illumination was fixed at 100 mW/cm² using a reference solar cell and meter (no. 91150, Oriel, USA). In each experiment, at least five solar cell measurements were carried out to ensure the acceptable data being obtained.

The copper K-edge XANES spectra of the Cu@C nanoparticles dispersed (1–10%) in the electrolyte were determined on the Wiggler BL17C1 beam line at the Taiwan National Synchrotron Radiation Research Center. The electron storage ring was operated at energy of 1.5 GeV. A Si(111) double-crystal monochromator was used for selection of energy with an energy resolution ($\Delta E/E$) about 1.9×10^{-4} (eV/eV). The incident photon energy was calibrated using a standard copper foil with a characteristic absorption edge at 8979 eV. The XANES spectra of copper in the Cu@C nanoparticles were analyzed with the UWXAFS 3.0 program [9]. Semiquantitative analyses of the XANES spectra of copper were conducted by the least-square fitting of linear

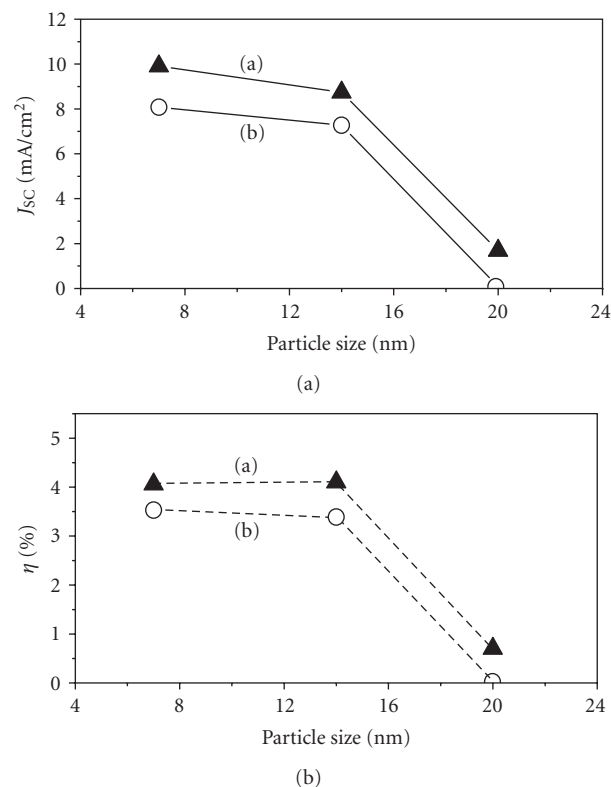


FIGURE 2: Dependence of Cu sizes in the Cu@C nanoparticles ((a) 1 and (b) 3%) dispersed molten salt in the electrolyte on the short-circuit photocurrent density (J_{SC}) and conversion efficiency (η) of the DSSC.

combinations of standard spectra (Cu (Merck, Germany, 99.7%), Cu₂O (Aldrich, USA, 97%), CuO (Merck, Germany, 99%), and NanoTeK^R CuO (Kanto, Japan, 99.3%)) to the spectra of samples. On the average, an uncertainty limit of 5% corresponds to an error of about c.a. 2.0% in the fitting results.

3. Results and Discussion

The I - V characteristics of the quasisolid-state DSSC enhanced with the Cu@C nanoparticles (Cu size = 7 nm) dispersed molten salt (DMPII) in the electrolyte are shown in Figure 1. The DSSC containing 1% of the Cu@C nanoparticles dispersed in the molten salt exhibits a maximum short-circuit photocurrent density ($J_{SC} = 9.910$ mA/cm²), moderate open-circuit photovoltage ($V_{OC} = 0.748$ V) and an enhancement (about 11%) of the conversion efficiency ($\eta = 4.06\%$). A greater fraction (3%) of the Cu@C nanoparticles, on the contrary, leads to a decrease of the conversion efficiency ($\eta = 3.53\%$).

Figure 2 shows the dependence of the Cu sizes in the core of the Cu@C nanoparticles on J_{SC} and η of the DSSC. It seems that J_{SC} and η decrease with an increase of the Cu size in the Cu@C nanoparticles. For the large Cu@C nanoparticles (Cu size = 20 nm) dispersed molten salt in the DSSC, the J_{SC} (Figure 2(a)) and η (Figure 2(b)) are dramatically reduced.

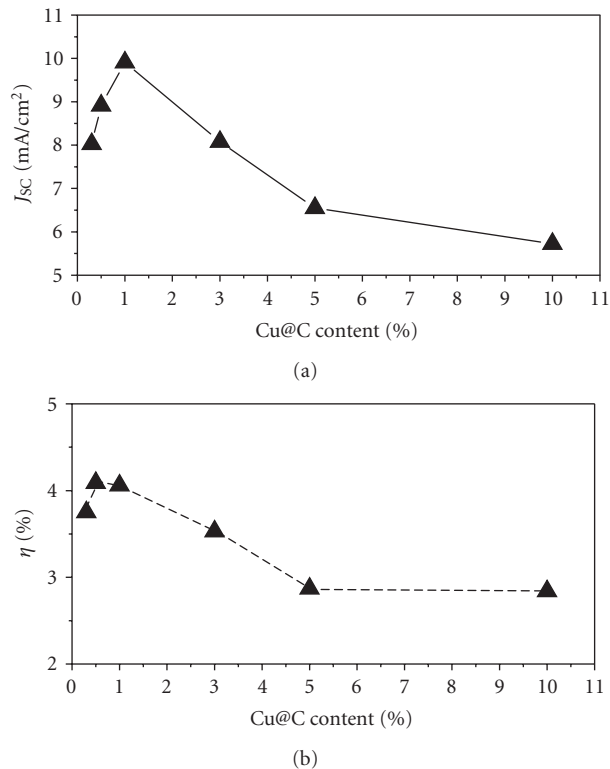


FIGURE 3: Dependence of fractions of Cu@C nanoparticles (Cu size = 7 nm) dispersed in the molten salt on the (a) short-circuit photocurrent density (J_{sc}) and (b) conversion efficiency (η) of the DSSC.

In Figure 3, the DSSC containing 1% of the Cu@C (Cu size = 7 nm) nanoparticles dispersed in the molten salt in the electrolyte has a desirable J_{sc} (9.910 mA/cm²) and η (4.06%). In the separate experiments, we also found that the self-diffusion coefficients of cations and anions in a room temperature ionic liquid ([bmim][BF₄]) dispersed with 0.08% of Cu@C nanoparticles were increased by 4.3–6.6 times [10]. The electrical conductivity of the Cu@C dispersed [bmim][BF₄] was increased by as high as 3.7 times in comparison with that without the Cu@C nanoparticles [10]. Nevertheless, in the present work, it is found that greater fractions (3–10%) of the Cu@C nanoparticles dispersed in the molten salt, on the contrary, may interfere the internal electron transportation routes or result in the electron back transportation from photoelectrode to counterelectrode, which cause a poor performance (lower J_{sc} and η) of the DSSC. A short-circuit in the presence of a large amount of carbon nanotubes and/or carbon nanoparticles in the quasi-solid-state DSSCs was also found by Usui et al. [3].

Molecular-scale data of select compounds in the complex matrix determined by XANES turn out to be very useful in revealing chemical structure and composition of key species in the reaction pathways [11, 12]. Figure 4 illustrates the XANES spectra of copper in the Cu@C nanoparticles-dispersed molten salt. The Cu@C nanoparticles contain mainly nanosize Cu (63%), Cu₂O (13%), and CuO (24%). Note that after the repeatedly efficiency measurements of

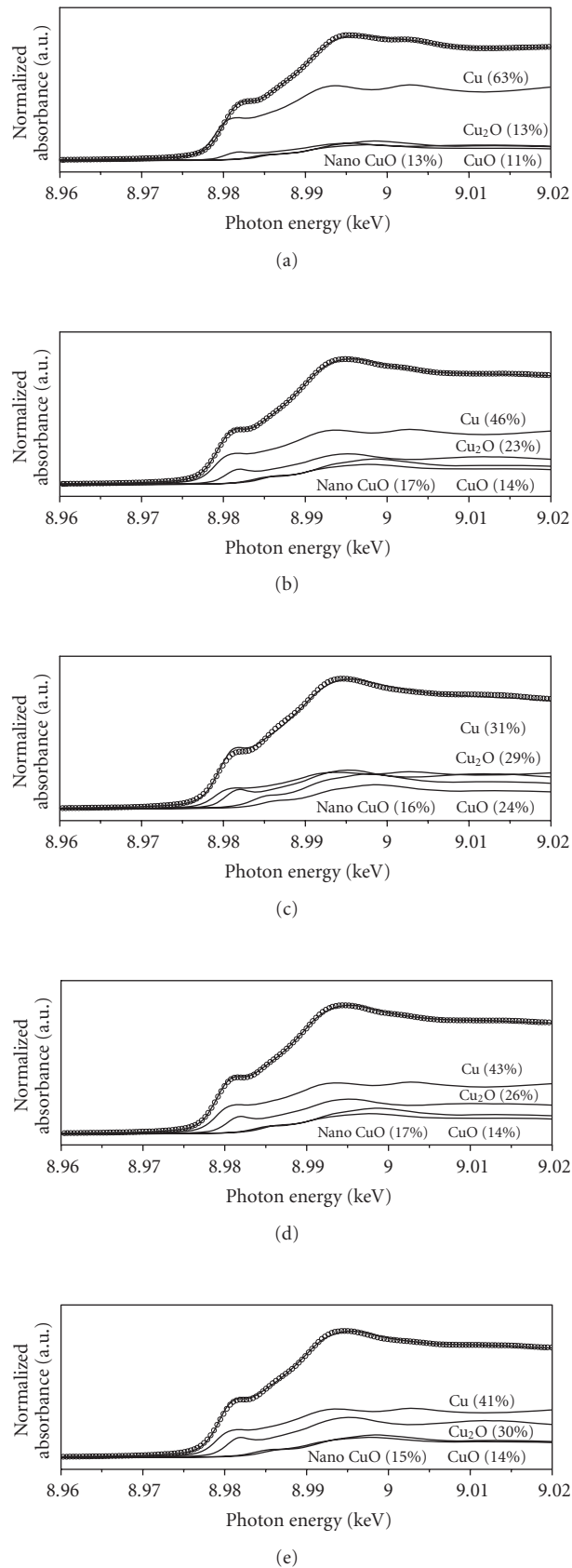


FIGURE 4: The least-square fitted XANES spectra of copper in the Cu@C nanoparticles (Cu size = 7 nm) (fractions of (a) 0, (b) 1, (c) 3, (d) 5, and (e) 10%) dispersed in the molten salt.

the quasisolid-state DSSC, in the presence of 0.05 M of I_2 (in the electrolyte), 17–32% of Cu encapsulated in the carbon shells are oxidized to Cu_2O (10–17%) and CuO (5–17%) (Figure 4). The oxidation of Cu with I_2 may interfere the internal electron transportation routes in the DSSC. As shown in Figure 3, greater fractions (3–10%) of the Cu@C nanoparticles dispersed in the molten salt in the electrolyte result in a poor performance (lower J_{SC} and η) of the DSSC.

Generally, the ratio of surface-to-total atoms for a Cu nanoparticle having a size of 7 nm is about 0.11. It seems that oxidation occurs mainly on the surfaces of the Cu nanoparticles, and further oxidation down to subsurfaces may be limited to about 40% of the total Cu atoms. The CuO or Cu_2O layer on the surfaces of the core Cu in the Cu@C may not perturb directly the electron transportation routes in the DSSC. Alternatively, the electron-rich surfaces of the carbon shell consisted of diamond and graphite carbons may play the main role in the electrical conduction.

4. Conclusions

Enhancements of the short-circuit photocurrent density (J_{SC}) and solar conversion efficiency (η) of the DSSC with the Cu@C nanoparticles-dispersed molten salt-conjugated electrolyte have been observed. The DSSC containing 1% of the Cu@C (Cu size = 7 nm) nanoparticles dispersed in the molten salt has a desirable J_{SC} (9.910 mA/cm²) and η (4.06%). Greater fractions (3–10%) of the Cu@C nanoparticles dispersed in the molten salt cause a poor performance (lower J_{SC} and η) of the DSSC possibly due to interference of the normal internal electron transportation routes in the DSSC by oxidation of Cu with I_2 originally in the electrolyte.

Acknowledgments

The financial supports of the Taiwan National Science Council, Bureau of Energy, the Excellence Project of the National Cheng Kung University, and National Synchrotron Radiation Research Center are gratefully acknowledged.

References

- [1] B. O'Regan and M. Grätzel, "A low-cost, high-efficiency solar cell based on dye-sensitized colloidal TiO_2 films," *Nature*, vol. 353, no. 6346, pp. 737–740, 1991.
- [2] P. Wang, S. M. Zakeeruddin, P. Comte, I. Exnar, and M. Grätzel, "Gelation of ionic liquid-based electrolytes with silica nanoparticles for quasi-solid-state dye-sensitized solar cells," *Journal of the American Chemical Society*, vol. 125, no. 5, pp. 1166–1167, 2003.
- [3] H. Usui, H. Matsui, N. Tanabe, and S. Yanagida, "Improved dye-sensitized solar cells using ionic nanocomposite gel electrolytes," *Journal of Photochemistry and Photobiology A*, vol. 164, no. 1–3, pp. 97–101, 2004.
- [4] T. Kato, T. Kado, S. Tanaka, A. Okazaki, and S. Hayase, "Quasi-solid dye-sensitized solar cells containing nanoparticles modified with ionic liquid-type molecules," *Journal of the Electrochemical Society*, vol. 153, no. 3, pp. A626–A630, 2006.

- [5] B. Xue, H. Wang, Y. Hu, et al., "Highly efficient dye-sensitized solar cells using a composite electrolyte," *Comptes Rendus Chimie*, vol. 9, no. 5-6, pp. 627–630, 2006.
- [6] T. Katakabe, R. Kawano, and M. Watanabe, "Acceleration of redox diffusion and charge-transfer rates in an ionic liquid with nanoparticle addition," *Electrochemical and Solid-State Letters*, vol. 10, no. 6, pp. F23–F25, 2007.
- [7] Z. Lan, J. Wu, D. Wang, S. Hao, J. Lin, and Y. Huang, "Quasi-solid-state dye-sensitized solar cells based on a sol-gel organic-inorganic composite electrolyte containing an organic iodide salt," *Solar Energy*, vol. 81, no. 1, pp. 117–122, 2007.
- [8] M. Berginc, M. Hočvar, U. O. Krašovec, A. Hinsch, R. Sastrawan, and M. Topič, "Ionic liquid-based electrolyte solidified with SiO_2 nanoparticles for dye-sensitized solar cells," *Thin Solid Films*, vol. 516, no. 14, pp. 4645–4650, 2008.
- [9] E. A. Stern, M. Newville, B. Ravel, Y. Yacoby, and D. Haskel, "The UWXAFS analysis package: philosophy and details," *Physica B*, vol. 208-209, pp. 117–120, 1995.
- [10] F. L. Chen, I. W. Sun, H. P. Wang, and C. H. Huang, "Nanosize copper dispersed ionic liquids as an electrolyte of new dye-sensitized solar cells," *Journal of Nanomaterials*, in press.
- [11] H.-L. Huang, H. P. Wang, G.-T. Wei, I.-W. Sun, J.-F. Huang, and Y. W. Yang, "Extraction of nanosize copper pollutants with an ionic liquid," *Environmental Science & Technology*, vol. 40, no. 15, pp. 4761–4764, 2006.
- [12] H. H. Hsu, J. H. Huang, H. P. Wang, and C. J. G. Jou, "Speciation of zinc in nano phosphor particulars abstracted in an ionic liquid," *Radiation Physics and Chemistry*, vol. 75, no. 11, pp. 1930–1933, 2006.

Research Article

Sensing of Ethanol with Nanosize Fe-ZnO Thin Films

G.-H. Kuo,¹ H. Paul Wang,^{1,2} H. H. Hsu,¹ James Wang,³ Y. M. Chiu,¹ C.-J. G. Jou,⁴
T. F. Hsu,¹ and F.-L. Chen⁵

¹ Department of Environmental Engineering, National Cheng Kung University, Tainan City 70101, Taiwan

² Sustainable Environment Research Center, National Cheng Kung University, Tainan City 70101, Taiwan

³ Department of Bioengineering, University of Washington, Seattle, WA 98105, USA

⁴ Department of Safety, Health and Environmental Engineering, National Kaohsiung First University of Science and Technology, Kaohsiung City 81184, Taiwan

⁵ Department of Chemistry, National Cheng Kung University, Tainan City 70101, Taiwan

Correspondence should be addressed to H. Paul Wang, wanghp@mail.ncku.edu.tw

Received 7 October 2008; Accepted 24 February 2009

Recommended by Alan K. T. Lau

Sensing of ethanol with iron doped ZnO (Fe-ZnO) thin films has been studied in this work. By X-ray diffraction spectroscopy, it is found that ZnO is the main compound in the low-iron (<10%) doped ZnO thin films. ZnFe₂O₄ is also found as 20–50% of iron are doped on the thin films. The 5% Fe-ZnO thin film has a very high sensitivity ($R_{\text{air}}/R_{\text{ethanol}} > 70$) to 1000 ppm of ethanol at 300 K. It seems that iron can promote the sensitivity of the ZnO thin film. The thin film doped with a greater amount (20–50%) of iron has, however, a much less sensitivity (<15) to ethanol. The chemical interactions between oxygen of ethanol and zinc on the Fe-ZnO thin film cause changes of the bond distances of Zn–O and Fe–O in the thin films to 1.90 and 1.98 Å which can be restored to 1.91 and 1.97 Å, respectively, in the absence of ethanol.

Copyright © 2009 G.-H. Kuo et al. This is an open access article distributed under the Creative Commons Attribution License, which permits unrestricted use, distribution, and reproduction in any medium, provided the original work is properly cited.

1. Introduction

Real-time detection of toxic gases by analytical equipments such as FTIR, GC, or mass spectrometers is expensive and not practical mainly due to their bulky sizes. Metal oxide semiconductor sensors have advantages of small size, low mass, good sensitivity and low cost [1–3]. ZnO which is an n-type semiconductor (band-gap = 3.2 eV) has been widely used in sensing of gases such as H₂, H₂O, and CH₄ [1–8]. Methods of preparing ZnO thin films include spray pyrolysis, chemical vapor deposition, sputtering, electron beam evaporation, screen printing, and sol-gel methods [9–16]. However, ZnO thin films have drawbacks, for instance, the working temperature is too high (>673 K) and their sensitivities are frequently not very desired [17]. To improve sensitivity, transition metals can be doped onto ZnO thin films [18]. Generally sensors doped with transition metals may also lead to a better stability [19]. Thus the main objective of the present work was to investigate sensitivities of the ZnO thin films doped with iron (5–50%) in the presence of ethanol vapor. Nature of the sensing active species in the iron-doped ZnO (Fe-ZnO) thin films was also studied by

in situ extended X-ray absorption fine structure (EXAFS) spectroscopy.

2. Experimental

The Fe-ZnO thin films were prepared by dissolving Zn(CH₃COO)₂ · 2H₂O (OSAKA) and Fe(NO₃)₃ · 9H₂O (MERCK, 99%) in 2-methoxyethanol (MERCK), to which a surfactant, monoethanolamine (MEA) (WAKO); was subsequently added. The molar ratio of MEA to Zn(CH₃COO)₂ was 0.02. The mole fractions of Fe(NO₃)₃ in the ZnO thin films were 0, 5, 10, 20, and 50%. The thin films were prepared by dip-coating on a home-made slow pulling device at a speed of 1.2 cm/d. The thin film samples were preheated at 523 K for 10 minutes to decompose organic compounds and annealed at 773 K for 60 minutes.

Chemical structure of the Fe-ZnO thin films was determined by X-ray powder diffraction (XRD) spectroscopy (D8 advance, Bruker) with a Cu K α radiation ($\lambda = 1.542 \text{ \AA}$). The surface morphology of the thin films was also measured by scanning electron microscope (SEM) (S-3000N, Phillips). In situ EXAFS spectra of zinc and iron in the Fe-ZnO thin

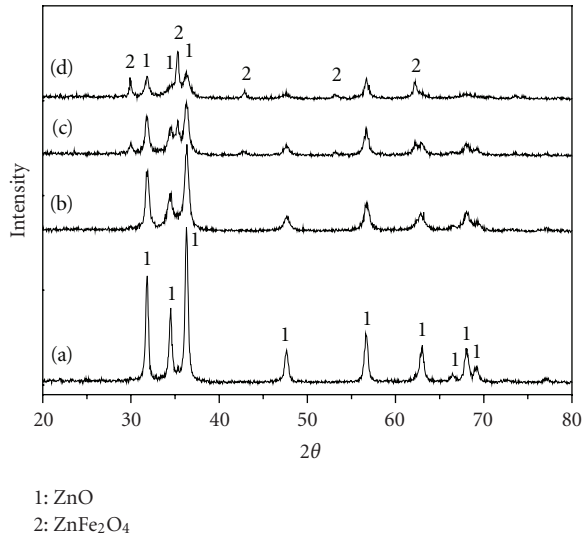


FIGURE 1: X-ray diffraction patterns of the Fe-ZnO thin films doped with (a) 5, (b) 10, (c) 20, and (d) 50% of iron.

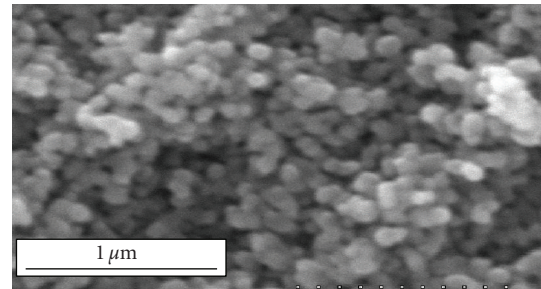
films were recorded on the Wiggler beam line (BL17C) at the National Synchrotron Radiation Research Center (NSRRC), Taiwan.

3. Results and Discussion

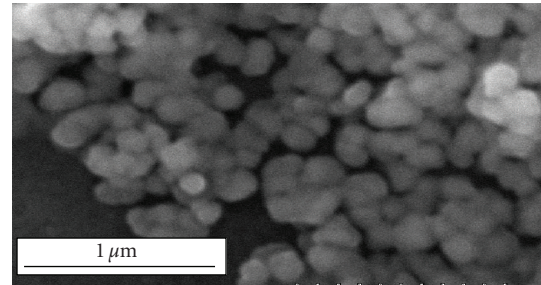
The X-ray diffraction (XRD) patterns of the Fe-ZnO thin films are illustrated in Figure 1. For the low-iron (0–10%) doped ZnO thin films, the main compound in the thin films is ZnO. As the fractions of the doped iron are greater than 20%, in addition to ZnO, ZnFe₂O₄ is also observed. By SEM, it is found that the thin film is consisted of nanosize ZnO which is packed closely and well distributed (Figure 2). The mean particle size of ZnO in the thin film is in the range of 50–90 nm.

Figure 3 shows the sensitivities ($R_{\text{air}}/R_{\text{ethanol}}$) of the ZnO and Fe-ZnO-Fe thin films in the presence of 1000 ppm of ethanol at 300 K. The sensitivity and response time of the ZnO thin film to ethanol are about 50 and 2.5 minutes, respectively. Interestingly, it is found that the 5% Fe-ZnO thin film has a relatively higher sensitivity (>70) and shorter response time (one minutes). Increasing the amount (>10%) of iron doped on the ZnO thin films leads to a rapid decrease of the sensitivity to less than 15.

It seems that a small amount (e.g., 5%) of iron can promote the sensitivity of the ZnO thin film to ethanol. The thin film doped with greater amount (20–50%) of iron has, on the contrary, a much less sensitivity to ethanol ($R_{\text{air}}/R_{\text{ethanol}} < 15$). To obtain a better understanding of interactions involved during sensing, the thin films have also been studied by in situ EXAFS spectroscopy. During sensing of ethanol, the chemical interactions between oxygen of ethanol and zinc on the Fe-ZnO thin film can be observed by EXAFS. An over 99% reliability of the EXAFS data fitting for zinc and iron species in the Fe-ZnO thin films is shown in Table 1. Their Debye-Waller factors ($\Delta\sigma^2$) were less than



(a)



(b)

FIGURE 2: SEM morphologies of the Fe-ZnO thin films doped with (a) 5 and (b) 10% of iron.

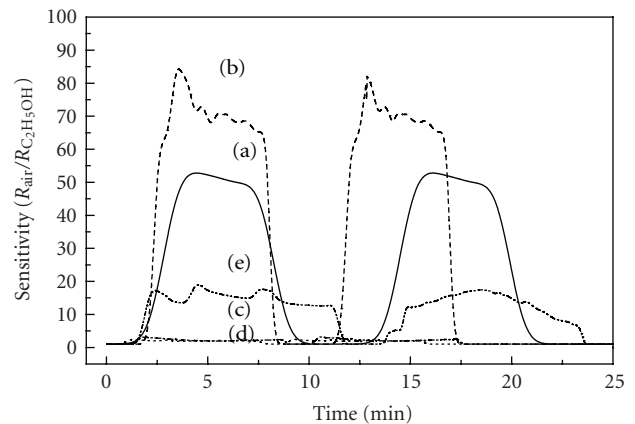


FIGURE 3: Dependence of time on sensitivities of the Fe-ZnO thin films doped with (a) 5, (b) 10, (c) 20, and (d) 50% of iron to 1000 ppm of ethanol at 300 K.

0.01 ($\Delta\sigma < 0.1 \text{ \AA}$ in general). Adsorption of ethanol on the 5% Fe-ZnO has caused changes of bond distances of Zn-O and Fe-O in the thin films to 1.90 and 1.98 \AA and restored to 1.91 and 1.97 \AA , respectively, in the absence of ethanol. The thin films doped with excess (>20%) iron have less amount of sensing active ZnO species which are consumed in formation of ZnFe₂O₄.

4. Conclusions

at the ambient temperature (e.g., 300 K), it is found experimentally that iron can promote the sensitivity of the ZnO thin

TABLE 1: In situ EXAFS data of zinc and iron in the 5% Fe-ZnO thin film during sensing of ethanol at 300 K.

| Ethanol (ppm) | Shells | Bond distance (Å) | σ^2 (Å ²) |
|---------------|--------|-------------------|------------------------------|
| 0 | Zn–O | 1.91 | 0.008 |
| 0 | Fe–O | 1.97 | 0.008 |
| 1000 | Zn–O | 1.90 | 0.008 |
| 1000 | Fe–O | 1.98 | 0.008 |

σ^2 : Debye-Waller factor.

film, for instance, the thin film doped with 5% of iron has a relatively higher sensitivity (>70) and shorter response time (one minutes) when sensing of 1000 ppm of ethanol vapor. On the contrary, the thin films doped with 20–50% of iron have a very low sensitivity to ethanol ($R_{\text{air}}/R_{\text{ethanol}} < 15$). By in situ EXAFS, it is found that sensing of ethanol on the Fe-ZnO has caused changes of bond distances of Zn–O and Fe–O in the thin films to 1.90 and 1.98 Å and restored to 1.91 and 1.97 Å, respectively in the absence of ethanol. It is clear that the thin films doped with excess ($>20\%$) iron have less amount of sensing active ZnO species which are consumed in formation of ZnFe_2O_4 .

Acknowledgments

The financial support of the National Science Council, Bureau of Energy, and NSRRC, Taiwan is gratefully acknowledged. The authors also thank Y. W. Yang and Jyh-Fu Lee of the NSRRC for their XAS experimental assistances.

References

- [1] T. Seiyama, A. Kato, K. Fujiishi, and M. Nagatani, "A new detector for gaseous components using semiconductive thin films," *Analytical Chemistry*, vol. 34, no. 11, pp. 1502–1503, 1962.
- [2] D. F. Paraguay, M. Miki-Yoshida, J. Morales, J. Solis, and L. W. Estrada, "Influence of Al, In, Cu, Fe and Sn dopants on the response of thin film ZnO gas sensor to ethanol vapour," *Thin Solid Films*, vol. 373, no. 1-2, pp. 137–140, 2000.
- [3] I. Stambolova, K. Konstantinov, S. Vassilev, P. Peshev, and T. Tsacheva, "Lanthanum doped SnO_2 and ZnO thin films sensitive to ethanol and humidity," *Materials Chemistry and Physics*, vol. 63, no. 2, pp. 104–108, 2000.
- [4] S. M. Chou, L. G. Teoh, W. H. Lai, Y. H. Su, and M. H. Hon, "ZnO:Al thin film gas sensor for detection of ethanol vapor," *Sensors*, vol. 6, no. 10, pp. 1420–1427, 2006.
- [5] L.-J. Meng and M. P. dos Santos, "Properties of indium tin oxide (ITO) films prepared by r.f. reactive magnetron sputtering at different pressures," *Thin Solid Films*, vol. 303, no. 1-2, pp. 151–155, 1997.
- [6] X. L. Cheng, H. Zhao, L. H. Huo, S. Gao, and J. G. Zhao, "ZnO nanoparticulate thin film: preparation, characterization and gas-sensing property," *Sensors and Actuators B*, vol. 102, no. 2, pp. 248–252, 2004.
- [7] M. Ohyama, H. Kozuka, and T. Yoko, "Sol-gel preparation of transparent and conductive aluminum-doped zinc oxide films with highly preferential crystal orientation," *Journal of the American Ceramic Society*, vol. 81, no. 6, pp. 1622–1632, 1998.
- [8] P. P. Sahay and R. K. Nath, "Al-doped ZnO thin films as methanol sensors," *Sensors and Actuators B*, vol. 134, no. 2, pp. 654–659, 2008.
- [9] E. Traversa and A. Bearzotti, "A novel humidity-detection mechanism for ZnO dense pellets," *Sensors and Actuators B*, vol. 23, no. 2-3, pp. 181–186, 1995.
- [10] P. Nunes, E. Fortunato, A. Lopes, and R. Martins, "Influence of the deposition conditions on the gas sensitivity of zinc oxide thin films deposited by spray pyrolysis," *International Journal of Inorganic Materials*, vol. 3, no. 8, pp. 1129–1131, 2001.
- [11] S. K. Hazra and S. Basu, "Hydrogen sensitivity of ZnO p - n homojunctions," *Sensors and Actuators B*, vol. 117, no. 1, pp. 177–182, 2006.
- [12] Y. Liu and M. Liu, "Ordered ZnO nanorods synthesized by combustion chemical vapor deposition," *Journal of Nanoscience and Nanotechnology*, vol. 7, no. 12, pp. 4529–4533, 2007.
- [13] L. P. Schuler, M. M. Alkaiji, P. Miller, and R. J. Reeves, "UV sensing using surface acoustic wave device on DC sputtered ZnO monolayer," *Microelectronic Engineering*, vol. 83, no. 4–9, pp. 1403–1406, 2006.
- [14] M. S. Wagh, L. A. Patil, T. Seth, and D. P. Amalnerkar, "Surface cupricated SnO_2 -ZnO thick films as a H_2S gas sensor," *Materials Chemistry and Physics*, vol. 84, no. 2-3, pp. 228–233, 2004.
- [15] S. Dixit, A. Srivastava, A. Srivastava, and R. K. Shukla, "Sol-gel derived zinc oxide films and their sensitivity to humidity," *Japanese Journal of Applied Physics*, vol. 47, no. 7, pp. 5613–5618, 2008.
- [16] K. R. Murali, "Properties of sol-gel dip-coated zinc oxide thin films," *Journal of Physics and Chemistry of Solids*, vol. 68, no. 12, pp. 2293–2296, 2007.
- [17] E. Comini, "Metal oxide nano-crystals for gas sensing," *Analytica Chimica Acta*, vol. 568, no. 1-2, pp. 28–40, 2006.
- [18] N. Yamazoe, "New approaches for improving semiconductor gas sensors," *Sensors and Actuators B*, vol. 5, no. 1–4, pp. 7–19, 1991.
- [19] R. Wang, L. L. H. King, and A. W. Sleight, "Highly conducting transparent thin films based on zinc oxide," *Journal of Materials Research*, vol. 11, no. 7, pp. 1659–1664, 1996.

Research Article

Surface Enamel Remineralization: Biomimetic Apatite Nanocrystals and Fluoride Ions Different Effects

Norberto Roveri,¹ Elisa Battistella,² Claudia Letizia Bianchi,³ Ismaela Foltran,^{1,2}
Elisabetta Foresti,¹ Michele Iafisco,^{1,2} Marco Lelli,¹ Alberto Naldoni,³
Barbara Palazzo,^{1,2} and Lia Rimondini²

¹ Department of Chemistry "G. Ciamician", University of Bologna, Via Selmi 2, 40126 Bologna, Italy

² Department of Medical Sciences, University of Eastern Piedmont "Amedeo Avogadro", Via Solaroli 17, 28100 Novara, Italy

³ Department of Physical Chemistry and Electrochemistry, University of Milano, Via Golgi 19, 20133 Milano, Italy

Correspondence should be addressed to Norberto Roveri, norberto.roveri@unibo.it

Received 13 October 2008; Accepted 22 January 2009

Recommended by Alan K. T. Lau

A new method for altered enamel surface remineralization has been proposed. To this aim carbonate-hydroxyapatite nanocrystals which mimic for composition, structure, nanodimensions, and morphology dentine apatite crystals and resemble closely natural apatite chemical-physical properties have been used. The results underline the differences induced by the use of fluoride ions and hydroxyapatite nanocrystals in contrasting the mechanical abrasions and acid attacks to which tooth enamel is exposed. Fluoride ions generate a surface modification of the natural enamel apatite crystals increasing their crystallinity degree and relative mechanical and acid resistance. On the other hand, the remineralization produced by carbonate-hydroxyapatite consists in a deposition of a new apatitic mineral into the eroded enamel surface scratches. A new biomimetic mineral coating, which progressively fills and shadows surface scratches, covers and safeguards the enamel structure by contrasting the acid and bacteria attacks.

Copyright © 2009 Norberto Roveri et al. This is an open access article distributed under the Creative Commons Attribution License, which permits unrestricted use, distribution, and reproduction in any medium, provided the original work is properly cited.

1. Introduction

Dental erosion is the chemical wear of the dental hard tissue without the involvement of bacteria [1]. Its clinical relevance is becoming wider and wider [2–6], and it is considered one of the main tooth pathologies able to cause patient discomfort, after periodontal diseases and caries.

Its aetiology is related to the enormous increase in consumption of soft drinks, fruit juices and sport drinks consumption [7]. However, other acid sources such as drugs containing syrups, analgesics and vitamin C intake and environmental acid exposure in working conditions are claimed to be related to enamel erosion [8–12].

The mechanisms involved in the damage of dental hard tissue are the acid attacks on the outer few micrometers of the enamel, which brings to demineralization and dissolution of the mineral phase [13–16].

Hydroxyapatite is the main constituent of the dental tissues representing in enamel and dentine the 95 wt% and 75 wt%, respectively.

The primary determinant of dissolution rate is the solubility of hydroxyapatite (HA) which is related to pH, and the presence of salivary pellicle also appears to be important [17–19].

Frequent application of a high concentration of topical fluoride may be of some benefit in preventing further demineralization and increasing the abrasion resistance of erosion lesions [20].

In vitro studies have shown that synthetic carbonated-hydroxyapatite (CHA) dissolution inhibition is a logarithmic function of the fluoride concentration in solution [21].

Systemic intake of fluoride during tooth formation has been claimed to be effective in caries prevention just by means of the apatite demineralization inhibition. According

to recommended daily allowances (RDAs) panel of the European Food Safety Authority, an intake of 0.1 mg fluoride/Kg body weight/day in children up to the age of eight years can be considered as the dose below which there will be no significant occurrence of moderate forms of fluorosis in permanent teeth [22].

However, it is important to consider that fluoridated water, fluoride supplements in diet, fluoride toothpaste, and topical fluoride applications have been identified as sources of enamel fluorosis [23]. Moreover, the “probably toxic dose” of fluoride—the dose which should trigger therapeutic intervention and hospitalization—is 5 mg/Kg of body weight, but as currently packaged, many dental products contain sufficient fluoride to exceed the “probably toxic dose” for young children [24].

Most of the products and devices used to contrast enamel and dentine erosion, such as fluoride [25–28], behave by reducing apatite dissolution rather than aiming to promote mineralization through apatite crystallization or replacement of the lost mineral. Hydroxyapatite, as well as in bone, is responsible for the mechanical behavior of the dental tissues. Unlike bone, in enamel and dentine, when HA is dissolved or abraded, it cannot spontaneously remineralize because enamel contains no cells and dentine apposition occurs only toward the pulp tissues. Therefore, both enamel and dentine can be reconstructed only by the application of alloplastic materials providing a sort of prosthetic restoration. In view of this situation, the demineralized area and micrometric sized scratches, which normally occur on enamel surface as a consequence of microwear and acid attack [29], cannot be repaired biologically nor prosthetically.

Hydroxyapatite has been widely subjected to experiment as bone filler and prosthetic coating due to its biocompatibility and osteoconductivity, representing an elective material covering a wide range of applications for bone substitution and interface [30]. Poorly crystalline HA nanocrystals, in addition to the excellent biological properties of HA, such as nontoxicity and lack of inflammatory and immunity responses, have bioresorption properties under physiological conditions. This property can be modulated by modifying its degree of crystallinity, which is achieved by implementation of innovative synthesis with a nanosize crystals control. In the last decade, advanced technology has been utilized to synthesize a new generation of biomimetic apatitic alloplastic materials which can optimize the interaction with biological entities thanks to their strong surface bioactivity [31]. The aim of the present study is to highlight the effect of the synthetic biomimetic hydroxyapatite crystals respect the fluoride ions into the remineralization in vitro of human enamel surface.

2. Materials and Methods

2.1. Chemicals. All the chemicals reagents used were of high chemical grade from Sigma-Aldrich, Mo, USA.

2.2. Synthesis of Carbonate-Hydroxyapatite Nanocrystals. Plate-acicular shaped carbonate-hydroxyapatite nanocrystals

about 100 nm in size were synthesized according to a modification of the method previously reported [32] and patented [33]. CHA nanocrystals about 100 nm in size were precipitated from an aqueous suspension of $\text{Ca}(\text{OH})_2$ (0.17 M) by slow addition of H_3PO_4 (0.15 M). The reaction mixture was stirred at 37°C for 12 hours, and then stirring was suspended allowing the deposition of CHA nanocrystals. Synthesized CHA 100 nm sized nanocrystals were isolated by filtration of the mother liquor, repeatedly washed with water and freeze-dried. The fraction of plate-acicular shaped crystals about 100 nm in size with a granular dimensions ranging from 100 to 150 μm was selected for the study. Aliquot of plate-acicular shaped crystals about 100 nm in size has been allowed, after synthesis to intergrowth in the reaction mixture up to the formation of clusters having dimension ranging from about 0.5 to 3.0 μm . The cluster aggregation process has been stopped by adding a surfactant (Protelan MST35 8 wt%) in the mother solution.

Plate-shaped carbonate-hydroxyapatite nanocrystals about 20 nm sized were synthesized according to the method of Liou et al. [34] with some modifications. The nanocrystals were precipitated from an aqueous solution of $(\text{NH}_4)_3\text{PO}_4$ (5.1 mM) by slow addition of an aqueous solution of $\text{Ca}(\text{CH}_3\text{COO})_2$ (8.5 mM) keeping the pH at a constant value of 10 by addition of a NH_4OH solution. The reaction mixture was kept under stirring at room temperature for 24 hours, and then stirring was suspended allowing the deposition CHA nanocrystals. Synthesized CHA nanocrystals were isolated by filtration of the solution, repeatedly washed with water, and freeze-dried. The fraction of plate shaped crystals about 20 nm in size having granular dimensions ranging from 100 to 150 μm was selected for the study.

2.3. Morphological Characterization. Transmission electron microscopy (TEM) investigations were carried out using a Philips CM 100 instrument. The powdered samples were ultrasonically dispersed in ultrapure water, and then a few droplets of the slurry deposited on holey-carbon foils supported on conventional copper microgrids.

Scanning electron microscopy (SEM) observation was carried out by an SEM (Zeiss EVO, 40 XVP) using secondary electrons at 25 kV and various magnifications.

2.4. Structural Characterization. X-ray diffraction powder and enamel surface patterns were collected using an Analytical X'Pert Pro equipped with X'Celerator detector powder diffractometer using $\text{Cu K}\alpha$ radiation generated at 40 kV and 40 mA. The instrument was configured with a 1° divergence and 0.2 mm receiving slits. The samples were prepared using the front loading of standard aluminium sample holders which are 1 mm deep, 20 mm high, and 15 mm wide. The degree of HA crystallinity was evaluated according to the formula [35]

$$\text{crystallinity} = \left(\frac{X}{Y} \right) 100, \quad (1)$$

where X = net area of diffracted peaks, and Y = net area of diffracted peaks + background area.

Crystal domain size along the *c* direction was calculated applying Scherrer's formula

$$L_{(002)} = \frac{0.94\lambda}{\left[\cos \theta \left(\sqrt{\Delta r^2 - \Delta_0^2} \right) \right]}, \quad (2)$$

where θ is the diffraction angle for plane (002), Δr and Δ_0 are the widths in radians of reflection (002) at half height for the synthesized and the reference HA materials, respectively, and $\lambda = 1.5405 \text{ \AA}$.

2.5. Infrared Microscopy Spectral Analysis. ATR-IR spectra were recorded on a Thermo Nicolet 380 FT-IR spectrometer equipped with a commercial ATR accessory.

The infrared spectra were registered from 4000 to 400 cm^{-1} at 2 cm^{-1} resolution using a Bruker IFS 66v/S spectrometer using KBr pellets.

ATR spectra were recorded with the cell empty to be used as a blank for subsequent experiments. Samples were made by placing the powder sample onto the Ge ATR crystal. Spectra were collected by averaging 32 scans at 4 cm^{-1} resolution.

2.6. Specific Surface Area Determination. Measurements were undertaken using a Carlo Erba Sorpt 1750 instrument by measuring N_2 absorption at 77 K and adopting the well-known BET procedure [36].

2.7. Spectrophotometric Analysis. Phosphorus contents were determined spectrophotometrically as molybdovanadophosphoric acid using 1 cm quartz cell [37].

Calcium contents were measured using inductively coupled plasma (ICP) optical emission spectrometry (OES) using a Perkin Elmer Optima 4200 DV.

2.8. X-Ray Photoemission Spectroscopy (XPS). Analyses were performed in an M-Probe Instrument (SSI) equipped with a monochromatic Al $K\alpha$ source (1486.6 eV) with a spot size of 200 \times 750 μm and pass energy of 25 eV, providing a resolution for 0.74 eV. With a monochromatic source, an electron flood gun was used to compensate the build up of positive charge on the insulator samples during the analyses. 10 eV electrons were selected to perform measurements on these samples. The accuracy of the reported binding energies (BEs) was estimated to be ± 0.2 eV. The quantitative data were also accurately checked and reproduced several times (at least ten times for each sample), and the percentage error was estimated to be $\pm 1\%$.

2.9. Statistics Analysis. Determination of HA crystallite domain size along the *c* direction, bulk and surface Ca/P ratio, and specific surface area were carried out 5 times on the same synthesis product. Data are presented as mean value \pm SD. Differences were considered statistically significant at a significance level of 90%.

2.10. In Vitro Enamel Remineralization Procedures. Slabs of enamel (3 \times 3 mm) were obtained from interproximal

surfaces of premolars extracted for orthodontic reasons. After the extraction, the teeth were cut with diamond disks, and the obtained slabs were sonicated for 10 minutes in 50% ethanol in order to remove any debris. Then, the specimens were etched with 37% phosphoric acid for 1 minute. Etched slabs were washed in distilled water for 10 minutes under stirring and then air dried. Two different in vitro remineralization procedures have been performed.

The first in vitro remineralization procedure utilizes a 10 wt% CHA in the range from 100 to 150 μm granules slurries constituted of both 20 nm or 100 nm sized nanocrystals. CHA nanocrystals aqueous slurries were applied for 10 minutes on the surfaces of the enamel slabs at room temperature with 100% relative humidity and then removed by water washing and air dried.

The second in vitro remineralization process utilizes toothpaste containing both fluoride ions and CHA 0.5–3.0 μm sized clusters constituted by intergrowth of 100 nm sized nanocrystals.

Comparable etched enamel slabs were divided into 3-groups of treatment using, respectively, fluoride or CHA-based toothpaste and only water (control). Each slab was brushed three times a day for a period of 15 days. The intervals between brushing sessions were at least 5 hours. Every brushing session has been performed for 30 seconds by an electric toothbrush using constant pressure and a bean sized toothpaste aliquot wetted with tap water, closely resembling the in vivo usual tooth brushing procedure. After every treatment, the single enamel slab was washed with tap water using a cleaned toothbrush in order to remove residual toothpaste.

3. Results

3.1. Synthesis and Characterization of Biomimetic Carbonate-Hydroxyapatite Nanocrystals. Biomimetic carbonate-hydroxyapatite nanocrystals have been synthesized with a nearly stoichiometric in bulk Ca/P molar ratio of about 1.6–1.7 and containing 4 ± 1 wt% of carbonate ions replacing prevalently phosphate groups. CHA nanocrystals have been synthesized both about 100 nm and 20 nm sized with an acicular and plate morphology, respectively. TEM images of synthetic 20 nm sized CHA nanocrystals showing the plate-shaped morphology and synthetic 100 nm sized CHA nanocrystals showing the acicular morphology are reported in Figures 1(a) and 1(b), respectively.

CHA nanocrystals can aggregate in microsized crystal clusters, whose dimensions increase prolonging maturation time in mother solution at constant temperature and stirring [33].

Powder X-ray diffraction patterns of plate shaped about 20 nm sized CHA nanocrystals and acicular shaped about 100 nm sized CHA nanocrystals (see Figures 2(b) and 2(c), resp.) show characteristic diffraction maxima of an apatite single phase (JCPDS 01-074-0565).

These X-ray diffraction patterns are compared with those collected for natural carbonate hydroxyapatite from deproteinized dentine and enamel reported in Figures 2(a)

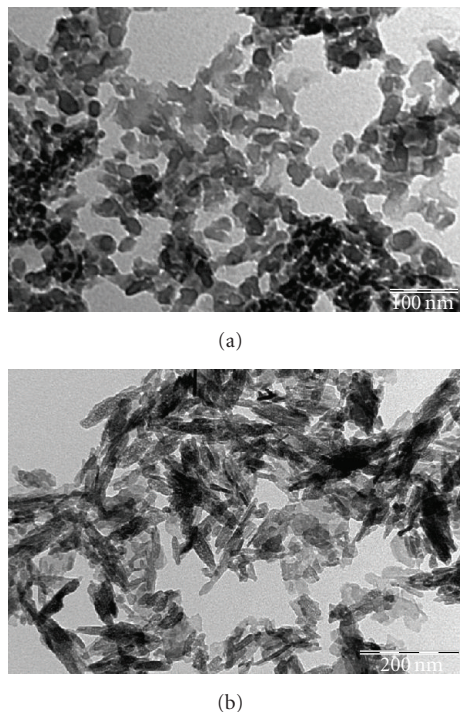


FIGURE 1: TEM images of (a) synthetic plate-shaped 20 nm sized CHA nanocrystals (scale bar = 100 nm), (b) synthetic plate-acicular 100 nm sized CHA nanocrystals (scale bars = 200 nm).

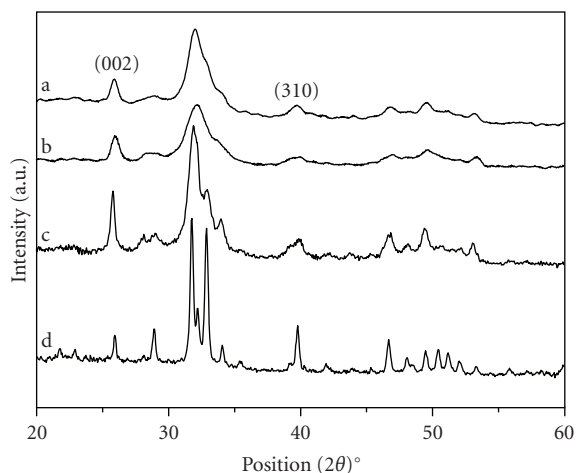


FIGURE 2: X-ray diffraction patterns of (a) natural carbonate-hydroxyapatite from deproteinized dentine, (b) synthetic plate shaped 20 nm sized CHA nanocrystals, (c) synthetic plate-acicular shaped 100 nm sized CHA nanocrystals, and (d) natural carbonate-hydroxyapatite from enamel.

and 2(d), respectively. The broadening of the diffraction maxima present in the X-ray diffraction patterns reported in Figures 2(a), 2(b), and 2(c) indicates a relatively low degree of crystallinity, which was quantified according to previous [35]. The degree of crystallinity of synthesized about 20 nm sized CHA nanocrystals with plate morphology and synthesized about 100 nm sized CHA nanocrystals with acicular

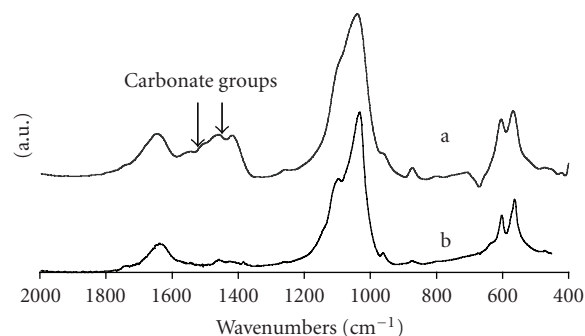


FIGURE 3: (a) FTIR spectra of synthetic 20 nm sized CHA nanocrystals, (b) natural carbonate-hydroxyapatite from deproteinized dentine.

morphology is 30% and 50%, respectively. The crystallinity degree of about 20 nm sized CHA nanocrystals is very close to that one determined from the X-ray diffraction pattern of deproteinized dentine natural carbonate-hydroxyapatite (28%) reported in Figure 2(a). Furthermore, the crystallinity degree of natural hydroxyapatite of deproteinized enamel, reported in Figure 2(d), is 70%. The crystal domain sizes along the c direction have been calculated by Scherrer's formula using the $2\theta = 26^\circ$ (002) diffraction peak of the X-ray diffraction patterns reported in Figures 2(a), 2(b), and 2(c). The calculated crystal domain sizes for 20 nm sized CHA nanocrystals and deproteinized dentine are 250 Å and 213 Å, respectively. These results obtained by X-ray diffraction investigation reveal that the crystal structures of the synthesized CHA nanocrystals are very close to that observed for natural dentine.

The same similarity can be observed from the comparison of the FTIR spectra of synthesized CHA nanocrystals and natural apatite of deproteinized dentine reported in Figures 3(a) and 3(b), respectively. In these spectra, the characteristic absorption bands of phosphate and carbonate groups are clearly resolved. The absorption band at 1468 cm^{-1} is related to the carbonate group substitution to the phosphate one, while the shoulder at 1545 cm^{-1} can be considered the contribution of the carbonate group substituting the hydroxyl group in the apatite structure. This finding reveals that synthesized CHA nanocrystals not only contain a similar carbonate amount, but also underline that the carbonate substitution to the phosphate and/or hydroxyl group is very similar in the synthetic and biological crystals.

A surface characterization of the synthetic carbonate-hydroxyapatite nanocrystals has been carried out in order to highlight their surface chemical-physical characteristic which directly interfaces and reacts with exposed dental tissues. The ATR spectra (data not shown) of the synthetic about 20 nm and 100 nm sized CHA nanocrystals reveal a 4% and 3 wt% surface carbonate, respectively. The consistent amount of surface of carbonate percentage present in synthetic CHA is appreciably higher than the surface carbonate percentage present in enamel and dentine about 2 wt% .

Specific surface area of $100\text{ m}^2\text{g}^{-1}$ and $80\text{ m}^2\text{g}^{-1}$ has been determined for 20 nm sized CHA nanocrystals with plate

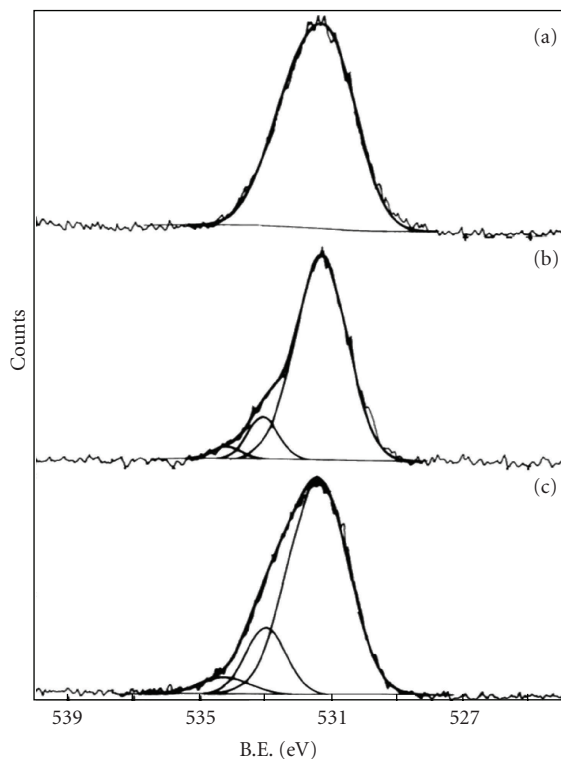
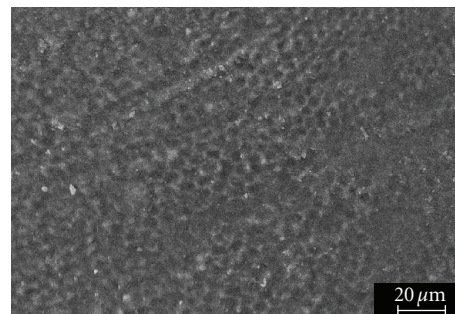


FIGURE 4: XPS analysis of spectral features of (a) the O 1s region of the enamel demineralized by orthophosphoric acid 37% for 1 minute, (b) enamel remineralized by a treatment with synthetic microclusters of CHA nanocrystals 100 nm sized for 10 minutes, and (c) synthetic microclusters of CHA nanocrystals 100 nm sized.

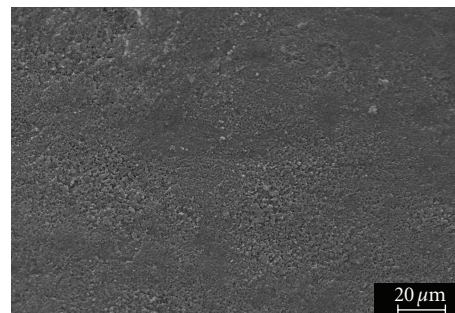
morphology and synthesized 100 nm sized CHA nanocrystals with acicular morphology, respectively. These specific surface area values obtained for synthetic nanocrystals are only slightly lower than the $110 \text{ m}^2 \text{ g}^{-1}$ obtained for biological nanocrystals.

The surface Ca/P molar ratio determined by XPS analysis for CHA nanocrystals and CHA crystals microclusters does not reveal appreciable differences and result significantly lower than Ca/P molar ratio determined by ICP analysis in bulk indicating a surface calcium deficiency probably due to surface disorder. In fact, the Ca/P molar ratios of 1.7 determined in bulk for synthetic CHA nanocrystals reduce to a value of 1.4-1.5 when determined on the crystals surface by XPS analysis (see Table 1). XPS analysis of spectral features of the O 1s region of the synthetic 100 nm sized CHA nanocrystals (see Figure 4(c)) shows a definite O 1s shape fitted by three components: a first, very intense, peak at lower BE attributed to oxygen in phosphate group, a second peak due to OH of the carbonate-hydroxyapatite, and a final peak at very high BE, which can be attributed to trapped undissociated water and carbonates.

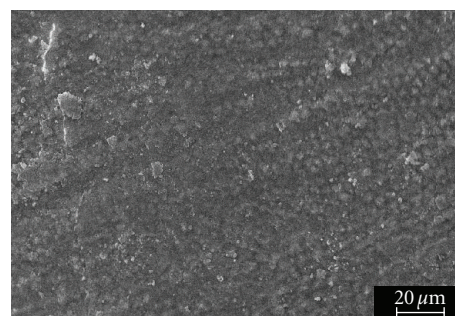
3.2. In Vitro Enamel Surface Remineralization by Biomimetic CHA Nanocrystals. SEM analysis allows investigating the morphology of both demineralized enamel and the fea-



(a)



(b)



(c)

FIGURE 5: SEM image of enamel surface after application of 37% orthophosphoric acid for 1 minutes. The etching treatment removed aprismatic layer and exposed prismatic and interprismatic hydroxyapatite structures (a), remineralized enamel surface after treatment by synthetic CHA micro-clusters constituted of nanocrystals 20 nm (b) and 100 nm sized (c) and synthetic CHA micro-clusters.

tures observed after remineralization procedures induced by biomimetic CHA nanocrystals in vitro application.

The demineralization procedure by orthophosphoric acid 37% for 1 minute removes the aprismatic enamel, and exposed hydroxyapatite prisms became evident. Figure 5(a) shows demineralization of both interprismatic and prismatic enamel structures.

After treatment for 10 minutes by aqueous slurry of both synthetic 20 nm and 100 nm sized CHA nanocrystals, the surface of the demineralized enamel appears covered by the CHA phase (see Figures 5(b) and 5(c), resp.) arranged in a thick and homogeneous apatitic layer.

XPS analysis of spectral features of the O 1s region of the enamel demineralized by orthophosphoric acid 37%

TABLE 1: XPS analysis of CHA nanocrystals, enamel tooth treated with ortophosphoric acid before and after treatment with either CHA 20 or 100 nm sized nanocrystals and after brushing with toothpaste containing booth CHA or fluoride.

| Sample | O (%) | C (%) | Ca (%) | P (%) | N (%) | Si (%) | Na (%) | F (%) | Ca/P |
|--|-------|-------|--------|-------|-------|--------|--------|-------|------|
| 20 nm CHA nanocrystals | 50.4 | 17.6 | 19.4 | 12.6 | — | — | — | — | 1.5 |
| 100 nm CHA nanocrystals | 48.4 | 18.0 | 19.6 | 13.9 | — | — | — | — | 1.4 |
| Tooth treated with ortophosphoric acid | 30.7 | 49.4 | 5.4 | 5.3 | 5.9 | 1.9 | 1.4 | — | 1.1 |
| Tooth treated with 20 nm CHA nanocrystals | 43.3 | 27.3 | 13.4 | 10.1 | 2.3 | — | 1.9 | — | 1.3 |
| Tooth treated with 100 nm CHA nanocrystals | 43.7 | 26.0 | 14.8 | 11.2 | 1.0 | — | 1.5 | — | 1.3 |
| CHA containing toothpaste | 30.7 | 51.9 | 5.5 | 4.7 | 1.6 | 5.6 | — | — | 1.2 |
| Fluoride containing toothpaste | 20.9 | 63.3 | 4.1 | 1.2 | 2.0 | 4.9 | — | 3.6 | 3.4 |

for 1 minute shows a single broad band, in which it is difficult to determine precisely and to quantify the binding energy (BE) and, therefore, the kind of the surface oxygen components (see Figure 4(a)). On the contrary, the enamel remineralized by synthetic 100 nm sized CHA nanocrystals for 10 minutes shows a definite O 1s shape fitted by three components at different binding energy (see Figure 4(b)). These components correspond to the same three ones used to fit O 1s shape recorded for synthetic 100 nm sized CHA nanocrystals (see Figure 4(c)), the first at lower BE very intense peak is attributed to oxygen in phosphate group, the second peak is due to OH of the carbonate-hydroxyapatite, and a final peak at high BE, can be attributed to trapped undissociated water and carbonate groups. These results unequivocally confirm the presence of synthetic CHA at the surface of the treated enamel and the consequent validation of the enamel remineralization. The same finding is pointed out by the ATR spectrum of enamel treated for 10 minutes by synthetic 100 nm sized CHA nanocrystals, showing appreciable higher intensity of the characteristic absorption bands of carbonate ions ($1420\text{--}1460$ and 1680 cm^{-1}) in respect of the same absorption bands present in the demineralized enamel ATR spectrum. No differences are appreciable in the phosphate ions bands ($1000\text{--}1100$ and $530\text{--}580\text{ cm}^{-1}$). ATR spectrum (data not shown) of remineralized enamel reveals that surface apatite is richer in carbonate than natural one, such as synthetic 100 nm sized CHA nanocrystals.

3.3. In Vitro Enamel Surface Remineralization by Toothpaste Containing either Fluoride or Biomimetic CHA Nanocrystals Microclusters. SEM analysis allowed us to investigate the morphology of both demineralized enamel and the features observed after a remineralization process which utilizes in vitro application of toothpaste containing either fluoride or CHA microclusters constituted of 100 nm in size nanocrystals.

The surfaces of the teeth treated with fluoride (see Figure 6(b)) were not consistently changed respect to that of demineralization by ortophosphoric acid (see Figure 6(c)). Actually both the interprismatic and prismatic enamel structures appear still evident. On the contrary after treatment of the enamel slabs with a toothpaste containing synthesized CHA microclusters constituted of 100 nm sized nanocrystals, the interprismatic and prismatic enamel structures appear to

be completely hidden by a thick homogeneous apatitic layer (see Figure 6(a)).

The XRD patterns collected on the surface of enamel slabs after treatment with CHA or fluoride toothpaste and water are reported in Figures 7(b), 7(c), and 7(d), respectively, and compared with the XRD pattern (see Figure 7(a)) of CHA microclusters constituted of 100 nm sized nanocrystals utilized to prepare the used CHA toothpaste. The XRD diffraction maxima recorded on the surface of enamel slabs treated with fluoride containing toothpaste appear slightly more sharpened than those obtained on the enamel etched slabs brushed only with water. This observation reveals an increased crystallinity degree probably due to a partial structural conversion of hydroxyapatite into fluoride substituted hydroxyapatite. On the contrary, the XRD pattern obtained on the surface of enamel slabs brushed with CHA containing toothpaste shows the broadened diffraction maxima characteristic of the synthetic biomimetic CHA, revealing its presence on the enamel surface. The CHA not removed by brushing procedures suggests the formation of chemical bonds between the synthetic CHA microclusters constituted of 100 nm sized nanocrystals and natural enamel apatite crystals. These bonds allow the formation of a persistent CHA coating on the enamel surface whose morphology was detected by SEM analysis.

The surface Ca/P molar ratio determined by XPS analysis for demineralized enamel slabs before and after in vitro remineralization by brushing whit toothpaste containing either fluoride or CHA are compared in Table 1. In this table, a comparison with the Ca/P molar ratio of CHA microclusters constituted of 100 nm sized nanocrystals also present. The enamel surface Ca/P molar ratio changes before and after the brushing treatment with toothpaste containing fluoride, assuming a value of 3.4 very different from the apatite stoichiometric one ($\text{Ca/P} = 1.7$). This finding reveals that the only structural modification of enamel hydroxyapatite induced by fluoride is restricted to a partial hydroxyl groups replacement by fluoride ions without affecting appreciably the Ca and phosphate structural network. On the contrary, enamel slabs treated with the toothpaste containing synthesised CHA microclusters of 100 nm sized nanocrystals exhibit a surface Ca/P molar ratio very similar to that one of the synthetic CHA.

This coating is highly less crystalline than native enamel apatite, and consists of a new apatitic mineral deposition

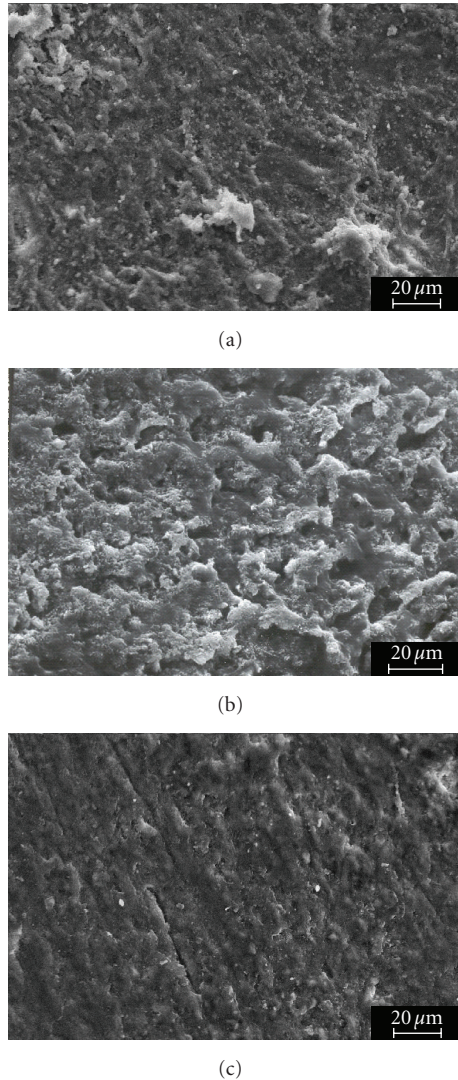


FIGURE 6: SEM images of enamel after brushing treatment with (a) CHA toothpaste containing, (b) fluoride containing toothpaste, and (c) orthophosphoric acid application.

which progressively fills the scratches and pits. On the contrary, the surface remineralization observed on the specimens treated with fluoride containing toothpaste is mainly based on chemical-physical enamel apatite surface modifications rather than a formation of a new mineral deposition.

The CHA biomimetic coating formation is a remineralization process corresponding to a new apatite deposition in the demineralized area of enamel surface.

4. Discussion

Enamel is the hardest and most mineralized tissue of human body. It is structured in order to resist to mechanical injuries, abrasion, and chemical attack. Differently from all the other mineralized tissues, it lacks proteins even if they are essential to its formation. Actually, matrix proteins are

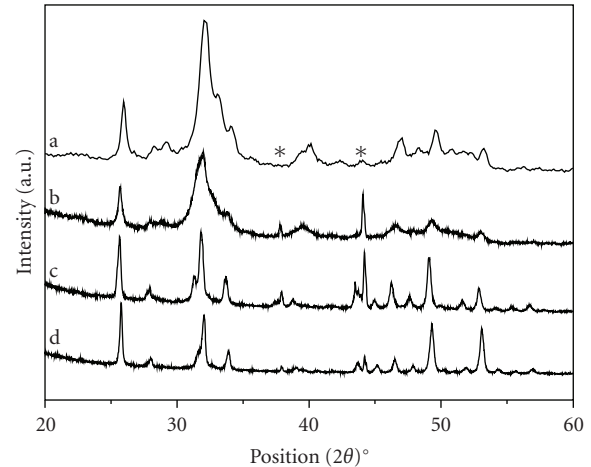


FIGURE 7: (a) XRD pattern of synthetic CHA, (b) enamel after brushing treatment with CHA containing toothpaste, (c) enamel after brushing treatment with fluoride containing toothpaste, (d) enamel after brushing treatment with water. * indicates Al holder diffraction maxima.

cleaved by proteinases secreted by the ameloblasts during tooth formation; hence, the matrix proteins of enamel are not incorporated into enamel prisms [38]. Degradation and resumption of enamel matrix proteins is the reason why enamel prisms, once formed, cannot be remodelled. After enamel prism formation, only the amount of hydroxyapatite within the prisms may decrease in consequence of chemical changes into the oral environment.

Acid attack is one of the major causes of enamel hydroxyapatite loss. It may occur even in young age as a consequence of plaque metabolism or simply due to food and beverage intakes [2–4].

In the present paper, synthetic carbonate-hydroxyapatite biomimetic nanocrystals have been chemical-physical characterized and investigated regarding the possibility to obtain an *in vitro* remineralization of the altered enamel surfaces.

The experimental model used in the present investigation was the demineralization by means of orthophosphoric acid of sound enamel of the interproximal surfaces and its subsequent remineralization.

This model was chosen because the demineralizing effect of orthophosphoric acid is well known in terms of chemical and microhistological features because it is an essential part of the procedures of adhesive restoration applications.

The SEM observations showed that the enamel is characterized by both amorphous and prismatic hydroxyapatite and by an irregular surface even. The use of orthophosphoric acid causes an exposure of prism and a loss of both interprismatic and prismatic substances.

The treatment of demineralized enamel only for ten minutes, by synthetic CHA nanocrystals, induces a consistent enamel remineralization through the formation of a surface carbonate-hydroxyapatite coating. This coating is due to the chemical bond of the synthetic CHA nanocrystals biomimetic for composition, structure, size, and morphology on the surface prismatic hydroxyapatite enamel. It can

be supposed that the application of CHA nanocrystals 20 nm sized allows a better mineralization in the lower surface fissure, because the interprismatic and prismatic enamel structures appear totally hidden. Using an equal time of treatment, the application of CHA nanocrystals 100 nm sized produces the formation of a homogeneous coating which hides interprismatic and prismatic enamel structures when examined with SEM.

In this paper, an in vitro enamel surface remineralization by brushing with toothpaste containing either fluoride or biomimetic CHA nanocrystals microclusters has been also carried out. The XRD patterns, SEM images, and XPS spectra collected on the surface of enamel slabs before and after treatment with CHA or fluoride toothpaste underline the possibility to obtain an enamel remineralization through the formation of a surface apatite coating which covers the enamel structure avoiding the most probably health dangerous fluoride effects, to contrast the mechanical abrasion and acid attacks to which tooth enamel is exposed. The documented CHA biomimetic coating formation which is less crystalline than enamel natural apatite represents an enamel repair process corresponding to an apatite deposition inside the demineralized area of enamel surface and may be considered an innovative approach to contrast enamel demineralization.

Acknowledgments

The authors acknowledge financial support from the University of Bologna, C.I.R.C.M.S.B., the Italian Ministero dell'Istruzione, Università e Ricerca (MIUR) PRIN Project no. 2006-032335, and the COSWELL President Paolo Gualandi for his cheering eagerness in suggesting this research work.

References

- [1] J. D. Eccles, "Dental erosion of nonindustrial origin. A clinical survey and classification," *The Journal of Prosthetic Dentistry*, vol. 42, no. 6, pp. 649–653, 1979.
- [2] C. Deery, M. L. Wagner, C. Longbottom, R. Simon, and Z. J. Nugent, "The prevalence of dental erosion in a United States and a United Kingdom sample of adolescents," *Pediatric Dentistry*, vol. 22, no. 6, pp. 505–510, 2000.
- [3] C. R. Dugmore and W. P. Rock, "The prevalence of tooth erosion in 12-year-old children," *British Dental Journal*, vol. 196, no. 5, pp. 279–282, 2004.
- [4] Y. H. Al-Dlaigan, L. Shaw, and A. Smith, "Dental erosion in a group of British 14-year-old, school children—part I: prevalence and influence of differing socioeconomic backgrounds," *British Dental Journal*, vol. 190, no. 3, pp. 145–149, 2001.
- [5] I. B. Arnadóttir, S. R. Sæmundsson, and W. P. Holbrook, "Dental erosion in Icelandic teenagers in relation to dietary and lifestyle factors," *Acta Odontologica Scandinavica*, vol. 61, no. 1, pp. 25–28, 2003.
- [6] J. H. Nunn, P. H. Gordon, A. J. Morris, C. M. Pine, and A. Walker, "Dental erosion—changing prevalence? A review of British national childrens' surveys," *International Journal of Paediatric Dentistry*, vol. 13, no. 2, pp. 98–105, 2003.
- [7] British Soft Drinks Association, "A shared responsibility," Annual Report, The British Soft Drinks Association, London, UK, 2002–2003.
- [8] C. C. Costa, I. C. S. Almeida, and L. C. Costa Filho, "Erosive effect of an antihistamine-containing syrup on primary enamel and its reduction by fluoride dentifrice," *International Journal of Paediatric Dentistry*, vol. 16, no. 3, pp. 174–180, 2006.
- [9] M. Kitchens and B. M. Owens, "Effect of carbonated beverages, coffee, sports and high energy drinks, and bottled water on the in vitro erosion characteristics of dental enamel," *Journal of Clinical Pediatric Dentistry*, vol. 31, no. 3, pp. 153–159, 2007.
- [10] A. Wiegand and T. Attin, "Occupational dental erosion from exposure to acids—a review," *Occupational Medicine*, vol. 57, no. 3, pp. 169–176, 2007.
- [11] A. Lussi, T. Jaeggi, and D. Zero, "The role of diet in the aetiology of dental erosion," *Caries Research*, vol. 38, supplement 1, pp. 34–44, 2004.
- [12] A. Lussi, E. Hellwig, D. Zero, and T. Jaeggi, "Erosive tooth wear: diagnosis, risk factors and prevention," *American Journal of Dentistry*, vol. 19, no. 6, pp. 319–325, 2006.
- [13] N. X. West, A. Maxwell, J. A. Hughes, D. M. Parker, R. G. Newcombe, and M. Addy, "A method to measure clinical erosion: the effect of orange juice consumption on erosion of enamel," *Journal of Dentistry*, vol. 26, no. 4, pp. 329–335, 1998.
- [14] N. X. West, J. A. Hughes, D. M. Parker, R. G. Newcombe, and M. Addy, "Development and evaluation of a low erosive blackcurrant juice drink 2. Comparison with a conventional blackcurrant juice drink and orange juice," *Journal of Dentistry*, vol. 27, no. 5, pp. 341–344, 1999.
- [15] J. A. Hughes, N. X. West, D. M. Parker, R. G. Newcombe, and M. Addy, "Development and evaluation of a low erosive blackcurrant juice drink in vitro and in situ 1. Comparison with orange juice," *Journal of Dentistry*, vol. 27, no. 4, pp. 285–289, 1999.
- [16] J. A. Hughes, N. X. West, D. M. Parker, R. G. Newcombe, and M. Addy, "Development and evaluation of a low erosive blackcurrant juice drink 3. Final drink and concentrate, formulae comparisons in situ and overview of the concept," *Journal of Dentistry*, vol. 27, no. 5, pp. 345–350, 1999.
- [17] A. V. Nieuw Amerongen, C. H. Oderkerk, and A. A. Driessen, "Role of mucins from human whole saliva in the protection of tooth enamel against demineralization in vitro," *Caries Research*, vol. 21, no. 4, pp. 297–309, 1987.
- [18] B. T. Amaechi, S. M. Higham, W. M. Edgar, and A. Milosevic, "Thickness of acquired salivary pellicle as a determinant of the sites of dental erosion," *Journal of Dental Research*, vol. 78, no. 12, pp. 1821–1828, 1999.
- [19] Y. Nekrashevych and L. Stösser, "Protective influence of experimentally formed salivary pellicle on enamel erosion: an in vitro study," *Caries Research*, vol. 37, no. 3, pp. 225–231, 2003.
- [20] D. T. Zero and A. Lussi, "Erosion—chemical and biological factors of importance to the dental practitioner," *International Dental Journal*, vol. 55, no. 4, supplement 1, pp. 285–290, 2005.
- [21] J. D. B. Featherstone, R. Glana, M. Shariati, and C. P. Shields, "Dependence of in vitro demineralization of apatite and remineralization of dental enamel on fluoride concentration," *Journal of Dental Research*, vol. 69, pp. 620–625, 1990.
- [22] European Food Safety Authority, "Opinion of the scientific panel on dietetic products, nutrition and allergies on a request

- from the Commission related to the tolerable upper intake level of fluoride," *The EFSA Journal*, vol. 192, pp. 1–65, 2005.
- [23] D. G. Pendrys and J. W. Stamm, "Relationship of total fluoride intake to beneficial effects and enamel fluorosis," *Journal of Dental Research*, vol. 69, pp. 529–538, 1990.
- [24] G. M. Whitford, "The physiological and toxicological characteristics of fluoride," *Journal of Dental Research*, vol. 69, pp. 539–549, 1990.
- [25] C. Ganss, J. Klimek, U. Schäffer, and T. Spall, "Effectiveness of two fluoridation measures on erosion progression in human enamel and dentine in vitro," *Caries Research*, vol. 35, no. 5, pp. 325–330, 2001.
- [26] C. Ganss, J. Klimek, V. Brune, and A. Schürmann, "Effects of two fluoridation measures on erosion progression in human enamel and dentine in situ," *Caries Research*, vol. 38, no. 6, pp. 561–566, 2004.
- [27] A. Wiegand and T. Attin, "Influence of fluoride on the prevention of erosive lesions—a review," *Oral Health & Preventive Dentistry*, vol. 1, no. 4, pp. 245–253, 2003.
- [28] A. Young, P. S. Thrane, E. Saxegaard, G. Jonski, and G. Rölla, "Effect of stannous fluoride toothpaste on erosion-like lesions: an in vivo study," *European Journal of Oral Sciences*, vol. 114, no. 3, pp. 180–183, 2006.
- [29] M. F. Teaford, "A review of dental microwear and diet in modern mammals," *Scanning Microscopy*, vol. 2, no. 2, pp. 1149–1166, 1988.
- [30] N. Roveri and B. Palazzo, "Hydroxyapatite nanocrystals as bone tissue substitute," in *Tissue, Cell and Organ Engineering*, C. S. S. R. Kumar, Ed., vol. 9 of *Nanotechnologies for the Life Sciences*, pp. 283–307, Wiley-VCH, Weinheim, Germany, 2006.
- [31] B. Palazzo, M. Iafisco, M. Laforgia, et al., "Biomimetic hydroxyapatite-drug nanocrystals as potential bone substitutes with antitumor drug delivery properties," *Advanced Functional Materials*, vol. 17, no. 13, pp. 2180–2188, 2007.
- [32] E. Landi, A. Tampieri, G. Celotti, and S. Sprio, "Densification behaviour and mechanisms of synthetic hydroxyapatites," *Journal of the European Ceramic Society*, vol. 20, no. 14–15, pp. 2377–2387, 2000.
- [33] S. P. A. Coswell, G. Gazzaniga, N. Roveri, et al., "Biologically active nanoparticles of a carbonate-substituted hydroxyapatite, process for their preparation and compositions incorporating the same," EU patent no. 005146, 2006.
- [34] S.-C. Liou, S.-Y. Chen, H.-Y. Lee, and J.-S. Bow, "Structural characterization of nano-sized calcium deficient apatite powders," *Biomaterials*, vol. 25, no. 2, pp. 189–196, 2004.
- [35] Z. E. Erkmén, "The effect of heat treatment on the morphology of D-Gun sprayed hydroxyapatite coatings," *Journal of Biomedical Materials Research Part B*, vol. 48, no. 6, pp. 861–868, 1999.
- [36] S. Brunauer, P. H. Emmett, and E. Teller, "Adsorption of gases in multimolecular layers," *Journal of the American Chemical Society*, vol. 60, no. 2, pp. 309–319, 1938.
- [37] K. P. Quinlan and M. A. DeSesa, "Spectrophotometric determination of phosphorus as molybdovanadophosphoric acid," *Analytical Chemistry*, vol. 27, no. 10, pp. 1626–1629, 1955.
- [38] J. P. Simmer and A. G. Fincham, "Molecular mechanisms of dental enamel formation," *Critical Reviews in Oral Biology and Medicine*, vol. 6, no. 2, pp. 84–108, 1995.

Research Article

Fabrication and Transport Properties of Manganite-Polyacrylamide-Based Composites

Viorel Sandu,¹ Stelian Popa,¹ Ion Ivan,¹ Carmen Plapcianu,¹ Elena Sandu,² Camelia Mihailescu,³ and Florica Doroftei³

¹National Institute of Materials Physics, 105b Atomistilor street, Magurele 077125, Romania

²Horia Hulubei National Institute of Physics and Nuclear Engineering, 407 Atomistilor Street, 077125 Magurele, Romania

³Department of Natural and Synthetic Polymers, The "Gheorghe Asachi" Technical University of Iasi, 700050 Iasi, Romania

Correspondence should be addressed to Viorel Sandu, vsandu@infim.ro

Received 15 October 2008; Revised 13 January 2009; Accepted 27 January 2009

Recommended by Alan K. T. Lau

We present the fabrication and transport properties of a series of composites made of $\text{La}_{2/3}\text{Sr}_{1/3}\text{MnO}_3$ and acrylamide-based copolymers. The most important result is the very narrow transition, of only 27 K, displayed by the peak that appears around the metal-insulator transition of the composites made with poly(acrylamide-vinylacetate). Although the amount of polymer is rather low, different copolymers change drastically the electric transport characteristics.

Copyright © 2009 Viorel Sandu et al. This is an open access article distributed under the Creative Commons Attribution License, which permits unrestricted use, distribution, and reproduction in any medium, provided the original work is properly cited.

1. Introduction

Polycrystalline structures based on perovskitic manganites which display colossal magnetoresistance (CMR) have been the subject of intense research during the last decade because of the great expectations for application of their low field magnetoresistance (see [1–4] and therein references). Although the mechanism leading to the colossal magnetoresistance in polycrystals is not completely understood, the key role of grain borders is unanimously accepted in the transport process. Therefore, a wealth of data reports on experiments trying to control and improve the grain border/intergrain area and further to decipher the underlying physics. It is considered that the magnetic disorder at the interface enhances the spin dependent scattering in that area. As the charge and spin transport occur by tunneling and hopping, many attempts to improve the barrier were made by dilution with a second non-CMR material [5–12]. The dilution not only modifies the barrier geometry but also produces a kind of conditioning by changing the magnetic structure and interactions at the grain border.

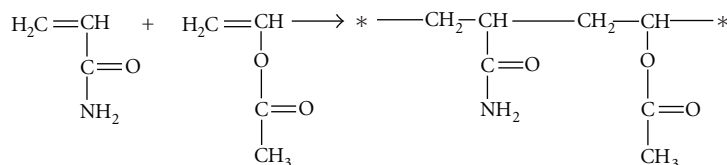
An interesting way of managing the grain surface is the dressing of the manganite grains with a very thin polymer layer. Consequently, the sintering involves only the polymeric

interface, hence, requires much lower temperatures and sintering time as compared to the use of oxides. The low processing temperatures are also beneficial for the grain cores since they are no more influenced by interdiffusion. In addition, the use of polymers increases the resistance of the interface, hence, of the whole sample, with orders of magnitude. There are few data concerning the use of polymers in conjunction with CMR manganites by our knowledge, only polyparaphenylene [13, 14], poly(methyl methacrylate) [15], and polyphenylene sulfide [16] have been reported in combination with manganites.

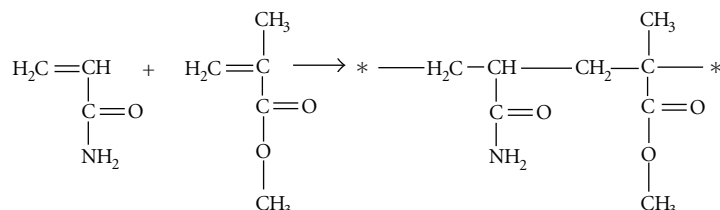
In this paper, we present the use of an acrylamide-vinylacetate copolymer to obtain manganite-polymer composite. The reason is that polyacrylamide and its copolymers are amongst the most used polymers in composite materials due to their outstanding capacity of wrapping the grains. In addition, they confer good mechanical properties to the composite samples.

2. Experimental

The manganite $\text{La}_{2/3}\text{Sr}_{1/3}\text{MnO}_3$ (LSMO) was prepared starting from La_2O_3 , SrCO_3 , and MnO_2 mixed together in warm citric acid (80°C) in the appropriate molar ratio (La:Sr:Mn



SCHEME 1



SCHEME 2

= 0.67:0.33:1). A transparent brownish gel was obtained which further was dried for 5 hours at 150°C in the oven, when a glassy solid oxide precursor could be separated. The precursor was further annealed at 1200°C in air for 12 hours. The complexes formed in both cases were characterized by elemental chemical analysis, TGA, IR spectroscopy, and nitrogen absorption (BET).

Acrylamide-vinylacetate copolymer (PAAm-VAc) was prepared by free radical polymerization of the comonomer mixture (feed molar ratio = 1/1). Aqueous medium copolymerization, initiated by the redox system $\text{K}_2\text{S}_2\text{O}_8/\text{Na}_2\text{S}_2\text{O}_5$, was carried out at 65°C following the reaction illustrated in Scheme 1.

At the end of the reaction, after 120 minutes, the reaction product was precipitated in methanol, filtered off, and washed several times. Subsequently, the polymer was dried to constant weight at 50°C. The polymer yield, gravimetrically determined, was over 50% (54.47%).

Differential scanning calorimetry (DSC) data showed a softening temperature of 157°C.

For the synthesis of poly(acrylamide-co-methyl methacrylate) (PAAm-MMA), was applied the microwave assisted copolymerization. The reaction was carried out in glass vessels without stirring, with 1% AIBN as radical initiator and dimethylsulfoxide solvent for microwave absorption. Microwaves have the advantage of a rapid and uniform heating so that the radical initiator decomposes almost instantaneously. Consequently, the concentration of the primary radicals is very high; hence, an increased efficiency is expected. In addition, the thermal degradation process is very limited. The copolymerization with methyl methacrylate followed the reaction illustrated in Scheme 2. Finally, the copolymer was conditioned in the same way as described for PAAm-VAc. Nevertheless, in this case the polymer yield is rather low 22.7% for five minutes reaction time. DSC data of this copolymer shows a softening temperature of 178°C.

The composites were prepared by dipping the manganite powder within appropriate solutions of copolymer in chloroform. The powder obtained after drying at room temperature was pelletized in bar shape at 20 kgf/cm² and sintered in an oven at 150°C for one hour. We prepared three types of $\text{La}_{2/3}\text{Sr}_{1/3}\text{MnO}_3$ -PAAm-VAc composites with 2%, 4%, and 6% copolymer, respectively. For transport measurements, four copper leads were attached to each pellet by ultrasonic soldering with Cerasolzer.

The electrical resistance was measured using the four probes technique with currents between 1 nA and 1 μA . Because of the polymer matrix, the temperature for measurements was limited at 325 K; therefore, it was difficult to reach the full paramagnetic state of the manganites that was reported at high temperatures.

3. Results and Discussion

The temperature T dependence of the resistance R follows a dependence that roughly reminds the general behavior of fined grained manganites. However, the type of polymer has strong influence on the particular characteristics of each sample.

In the case of the composites with PAAm-VAc, as the temperature decreases, the resistance, of order 0.1–0.9 M Ω , starts to increase very fast reaching a narrow peak followed by a steep metal-insulator transition at lower temperatures. For a further decrease of the temperature, the resistance shows a dip followed by an increase toward a temperature-independent resistance. Figure 1 shows the evolution of the resistance normalized to the peak resistance R_{MI} as a function of the temperature normalized to the metal-insulator transition temperature T_{MT} , measured with a current of 100 nA. What is outstanding is the width of the peak which is the narrowest ever reported, by our knowledge, only 27 K at half width. A second special feature is the wide T range, between 10 and 200 K, where the resistance keeps

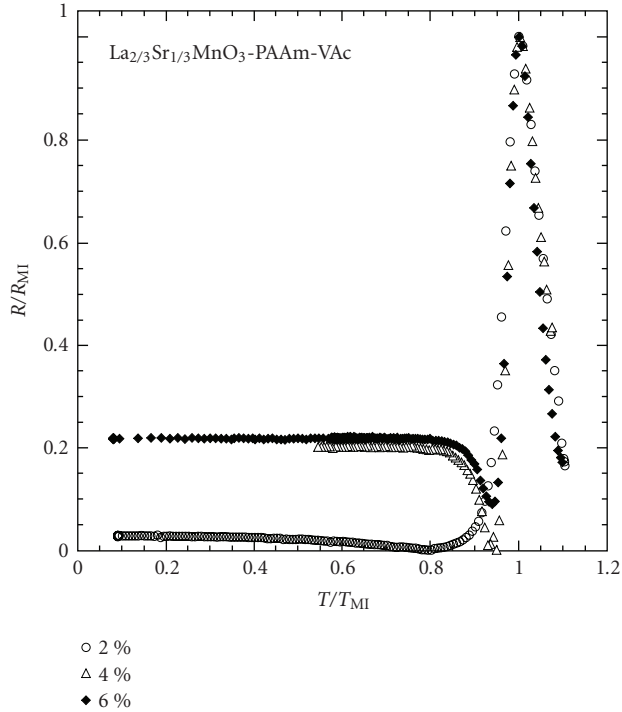


FIGURE 1: Temperature dependence of the relative resistance R/R_{MI} for a series of composites made from $\text{La}_{2/3}\text{Sr}_{1/3}\text{MnO}_3$ with 2; 4; and 6% poly(acrylamide-co-vinylacetate) (PAAm-VAc).

an almost constant value. In addition, in this representation, all peaks collapse onto one curve. Magnetic measurements have shown that the paramagnetic to ferromagnetic phase transition occurs at temperatures higher than the limitations imposed by the material composition (325 K); hence, the material is in ferromagnetic state in the temperature range $269 \leq T \leq 305$ K where T_{MI} is located. A simple model for the increase of the resistance in the ferromagnetic state was presented by Yuan et al. [17] that consider the distribution of grain separation and an exchange coupling between grains that can change the sign with the distance between grain borders. As a result, the conductance has a spin dependent contribution due to the ferromagnetic coupling that depends on the grain magnetization and a second contribution which is almost constant mirroring the antiferromagnetic coupling. The latter term behaves like an activated transport; specifically the conductance decreases fast with decreasing T while the conductance due to the ferromagnetically coupled grains increases and becomes constant at low temperature where it is dominant. Thus, the interplay of the conductances could explain both the peak and the constant resistance at low temperatures.

The role of the copolymer is not very clear in this model, but experimentally we found it is very important. For the sake of comparison, we have tried a second copolymer, poly(acrylamide-co-methyl methacrylate) (PAAm-MMA) with the same manganite. Although the amount of polymer was only 2% in both cases, the differences between LSMO-PAAm-VAc and LSMO-PAAm-MMA composites are

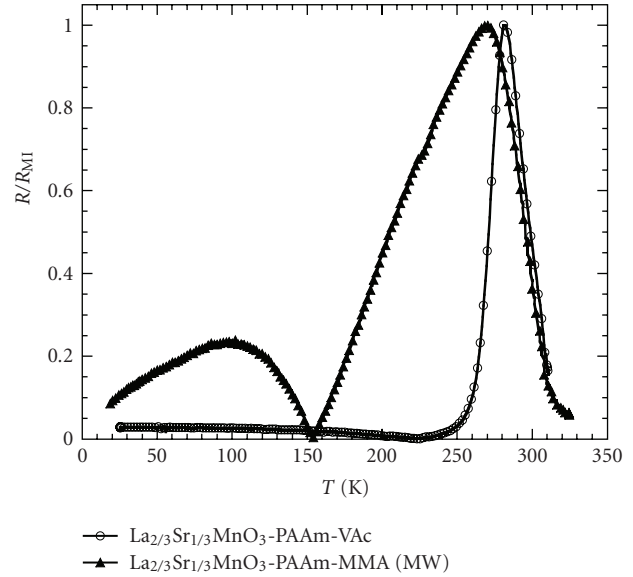


FIGURE 2: Comparison between temperature dependence of two composites made from $\text{La}_{2/3}\text{Sr}_{1/3}\text{MnO}_3$ and 2% poly(acrylamide-co-vinylacetate) (PAAm-VAc) and the same manganite with 2% poly(acrylamide-co-methyl methacrylate) (PAAm-MMA).

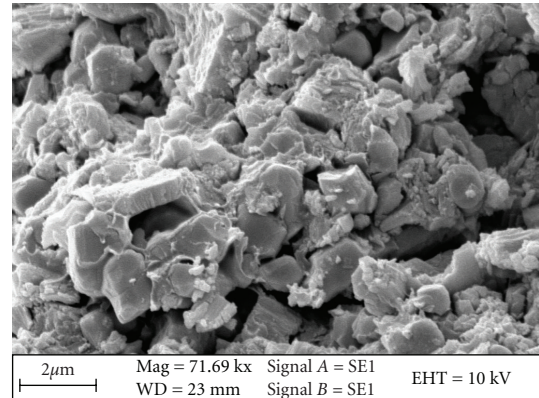


FIGURE 3: SEM micrograph of the composite made of $\text{La}_{2/3}\text{Sr}_{1/3}\text{MnO}_3$ and 2% poly(acrylamide-co-vinylacetate).

noticeable (Figure 2). The T_{MI} of the latter shifts to lower temperatures and the metal-insulator transition is broad. Actually, the whole peak is four times broader than for LSMO-PAAm-VAc. In addition, a low temperature peak appears around 100 K which is rather broad but well defined.

The SEM micrograph of the fracture of the LSMO-PAAm-VAc sample shows a uniform covering of each manganite grain (Figure 3). In the case of the LSMO-PAAm-MMA sample, the polymer appears like a network which separates large clusters of grains (Figure 4). Therefore, in the first case, the polymer acts only at the level of the intergrain tunneling barrier. In the latter case, the presence of the polymer network-like structure, which encloses large clusters of grains, leads to extra barriers. In addition, we

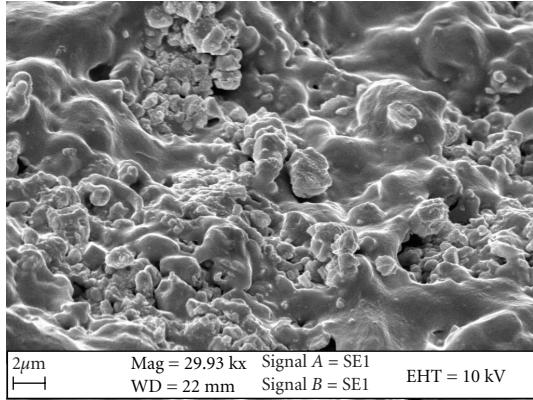


FIGURE 4: SEM micrograph of the composite made of $\text{La}_{2/3}\text{Sr}_{1/3}\text{MnO}_3$ and 2% poly(acrylamide-co-methyl methacrylate).

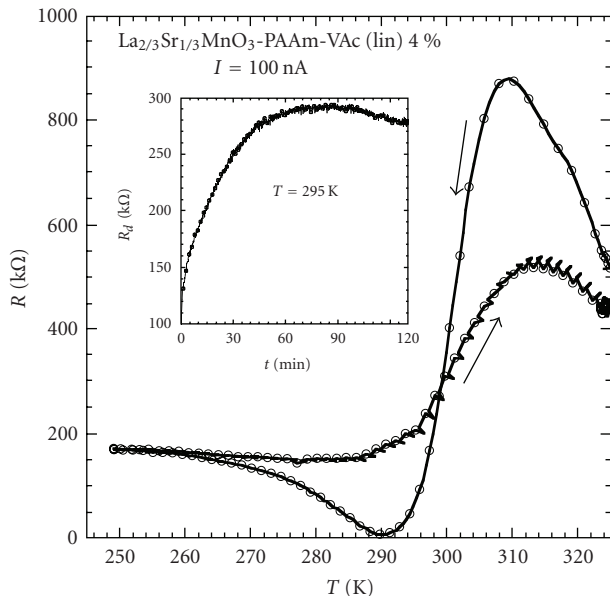


FIGURE 5: History dependence of the resistance of a composite made from $\text{La}_{2/3}\text{Sr}_{1/3}\text{MnO}_3$ with 4% poly(acrylamide-co-vinylacetate) PAAm-Vinylacetate (lin). Inset: time evolution of the resistance at 290 K for a feeding current of 100 nA.

cannot rule out a temperature dependence of the intergrain contacts due to the dramatic change of the elastic properties of the polymer network as well as the difference in the thermal expansion of the two constituents: manganite and polymer.

Finally, we mention the history dependent resistance of the LSMO-PAAm-Vac composite. There is a significant difference between the R - T dependence when the sample is warmed up after the resistance was measured in a cooling down process. As Figure 5 shows, during the warming process after the first cooling down process, the dip vanishes and the peak decreases with almost 40%. Most likely, this is an effect of phase separation which is typical for manganites

[18–22]. The border between the conductive and dielectric phases is moved by the measuring current; hence, the second run finds another phase arrangement with lower resistance at the peak. The inset to Figure 5 shows the time increase of the resistance for a constant current of 100 nA and at constant temperature close to the dip. A delay of several hours at room temperature without any transport current running through the sample reestablishes the initial state and the R - T curve recovers its initial variation.

In summary, we have fabricated composites with $\text{La}_{2/3}\text{Sr}_{1/3}\text{MnO}_3$ - and polyacrylamide-based copolymers: poly(acrylamide-co-vinylacetate) and, for comparison, poly(acrylamide-co-methyl-methacrylate). The samples with PAAm-VAc display a transition from paramagnetic to ferromagnetic phase with a very narrow breadth, of only 27 K at the half resistance peak, which is the narrowest value, yet reported. An attempt of explanation was made based on the model of oscillatory exchange coupling between grains. A history-dependent process and its relaxation were also revealed.

Acknowledgment

The work was supported by the Romanian NASR in the framework of the PN II Project 72–151.

References

- [1] M. Ziese, “Extrinsic magnetotransport phenomena in ferromagnetic oxides,” *Reports on Progress in Physics*, vol. 65, no. 2, pp. 143–249, 2002.
- [2] K. Dörr, “Ferromagnetic manganites: spin-polarized conduction versus competing interactions,” *Journal of Physics D*, vol. 39, no. 7, pp. R125–R150, 2006.
- [3] E. Dagotto, S. Yunoki, C. Şen, G. Alvarez, and A. Moreo, “Recent developments in the theoretical study of phase separation in manganites and underdoped cuprates,” *Journal of Physics: Condensed Matter*, vol. 20, no. 43, Article ID 434224, 7 pages, 2008.
- [4] P. K. Siwach, H. K. Singh, and O. N. Srivastava, “Low field magnetotransport in manganites,” *Journal of Physics: Condensed Matter*, vol. 20, no. 27, Article ID 273201, 43 pages, 2008.
- [5] Y.-H. Huang, S. Wang, F. Luo, S. Jiang, and C.-H. Yan, “Enhanced magnetoresistance at high temperatures in $\text{La}_{0.7}\text{Sr}_{0.3}\text{MnO}_3$ /silica nanocomposites,” *Chemical Physics Letters*, vol. 362, no. 1–2, pp. 114–118, 2002.
- [6] I. L. Balcells, A. E. Carrillo, B. Martínez, and J. Fontcuberta, “Enhanced field sensitivity close to percolation in magnetoresistive $\text{La}_{2/3}\text{Sr}_{1/3}\text{MnO}_3/\text{CeO}_2$ composites,” *Applied Physics Letters*, vol. 74, no. 26, pp. 4014–4016, 1999.
- [7] D. K. Petrov, L. Krusin-Elbaum, J. Z. Sun, C. Feild, and P. R. Duncombe, “Enhanced magnetoresistance in sintered granular manganite/insulator systems,” *Applied Physics Letters*, vol. 75, no. 7, pp. 995–997, 1999.
- [8] S. Gupta, R. Ranjit, C. Mitra, P. Raychaudhuri, and R. Pinto, “Enhanced room-temperature magnetoresistance in $\text{La}_{0.7}\text{Sr}_{0.3}\text{MnO}_3$ -glass composites,” *Applied Physics Letters*, vol. 78, no. 3, pp. 362–364, 2001.

- [9] S. Karmakar, S. Taran, B. K. Chaudhuri, et al., "Study of grain boundary contribution and enhancement of magnetoresistance in $\text{La}_{0.67}\text{Sr}_{0.33}\text{MnO}_3/\text{V}_2\text{O}_5$ composites," *Journal of Physics D*, vol. 38, no. 20, pp. 3757–3763, 2005.
- [10] A. Gaur, G. D. Varma, and H. K. Singh, "Enhanced low field magnetoresistance in $\text{La}_{0.7}\text{Sr}_{0.3}\text{MnO}_3/\text{TiO}_2$ composite," *Journal of Physics D*, vol. 39, no. 16, pp. 3531–3535, 2006.
- [11] D. Das, C. M. Srivastava, D. Bahadur, A. K. Nigam, and S. K. Malik, "Magnetic and electrical transport properties of $\text{La}_{0.67}\text{Ca}_{0.33}\text{MnO}_3$ (LCMO): $x\text{ZnO}$ composites," *Journal of Physics: Condensed Matter*, vol. 16, no. 23, pp. 4089–4102, 2004.
- [12] L. E. Hueso, J. Rivas, F. Rivadulla, and M. A. López-Quintela, "Magnetoresistance in manganite/alumina nanocrystalline composites," *Journal of Applied Physics*, vol. 89, no. 3, pp. 1746–1750, 2001.
- [13] C.-H. Yan, Y.-H. Huang, X. Chen, C.-S. Liao, and Z.-M. Wang, "Improvement of magnetoresistance over a wide temperature range in $\text{La}_{2/3}\text{Sr}_{1/3}\text{MnO}_3$ /polymer composites," *Journal of Physics: Condensed Matter*, vol. 14, no. 41, pp. 9607–9614, 2002.
- [14] L. K. Gil, E. Baca, O. Morán, C. Quinayas, and G. Bolaños, "Electrical transport properties of sintered granular manganite/insulator systems," *Solid State Communications*, vol. 145, no. 1-2, pp. 66–71, 2008.
- [15] J. Kumar, R. K. Singh, P. K. Siwach, H. K. Singh, R. Singh, and O. N. Srivastava, "Low field magneto-transport in LBSMO-PMMA composite," *Journal of Magnetism and Magnetic Materials*, vol. 299, no. 1, pp. 155–160, 2006.
- [16] A. Gaur and G. D. Varma, "Improved magnetotransport in LCMO-polymer (PPS) composite," *Solid State Communications*, vol. 144, no. 3-4, pp. 138–143, 2007.
- [17] S. L. Yuan, Z. C. Xia, L. Liu, et al., "Electrical transport in manganite granular systems," *Physical Review B*, vol. 68, no. 18, Article ID 184423, 5 pages, 2003.
- [18] E. Dagotto, T. Hotta, and A. Moreo, "Colossal magnetoresistant materials: the key role of phase separation," *Physics Report*, vol. 344, no. 1–3, pp. 1–153, 2001.
- [19] L. Zhang, C. Israel, A. Biswas, R. L. Greene, and A. de Lozanne, "Direct observation of percolation in a manganite thin film," *Science*, vol. 298, no. 5594, pp. 805–807, 2002.
- [20] M. Tokunaga, Y. Tokunaga, and T. Tamegai, "Imaging of percolative conduction paths and their breakdown in phase-separated $(\text{La}_{1-y}\text{Pr}_y)_{0.7}\text{Ca}_{0.3}\text{MnO}_3$ with $y = 0.7$," *Physical Review Letters*, vol. 93, no. 3, Article ID 037203, 4 pages, 2004.
- [21] E. Dagotto, "Open questions in CMR manganites, relevance of clustered states and analogies with other compounds including the cuprates," *New Journal of Physics*, vol. 7, article 67, pp. 1–28, 2005.
- [22] W. Wu, C. Israel, N. Hur, S. Park, S.-W. Cheong, and A. de Lozanne, "Magnetic imaging of a supercooling glass transition in a weakly disordered ferromagnet," *Nature Materials*, vol. 5, no. 11, pp. 881–886, 2006.

Research Article

Antibacterial Properties of Nanosilver PLLA Fibrous Membranes

Lin Li,¹ Yi Li,¹ Jiashen Li,¹ Lei Yao,¹ Arthur F. T. Mak,² Frank Ko,³ and Ling Qin⁴

¹Institute of Textiles and Clothing, The Hong Kong Polytechnic University, Kowloon, Hong Kong

²Department of Health Technology and Informatics, The Hong Kong Polytechnic University, Kowloon, Hong Kong

³Department of Materials Engineering, AMPEL, The University of British Columbia, Vancouver, BC, Canada

⁴Department of Orthopaedics and Traumatology, The Chinese University of Hong Kong, Shatin, Hong Kong

Correspondence should be addressed to Yi Li, tcliyi@inet.polyu.edu.hk

Received 15 October 2008; Revised 13 March 2009; Accepted 24 April 2009

Recommended by Alan K. T. Lau

Nanosilver has been studied as a valuable material for its strong antibacterial effects. In this study, we investigated the antibacterial properties of nano silver Poly-L-Lactic acid (Ag/PLLA) composite fibrous membranes. Ag/PLLA fibrous membranes were prepared with silver nanoparticles having weight ratio of silver nanoparticles to PLLA at 5% (w/w). In vitro antibacterial tests were performed using *Escherichia coli* (E. coli) and *Staphylococcus aureus* (Staph.) to determine the antibacterial capability of the Ag/PLLA fibrous membranes. As the results suggested, Ag/PLLA fibrous membranes showed strong antibacterial properties. Thus, Ag/PLLA fibrous membrane can be used as an antibacterial scaffold for tissue engineering.

Copyright © 2009 Lin Li et al. This is an open access article distributed under the Creative Commons Attribution License, which permits unrestricted use, distribution, and reproduction in any medium, provided the original work is properly cited.

1. Introduction

Tissue engineering scaffolds which are supposed to be used for medical applications have applied various polymers such as degradable Poly-L-Lactide (PLLA) and Polyglycolic acid (PGA), or natural biomaterials like chitin, silk, protein, and collagen [1–13]. These biomaterials offer a promising new approach to help to restore and reconstruct defected tissues. An optimal scaffold for medical applications requires the following merits: suitable for cell adhesion and proliferation; highly porous for transport of nutrients and metabolic waste; biodegradable and bioresorbable. PLLA is a biocompatible, biodegradable, and immunologically inert synthetic polymer. Thus, PLLA was chosen in this study for designing a composition of tissue engineering scaffold.

In addition, the risk of infection requires tissue engineering scaffolds to have antibacterial properties [14]. For example, during the treatment of wound, infection is a common risk that needs to be prevented for good healing of wound. Due to their strong antibacterial properties and low toxicity, silver and its compounds have been studied for many years not only for their low toxicity, but also for their antibacterial activity [14–27]. Yeo et al. found that fibers having silver showed excellent antibacterial property [28]. Electrospinning technique was employed to produce PLLA

fibers to provide a matrix with wide interface for combining antibacterial materials.

Meanwhile, the nanotechnology has provided a most promising field for the new attempts of biomedical materials [14]. Such as silver nanoparticles provide larger interface to the environment than that of microscale silver particles. Li et al. (2005) reported that nanosilver had strong antibacterial efficacy with very small amount against bacteria [17]. So, nanosized silver is a good material to reduce the quantity without decreasing antibacterial activity of silver. Thus, in this study, we used the silver nanoparticles to combine with PLLA by using electrospinning technique to fabricate biodegradable tissue engineering scaffolds with antibacterial property. E. coli and Staphylococcus which often infect wound skin and other tissues were applied for antibacterial tests to investigate the antibacterial activity of Ag/PLLA fibrous membranes [28].

2. Materials and Methods

2.1. Materials. Poly-L-Lactide (PLLA) with molecular weight of 1 000 000 was purchased from Purac, Netherlands. Silver nanoparticles (0–100 nm) with 99.9% purity and 35 nm average particle size (Figure 1) were purchased from the Shenzhen Junye Nano Material Co. Ltd.

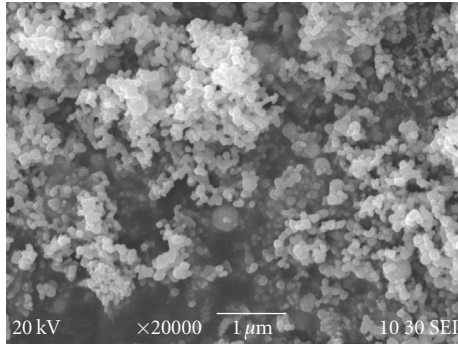


FIGURE 1: SEM images of silver nanoparticle (20 kV). Silver nanoparticles are grey and white color with the average particle size of 35 nm.

2.2. Electrospinning of PLLA and Ag/PLLA Membranes. Electrospinning method is according to our previous study [29]. PLLA was dissolved at the weight ratio of 1% in an organic solvent mixed with the composition of chloroform and N,N-dimethylformamide (DMF) (10 : 1, w/w). Silver nanoparticles were then added to the solution and stirred evenly to prepare 5% Ag/PLLA solution for electrospinning. PLLA and Ag/PLLA solutions were taken in a syringe with blunt needle, and fed by syringe plunger at a feeding rate of 0.3 mL/min. A grounded metal rotating drum wrapped with aluminum foil was located at a fixed distance of 10 cm away from the nozzle of the needle for collecting fibers. A high electric field was applied to the droplet which was coming out from the nozzle. This leads to the droplet deformation of continuous fibers. PLLA and Ag/PLLA fibrous membranes were produced under high voltage of 13 kV.

2.3. Antibacterial Test. Antibacterial test method was referred to AATCC147-2004 in this study. *Escherichia coli* (*E. coli*, ATCC25922) and *Staphylococcus aureus* (*Staph.*, ATCC25923) were used for this test as the common microorganisms involved in hospital-acquired infections [17]. The test repeated three times for every specimen.

2.3.1. Procedure. The strains were cultured overnight in 10 mL nutrient broth to achieve the turbidity of 10^8 colony forming units (CFU)/mL. Sterilized nutrient agar was dispensed by pouring 15 ± 2 mL into each standard (15×100 mm) flat bottom petri dish to obtain firmly solid agar before inoculating. Using a 4 mm inoculating loop, loaded one loopful of the 10 times diluted inoculums and transfer to the surface of the sterile agar by making five streaks coving the central area of a petri dish. Gently press the specimen of Ag/PLLA membrane to contact intimately with the agar surface. Then incubated at 37°C for 24 hours. PLLA membrane was used as a negative control. All specimens were prepared with the diameter of 5 mm for antibacterial test.

2.3.2. Evaluation. Examine the incubated plates for interruption of growth along the streaks of inoculum beneath the specimen and for a clear zone of inhibition beyond its edge.

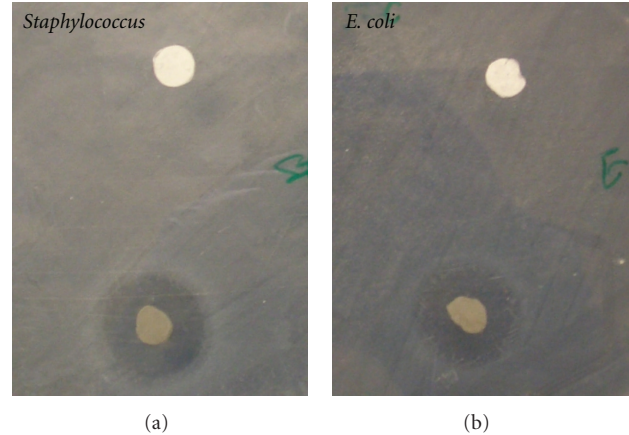


FIGURE 2: Antibacterial test results of Ag/PLLA using *Staphylococcus* (a) and *E. coli* (b) were used. The bacteria inhibition clear zones of both *E. coli* and *Staph.* can be observed around the Ag/PLLA membranes (lower specimen) with the average width of 5 mm after 24 hours incubation.

The average width of a zone of inhibition along a streak on either side of the test specimen was calculated using the following equation:

$$W = \frac{(T - D)}{2}, \quad (1)$$

where W = width of clear zone of inhibition in mm; T = total diameter of test specimen and clear zone in mm; D = diameter of the test specimen in mm.

2.4. Scanning Electron Microscopy (SEM). PLLA and Ag/PLLA fibrous membranes with bacteria were sputter coated with gold, then observed by scanning electron microscopy (LEICA, Stereoscan 440, 20 kV).

2.5. Statistical Analysis. Values were expressed as means \pm standard deviations. Statistical differences were determined by one-way ANOVA. P values of less than .05 were considered to be statistically significant.

3. Results

3.1. Antibacterial Activities of Ag/PLLA Fibrous Membranes. *E. coli* and *Staph.* were used for this test to evaluate the antibacterial capability of Ag/PLLA fibrous membranes. The bacteria were cultured overnight in 10 mL nutrient broth to achieve the turbidity of 10^8 colony forming units (CFU)/mL. A loop of each kind of bacteria at the concentration of 10^8 CFU/mL was taken to evenly streak the agar filled petri dishes. Each of the circular specimens with 5 mm diameter was gently pressed on the inoculated agar surface before incubation at 37°C for 24 hours.

As shown in Figure 2, the upper specimens were PLLA membranes, the lower specimens were Ag/PLLA membranes. All the membranes were freshly prepared. After 24 hours incubation, obvious bacteria inhibition clear zones of

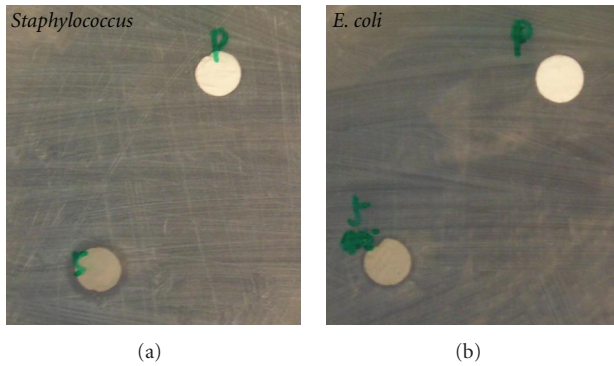


FIGURE 3: Antibacterial activity of Ag/PLLA fibrous membrane (lower specimen) reduced after exposure in the air for 8 weeks. The average width of *E. coli* and *Staph.* inhibition clear zones decreased to 1.2 mm and 1.5 mm, respectively, after 24 hours incubation.

Ag/PLLA membranes could be seen, the average width of the zones was 55.0 ± 0.1 mm. While no clear zone of inhibition was seen around PLLA membranes. Both *Staph.* and *E. coli* had the same results which indicated the strong antibacterial activity of Ag/PLLA.

After exposure in the air for 8 weeks, Ag/PLLA membranes were still observed antibacterial activity. The average width of bacterial inhibition zones of Ag/PLLA membranes was 1.2 ± 0.1 mm with *E. coli*, and 1.5 ± 0.1 mm with *Staph.* According to Table 1, the antibacterial activity was found to decrease significantly (see Figure 3).

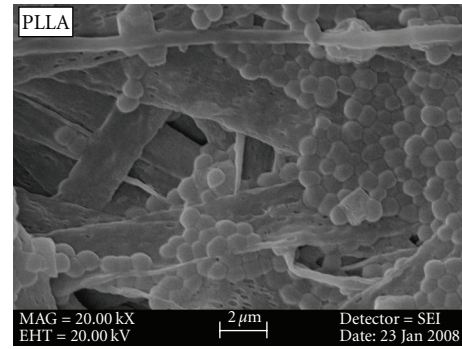
These results showed that Ag/PLLA membranes had strong antibacterial capability. Although the membranes were exposure in the air for a long term, they were still antibacterial.

3.2. SEM Observation of *Staph.* on PLLA and Ag/PLLA Fibrous Membranes. The morphological changes of bacteria were also observed through SEM using *Staph.* $20 \mu\text{L}$ diluted inoculum of *Staph.* at the concentration of 10^7 CFU/mL were spread on the PLLA and Ag/PLLA membranes, respectively, before being incubated at 37°C for 2 hours. SEM observations were then performed.

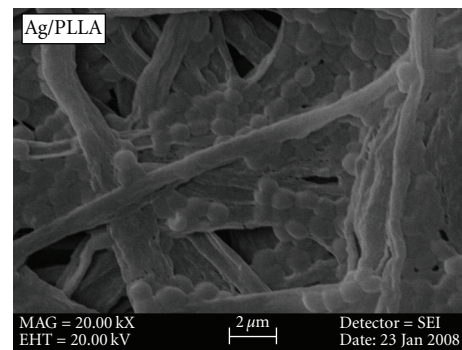
As shown in Figure 4, the number of *Staph.* spread on PLLA membrane was obviously more than that on Ag/PLLA membrane. Besides, the surface of *Staph.* on PLLA membrane was smoother than that on Ag/PLLA membrane. This result indicated that there might be less destroy on the structure of bacteria which spread on PLLA membrane than that on Ag/PLLA membrane.

4. Discussion

Tissue engineering scaffolds with the effectiveness in reducing the possibility of infections will be more acceptable for medical applications [13]. For example, skin is the first protective barrier for all the tissues and organs, so a wound on skin will easily weaken the anti-infective capability of human body. Here we mainly focused on the feasibility to fabricate an antibacterial scaffolds for wound healing.



(a)



(b)

FIGURE 4: SEM images magnified *Staph.* on PLLA and Ag/PLLA fibrous membrane 20 thousand times (20 kV). (1) The number of *Staph.* on PLLA membranes was more than that on the Ag/PLLA membrane. (2) *Staph.* on PLLA membrane had smooth surface, while the ones on Ag/PLLA membrane were not very smooth.

Nanosilver was observed to be toxic to bacteria cells. This finding suggested an exploration of the antibacterial tissue engineering scaffolds [12, 13, 24]. In 2004, Alt et al. reported that bone cement with 1% of nanosilver showed high antibacterial activity against most of the tested bacteria [13]. Yeo et al. found that fibers having nanosilver showed excellent antibacterial property. Besides, PLLA was already approved by FDA as a safe material for the clinical application. Thus, to combine silver nanoparticles and PLLA by using electrospinning technique [1–4] could be a good approach to produce tissue engineering scaffolds with high antibacterial effect. On the other hand, electrospun fibers can produce ventilate fibrous membranes with wide interface to highly perform their antibacterial activity.

In the antibacterial tests, PLLA membranes were set as control specimen. The Ag/PLLA membranes were found to inhibit the proliferation of *E. coli* and *Staphylococcus* significantly. On the basis of this finding, silver nanoparticles were approved to be released from PLLA fibers gradually. In terms of the degradability of PLLA, Ag/PLLA is an optimal matrix to contain silver nanoparticles and help to gradually release silver nanoparticles as PLLA degrade. Accordingly, Ag/PLLA fibrous membrane is a good candidate antibacterial substance for tissue engineering.

TABLE 1: Assessment of the antibacterial activity of the extractions of Ag/PLLA membranes.

| Bacteria | Average width of bacteria inhibition clear zone (mm) | |
|------------------------------|--|------------|
| | PLLA | 5% Ag/PLLA |
| Before | | |
| <i>Escherichia coli</i> | 0 | 5.0 ± 0.1* |
| <i>Staphylococcus aureus</i> | 0 | 5.0 ± 0.1* |
| After | | |
| <i>Escherichia coli</i> | 0 | 1.2 ± 0.1* |
| <i>Staphylococcus aureus</i> | 0 | 1.5 ± 0.1* |

* The mean values were shown for means ± SD. $P < .05$ versus PLLA membranes.

Meanwhile, although the Ag/PLLA membrane was proved to be antibacterial in this study, the antibacterial activity of the membrane was observed decreasing. After eight-week exposure in the air, the antibacterial activity of the Ag/PLLA fibrous membranes reduced. This result may be caused by the oxidization by the air or other reactions during the exposure. So, further investigation about the factors which affect the antibacterial properties of Ag/PLLA membrane need to be performed in the next process. These findings also suggest that it is possible to keep Ag/PLLA membrane with strong antibacterial activity for long time.

To investigate the mechanism of the antibacterial activity of Ag/PLLA membranes, morphological change of bacteria were primarily observed by SEM. More Staph. were seen on PLLA membrane than that on Ag/PLLA membrane. And the surface of Staph. on PLLA membranes was smoother than that on Ag/PLLA membranes. These findings imply that nanosilver may affect the structure of bacterial membrane, thereby cause the defunctionalization of bacteria. The mechanism of antibacterial activity of Ag/PLLA membranes needs further study to be verified.

On the other hand, based on the review of silver toxicity studies, it was reported that the possible side effects of nanoparticles had not been much investigated, so, detailed study needs to be carried out before the merchandised product is introduced to the market [30]. But, as a strong antibacterial substance, silver nanoparticles have been playing an irreplaceable role in anti-infections. Hence, the further study needs to be carried on for both the antibacterial function and toxicity of silver nanoparticles composed materials to find out the safe balance point for antibacterial scaffolds with no toxicity to the human body and environment.

5. Conclusions

This study describes the antibacterial capability of the Ag/PLLA fibrous membrane. On the basis of the observations and findings above, it can be concluded that PLLA is a good matrix for containing and gradually releasing antibacterial substance, while silver nanoparticles can provide strong antibacterial property to the Ag/PLLA fibrous membranes. Thus, Ag/PLLA fibrous membrane can be used as an antibacterial scaffold for wound healing. Besides, the factors which

influence the antibacterial effect need further investigation to clarify the mechanism of antibacterial activity of Ag/PLLA membranes.

Acknowledgments

The authors would like to express their gratitude to the Hong Kong Research Grant Council, the Technology Innovation Commission/HKRITA, and the Hong Kong Polytechnic University for supporting this research through Projects PolyU 5281/03E, ITP-001-07-TP, and G-YE51.

References

- [1] S. Sukigara, M. Gandhi, J. Ayutsede, M. Micklus, and F. Ko, "Regeneration of Bombyx mori silk by electrospinning—part 1: processing parameters and geometric properties," *Polymer*, vol. 44, no. 19, pp. 5721–5727, 2003.
- [2] Y. Chen, A. F. T. Mak, M. Wang, J. Li, and M. S. Wong, "PLLA scaffolds with biomimetic apatite coating and biomimetic apatite/collagen composite coating to enhance osteoblast-like cells attachment and activity," *Surface and Coatings Technology*, vol. 201, no. 3-4, pp. 575–580, 2006.
- [3] K. E. Park, H. K. Kang, S. J. Lee, B. M. Min, and W. H. Park, "Biomimetic nanofibrous scaffolds: preparation and characterization of PGA/Chitin blend nanofibers," *Biomacromolecules*, vol. 7, no. 2, pp. 635–643, 2006.
- [4] S. Sukigara, M. Gandhi, J. Ayutsede, M. Micklus, and F. Ko, "Regeneration of Bombyx mori silk by electrospinning—part 2: process optimization and empirical modeling using response surface methodology," *Polymer*, vol. 45, no. 11, pp. 3701–3708, 2004.
- [5] S. Putthananat, R. K. Eby, W. Kataphinan, et al., "Electrospun Bombyx mori gland silk," *Polymer*, vol. 47, no. 15, pp. 5630–5632, 2006.
- [6] H. K. Noh, S. W. Lee, J.-M. Kim, et al., "Electrospinning of chitin nanofibers: degradation behavior and cellular response to normal human keratinocytes and fibroblasts," *Biomaterials*, vol. 27, no. 21, pp. 3934–3944, 2006.
- [7] K. Tomihata and Y. Ikada, "In vitro and in vivo degradation of films of chitin and its deacetylated derivatives," *Biomaterials*, vol. 18, no. 7, pp. 567–575, 1997.
- [8] W.-J. Li, C. T. Laurencin, E. J. Caterson, R. S. Tuan, and F. K. Ko, "Electrospun nanofibrous structure: a novel scaffold for tissue engineering," *Journal of Biomedical Materials Research*, vol. 60, no. 4, pp. 613–621, 2002.

- [9] W.-J. Li, R. Tuli, X. Huang, P. Laquerriere, and R. S. Tuan, "Multilineage differentiation of human mesenchymal stem cells in a three-dimensional nanofibrous scaffold," *Biomaterials*, vol. 26, no. 25, pp. 5158–5166, 2005.
- [10] Y. Ji, K. Ghosh, X. Z. Shu, et al., "Electrospun three-dimensional hyaluronic acid nanofibrous scaffolds," *Biomaterials*, vol. 27, no. 20, pp. 3782–3792, 2006.
- [11] D. H. Reneker and I. Chun, "Nanometre diameter fibres of polymer, produced by electrospinning," *Nanotechnology*, vol. 7, no. 3, pp. 216–223, 1996.
- [12] M. Li, M. J. Mondrinos, M. R. Gandhi, F. K. Ko, A. S. Weiss, and P. I. Lelkes, "Electrospun protein fibers as matrices for tissue engineering," *Biomaterials*, vol. 26, no. 30, pp. 5999–6008, 2005.
- [13] V. J. Chen and P. X. Ma, "The effect of surface area on the degradation rate of nano-fibrous poly(L-lactic acid) foams," *Biomaterials*, vol. 27, no. 20, pp. 3708–3715, 2006.
- [14] X. Chen and H. J. Schluesener, "Nanosilver: a nanoparticle in medical application," *Toxicology Letters*, vol. 176, no. 1, pp. 1–12, 2008.
- [15] V. Alt, T. Bechert, P. Steinrücke, et al., "An in vitro assessment of the antibacterial properties and cytotoxicity of nanoparticulate silver bone cement," *Biomaterials*, vol. 25, no. 18, pp. 4383–4391, 2004.
- [16] B. Shan, Y.-Z. Cai, J. D. Brooks, and H. Corke, "Antibacterial properties of *Polygonum cuspidatum* roots and their major bioactive constituents," *Food Chemistry*, vol. 109, no. 3, pp. 530–537, 2008.
- [17] Y. Li, P. Leung, L. Yao, Q. W. Song, and E. Newton, "Antimicrobial effect of surgical masks coated with nanoparticles," *Journal of Hospital Infection*, vol. 62, no. 1, pp. 58–63, 2006.
- [18] T. A. Gaonkar, L. A. Sampath, and S. M. Modak, "Evaluation of the antimicrobial efficacy of urinary catheters impregnated with antiseptics in an in vitro urinary tract model," *Infection Control and Hospital Epidemiology*, vol. 24, no. 7, pp. 506–513, 2003.
- [19] B. Walder, D. Pittet, and M. R. Tramèr, "Prevention of bloodstream infections with central venous catheters treated with anti-infective agents depends on catheter type and insertion time: evidence from a meta-analysis," *Infection Control & Hospital Epidemiology*, vol. 23, no. 12, pp. 748–756, 2002.
- [20] N. S. Morris and D. J. Stickler, "Encrustation of indwelling urethral catheters by *Proteus mirabilis* biofilms growing in human urine," *Journal of Hospital Infection*, vol. 39, no. 3, pp. 227–234, 1998.
- [21] B. Galeano, E. Korff, and W. L. Nicholson, "Inactivation of vegetative cells, but not spores, of *Bacillus anthracis*, *B. cereus*, and *B. subtilis* on stainless steel surfaces coated with an antimicrobial silver- and zinc-containing zeolite formulation," *Applied and Environmental Microbiology*, vol. 69, no. 7, pp. 4329–4331, 2003.
- [22] V. Thomas, M. M. Yallapu, B. Sreedhar, and S. K. Bajpai, "A versatile strategy to fabricate hydrogel-silver nanocomposites and investigation of their antimicrobial activity," *Journal of Colloid and Interface Science*, vol. 315, no. 1, pp. 389–395, 2007.
- [23] K. K. Lai and S. A. Fontecchio, "Use of silver-hydrogel urinary catheters on the incidence of catheter-associated urinary tract infections in hospitalized patients," *American Journal of Infection Control*, vol. 30, no. 4, pp. 221–225, 2002.
- [24] J. H. Crabtree, R. J. Burchette, R. A. Siddiqi, I. T. Huen, L. L. Hadnott, and A. Fishman, "The efficacy of silver-ion implanted catheters in reducing peritoneal dialysis-related infections," *Peritoneal Dialysis International*, vol. 23, no. 4, pp. 368–374, 2003.
- [25] D. K. Riley, D. C. Classen, L. E. Stevens, and J. P. Burke, "A large randomized clinical trial of a silver-impregnated urinary catheter: lack of efficacy and staphylococcal superinfection," *The American Journal of Medicine*, vol. 98, no. 4, pp. 349–356, 1995.
- [26] F. Furno, K. S. Morley, B. Wong, et al., "Silver nanoparticles and polymeric medical devices: a new approach to prevention of infection?" *Journal of Antimicrobial Chemotherapy*, vol. 54, no. 6, pp. 1019–1024, 2004.
- [27] M. Wilson, R. McNab, and B. Henderson, *Bacterial Disease Mechanisms: An Introduction to Cellular Microbiology*, Cambridge University Press, Cambridge, UK, 2002.
- [28] S. Y. Yeo, H. J. Lee, and S. H. Jeong, "Preparation of nanocomposite fibers for permanent antibacterial effect," *Journal of Materials Science*, vol. 38, no. 10, pp. 2143–2147, 2003.
- [29] J. Li, Y. Li, L. Li, A. F. T. Mak, F. Ko, and L. Qin, "Fabrication of poly(L-lactic acid) scaffolds with wool keratin for osteoblast cultivation," *Advanced Materials Research*, vol. 47–50, pp. 845–848, 2008.
- [30] M. Rai, A. Yadav, and A. Gade, "Silver nanoparticles as a new generation of antimicrobials," *Biotechnology Advances*, vol. 27, no. 1, pp. 76–83, 2009.

Research Article

Fracture Toughness of Vapor Grown Carbon Nanofiber-Reinforced Polyethylene Composites

A. R. Adhikari,¹ E. Partida,¹ T. W. Petty,¹ R. Jones,¹ K. Lozano,¹ and C. Guerrero²

¹Department of Mechanical Engineering, University of Texas-Pan American, Edinburg, TX 78539, USA

²Facultad de Ingeniería Mecánica y Eléctrica, Universidad Autónoma de Nuevo León, San Nicolás de los Garza, 66451, Nuevo León, CP, Mexico

Correspondence should be addressed to K. Lozano, lozanok@utpa.edu

Received 2 November 2008; Accepted 22 June 2009

Recommended by Alan K. T. Lau

The impact fracture behavior of a vapor grown carbon nanofiber (VGCNF) reinforced high-density polyethylene (PE) composite was evaluated. The samples consisting of pure PE and composites with 10 wt% and 20 wt% of VGCNFs were prepared by a combination of hot-pressing and extrusion methods. Extrusion was used to produce samples with substantially different shear histories. The fracture behavior of these samples was analyzed using the essential work of fracture (EWF) approach. The results showed an increase of 292% in the essential work of fracture for the loading of 10 wt%. Further increasing fiber loading to 20 wt% caused the essential work of fracture to increase only 193% with respect to the unmodified material. Evaluation of the fracture surface morphology indicated that the fibril frequency and microvoid size within the various fiber loadings depended strongly on processing conditions.

Copyright © 2009 A. R. Adhikari et al. This is an open access article distributed under the Creative Commons Attribution License, which permits unrestricted use, distribution, and reproduction in any medium, provided the original work is properly cited.

1. Introduction

Polyethylene is characterized by a great capacity to absorb energy despite its low modulus of elasticity [1]. Because of its high toughness it offers promise as a matrix for highly damage tolerant composites. However development of adequate adhesion between PE and high performance reinforcements has been a challenge. Nanofibers show great promise for modification of existing materials due to the combination of their small size and surface compatibility. Their high thermal, electrical, and mechanical properties offer the prospect of substantial improvements in polymeric systems. This prospect is further enhanced by the strong natural adhesion nanofibers with many thermoplastic matrices [2–6].

Prior studies have shown that VGCNFs interact strongly with polymeric matrices and enhance several properties. PE/VGCNF composites have been found to produce a simultaneous increase in both storage (elastic) and loss (viscous dissipation) modulus as measured by dynamic mechanical analysis [7]. Tensile tests of these composites show a remarkable increase in elongation to failure with

increased shear history and an apparently new mechanism of void stabilization permitting the formation of widespread stable subcritical voids in the deformed polymer [8]. The current work extends the study of these materials to the regime of dynamic impact behavior.

The highly nonlinear nature of the fracture process in PE requires the use of nonlinear fracture analysis. The most widely used methods are the J-integral [9] and the essential work of fracture (EMF) [10, 11]. In the recent years, the concept of EWF has been broadly applied to the evaluation of fracture toughness in ductile polymers and their composites due to its greater simplicity when compared to J-integral measurement [12–15]. This theory was initially proposed by Broberg [16] in 1968 and further developed by Mai and others [11, 17]. The theory poses that the total energy necessary to fracture a cracked material (W_f) contains two components the essential work of fracture (W_e) and nonessential work or plastic work (W_p) (see Figure 1)

$$W_f = W_e + W_p. \quad (1)$$

W_e is the essential work required to rupture in its inner fracture process zone. For a given material thickness (t), W_e

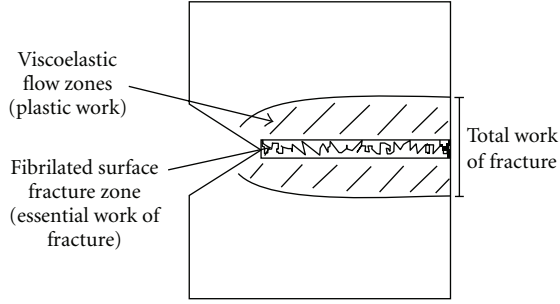


FIGURE 1: Schematic diagram of flow zones during fracture.

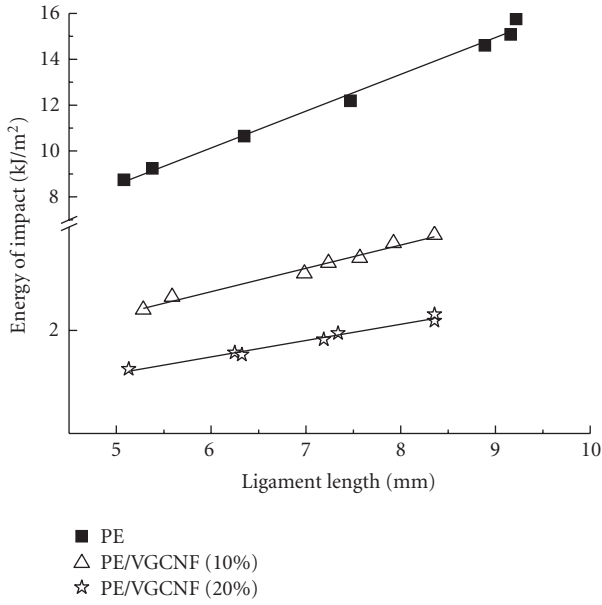


FIGURE 2: A representative plot of energy of impact (w_f) versus ligament length (ℓ).

is proportional to the ligament length (ℓ). W_p is the energy consumed by mechanisms of deformation in the outer plastic zone and is a volume energy proportional to ℓ^2 .

The expression in (1) can be expanded to

$$W_f = w_e \ell t + \beta w_p \ell^2 t. \quad (2)$$

In terms of specific values, total specific work of fracture, w_f is given by

$$w_f = \left(\frac{W_f}{\ell t} \right) = w_e + \beta w_p \ell, \quad (3)$$

where w_e and w_p are the essential specific work of fracture and the specific nonessential work (or specific plastic work), respectively. The term β is a form factor for the plastic zone. Equation (3) provides the w_e and w_p from the intercept and the slope of corresponding linear regression curve of the plot of w_f as a function of ℓ . A representative plot of w_f as a function of ℓ is shown in Figure 2.

In this study, measurements of energy to fracture under impact using the method of essential work of fracture were made. Fracture surface morphology was also evaluated to determine changes in the fracture mechanism caused by nanofibers reinforcement.

2. Experimental

2.1. Materials. The systems evaluated were based on high-density polyethylene (Marflex PE CL-L-R-240370) provided by Chevron-Philips Chemical Co. and vapor grown carbon nanofibers (Pyrograf III) (VGCNFs) provided by Applied Sciences. The fibers were purified before use according to procedures developed and described elsewhere [18]. Purification of the fibers was done with a process of refluxing nanofibers in dichloromethane followed by rinsing with deionized water. The purpose of purification is to remove amorphous carbon and untangle nested fiber bundles. It also serves to lightly functionalize the surface of the fibers, making them more compatible with some polymer matrices though this may not be critical to performance in PE.

2.2. Processing. After purification, the fibers were introduced into the PE matrix using a Haake Polylab 600 mixer which subjects the composite to high shear stresses. Mixing was done at a nominal temperature of 190 °C for a total of 16 minutes at varied mixing speeds. A 2-minute mix of pure PE at 90 rpm was followed by fiber addition, 11 minutes at 30 rpm, and 3 minutes at 60 rpm. The length of each processing step was determined by the time necessary to produce a constant shearing torque measured at the mix head. The resulting material was hot pressed (Carver Hot-Press model 3912) and again extruded using a Haake Rheomixer 600 with an extrusion screw speed of 40 rpm and a die temperature of 190 °C.

After extrusion, the film was stretched by a Haake Tape Postex 600 to create a tape. To introduce varying shear stress histories generated by the extensional flow, drawing was done at 10 and 20 rpm. The resulting tape was pelletized once more and then molded to the final specimen size and thickness in a hydraulic heated press (PHI model 100-1a). The preparation combinations are summarized in Table 1. Rectangular 63.5 mm × 12.7 mm × 3.2 mm bars, with a single-edge-notched 3-point bending configuration, were used for impact testing.

2.3. Characterizations. Tests were done at a temperature of 22 °C in the Dynatup 830I drop weight system with a span length of 50 mm and an impact velocity of 2.5 m/s. Eight specimens were prepared and tested for each treatment combination. The exact length of the ligament was measured by optical microscopy on an Olympus T4560 imaging analyzer. The specimen was made with a saw 1mm gap and the tip of crack with a fresh razor blade. It was not necessary to immerse in liquid nitrogen because this sample presented a brittle fracture. The fracture morphology was studied using Scanning electron microscopy (SEM).

TABLE 1: Process flow used for neat PE and PE/VGCNF composites preparation, MP samples were mixed and pressed; MPEP 10 RPM samples were mixed, pressed, extruded at 10 rpm and pressed again; MPEP 20 RPM samples were mixed pressed extruded at 20 rpm and pressed again.

| Sample | Mixed | Hot pressed | Process type | | Mold pressed |
|-------------------|-------|-------------|---------------------------------------|----|--------------|
| | | | Extruded velocity of elongation (rpm) | | |
| | | | 10 | 20 | |
| Pure PE | | | | | |
| MP | × | × | – | – | × |
| MPEP 10 RPM | × | × | × | – | × |
| MPEP 20 RPM | × | × | – | × | × |
| PE/VGCNF (10% wt) | | | | | |
| MP | × | × | – | – | × |
| MPEP 10 RPM | × | × | × | – | × |
| MPEP 20 RPM | × | × | – | × | × |
| PE/VGCNF (20% wt) | | | | | |
| MP | × | × | – | – | × |
| MPEP 10 RPM | × | × | × | – | × |
| MPEP 20 RPM | × | × | – | × | × |

3. Results and Discussion

3.1. Fracture Analysis. Impact results of PE and its composites were compared using single-edge notched tension specimen. A representative plot of total energy of fracture versus ligament length is shown in Figure 2. It clearly shows the effect of increased flow stress with nanofiber addition. The higher flow stress results in increased constraint in the ligament and a reduction in gross viscoplastic flow in the ligament. The reduced gross plasticity reduces the total energy of fracture relative to the unreinforced material. Table 2 summarizes the values of w_e , w_p and total energy. w_e values for all samples are plotted in Figure 3. The unmodified PE shows an increase in w_e (local fracture energy) but an overall reduction in fracture energy. The fiber modified systems show a clear increase in w_e with increasing shear history while total fracture energy falls relative to the unmodified system. In other words, increased processing improves the local material toughness in the process zone while fiber addition reduces the overall toughness by constraining gross plasticity in the specimen.

The increase in toughness is higher for the 10 wt% PE/VGCNF composite than for the 20 wt% fiber system which could indicate a countervailing effect of fiber loading. Essential work of fracture in the fracture zone corresponds to the energy required to debond PE and VGCNF, and to deform the polymer matrix [19]. Therefore, the likely mechanism for the improvement in toughness is improvement in fiber/polymer adhesion and better dispersion of the fibers. These improvements result in greater void growth through stable fibril formation (see morphology section). At the same time, the plastic work, w_p , generally falls, suggesting greater localization of the fracture process and reduction of gross plasticity. The smaller increase in toughness observed in the

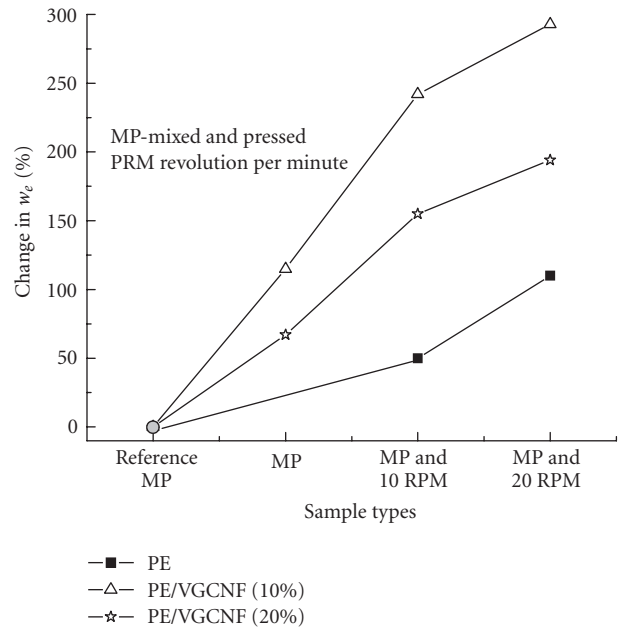


FIGURE 3: Comparison of % change of w_e with process parameters.

higher fiber loaded system indicates that the toughening phenomenon is primarily matrix driven and is not due directly to fiber breakage or other fiber driven energy consuming process. Eventually the higher loading of fibers (20 wt%) results in a reduction in the work of fracture through restriction of ductile matrix deformation (caused by constraint as well as a reduction in the volume of polymer available). This leads to a diminution in the specific plastic work of the material. This is similar to the behavior seen in traditional short-glass fiber reinforced polymers [20, 21].

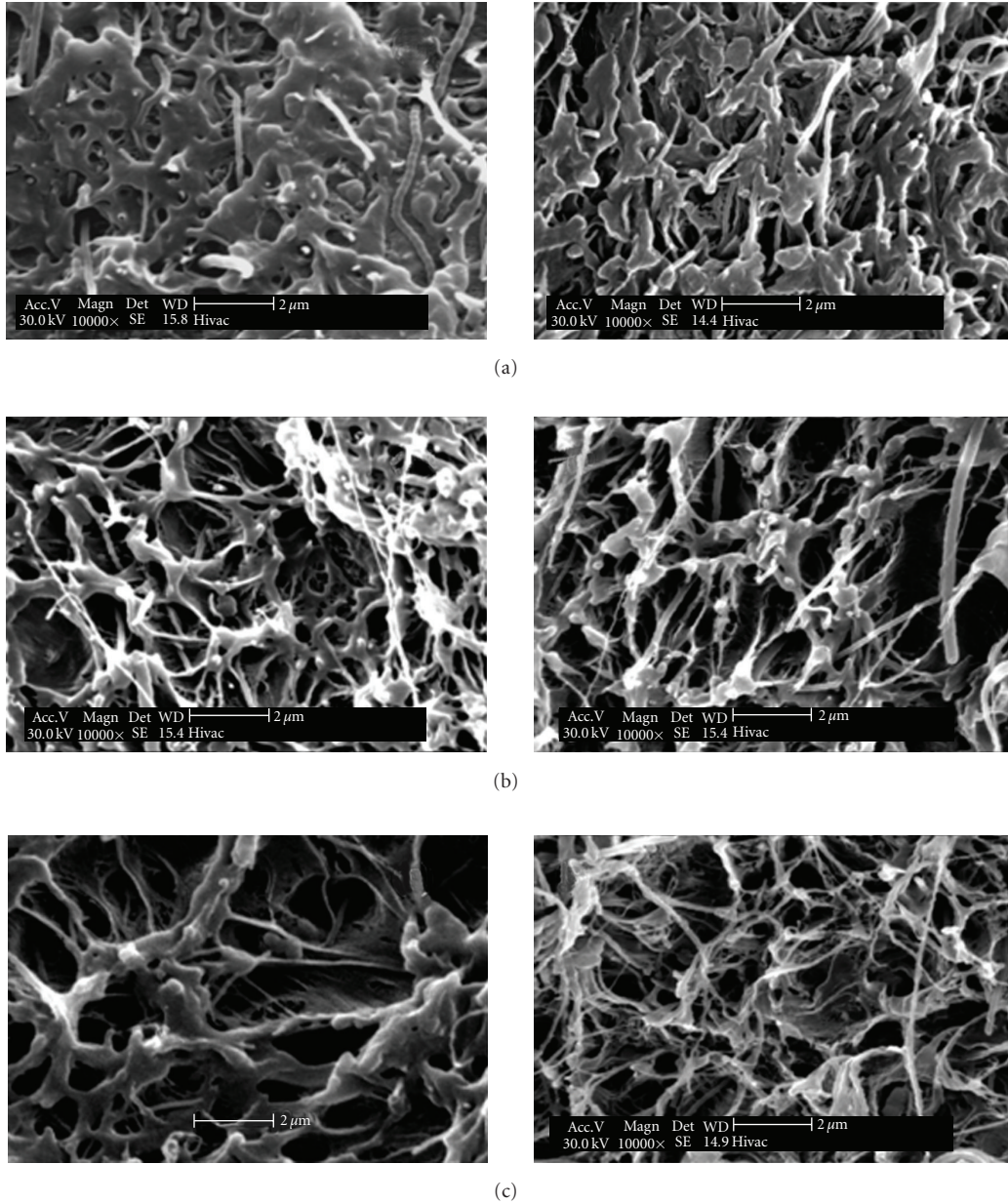


FIGURE 4: Fracture surface SEM micrograph of 10% (left) and 20% (right) PE/VGCF Composite: (a) undrawn, (b) 10 rpm drawn, and (c) 20 rpm drawn.

The substantial improvement seen in process zone energy dissipation with the addition of nanofibers in an impact environment suggests that these materials should show substantial improvement in resistance to slow stable crack growth or stress corrosion cracking which are quasistatic fracture processes which do not involve significant gross plasticity. That will be the subject of future research.

3.2. Morphology. Changes in the fracture process are usually reflected in the morphology of the fracture surface; therefore, specimens were evaluated using the scanning electron micro-

scope. It should be noted that the high level of fibrillation seen in these impact test specimens, especially the levels seen in the drawn materials, are more consistent with quasistatic fracture in neat polyethylene systems than with impact. Nanofiber loading makes possible energy dissipating fracture processes normally prevented by high crack velocities.

Representative micrographs are shown in Figure 4 for PE/VGCF composites with fiber contents of 10 and 20 wt% and three processing levels. The fibers were clearly well dispersed in both systems. The number and length of fibrils, along with voids developed within the fracture process zone, increase dramatically after the shearing process (10 rpm and

TABLE 2: EWF parameters for neat PE and PE/VGCNF composites.

| Samples | w_e (kJ/m ²) | βw_p (kJ/m ²) | Ligament (mm) | r^2 | Total energy (kJ/m ²) |
|---------------------|-------------------------------|-------------------------------------|------------------|-------|--------------------------------------|
| PE | | | | | |
| MP | 0.4978 | 1.606 | 8.890 | 0.993 | 2.0799 |
| MPEP at 10 RPM | 0.7058 | 1.2122 | 9.017 | 0.995 | 1.918 |
| MPEP at 20 RPM | 0.9914 | 1.1704 | 8.128 | 0.991 | 1.8828 |
| PE/VGCNFs (10% wt.) | | | | | |
| MP | 1.0156 | 0.2262 | 7.925 | 0.984 | 1.2418 |
| MPEP at 10 RPM | 1.6165 | 0.1216 | 8.255 | 0.980 | 1.7381 |
| MPEP at 20 RPM | 1.8531 | 0.1471 | 8.001 | 0.992 | 2.0002 |
| PE/VGCNFs (20% wt.) | | | | | |
| MP | 0.7891 | 0.1588 | 8.357 | 0.980 | 0.9479 |
| MPEP at 10 RPM | 1.2015 | 0.0446 | 8.966 | 0.915 | 1.2461 |
| MPEP at 20 RPM | 1.3861 | 0.1012 | 8.636 | 0.977 | 1.4873 |

20 rpm) for 10 wt% fibers loading. However, the development of fibrils in 20 wt% composite at higher shearing (20 rpm) is not similar to that of 10 wt% composites. This can be attributed to the interaction between the nanofibers at higher loading. The observed fracture surface morphology indicates that the higher values of local fracture energy, w_e , of composites is a result of enhancement in fibrillation and the formation of large stable voids resulting from coalescence of stable voids. The fibers act to stabilize and increase fibrillation thus enhancing the toughness of the matrix in the local process zone.

4. Conclusion

The addition of carbon nanofibers to polyethylene improves the ability of the polymer to form large fibril/void structures even under conditions of process zone constraint due to impact loading. This is reflected in an increase in local fracture toughness measured by the essential work of fracture. Further, this local toughness increases with increasing shear history during processing. The strength of this interaction may arise from one or both of two sources. The extended shear and thermal history may cause molecular scission as evidenced by the reduced total toughness of the unmodified system. The resulting free radicals then may bond to the nanofibers, resulting in an extremely strong matrix/fiber interaction. It is also likely that because of their similar structures, polyethylene and VGCNFs will form strong bonds when polymer chains are stretched out along the fiber surfaces. Either mechanism results in a level of interaction which produces properties and fracture processes not heretofore observed in polymer composites.

Acknowledgment

The authors would like to acknowledge Jiang Zhu at Rice University for SEM pictures.

References

- [1] C. A. Harper and E. M. Petrie, Eds., *Plastics Materials and Processes: A Concise Encyclopedia*, John Wiley & Sons, New York, NY, USA, 2003.
- [2] G. Galgali, C. Ramesh, and A. Lele, "A rheological study on the kinetics of hybrid formation in polypropylene nanocomposites," *Macromolecules*, vol. 34, no. 4, pp. 852–858, 2001.
- [3] F. H. Gojny and K. Schulte, "Functionalisation effect on the thermo-mechanical behaviour of multi-wall carbon nanotube/epoxy-composites," *Composites Science and Technology*, vol. 64, no. 15, pp. 2303–2308, 2004.
- [4] W. E. Gacitua, A. A. Ballerini, and J. Zhang, "Polymer nanocomposites: synthesis and natural fillers a review," *Maderas. Ciencia y Tecnología*, vol. 7, pp. 159–178, 2005.
- [5] L. Bokobza and J.-P. Chauvin, "Reinforcement of natural rubber: use of in situ generated silicas and nanofibres of sepiolite," *Polymer*, vol. 46, no. 12, pp. 4144–4151, 2005.
- [6] B. Lim, C.-J. Kim, B. Kim, et al., "The effects of interfacial bonding on mechanical properties of single-walled carbon nanotube reinforced copper matrix nanocomposites," *Nanotechnology*, vol. 17, no. 23, pp. 5759–5764, 2006.
- [7] S. Yang, J. Taha-Tijerina, V. Serrato-Diaz, K. Hernandez, and K. Lozano, "Dynamic mechanical and thermal analysis of aligned vapor grown carbon nanofiber reinforced polyethylene," *Composites Part B*, vol. 38, no. 2, pp. 228–235, 2007.
- [8] K. Lozano, S. Yang, and R. E. Jones, "Nanofiber toughened polyethylene composites," *Carbon*, vol. 42, no. 11, pp. 2329–2331, 2004.
- [9] J. G. Williams, *Fracture Mechanics of Polymers*, Ellis Horwood, Chichester, UK, 1987.
- [10] K. B. Broberg, "Crack-growth criteria and non-linear fracture mechanics," *Journal of the Mechanics and Physics of Solids*, vol. 19, no. 6, pp. 407–418, 1971.
- [11] Y.-W. Mai and B. Cotterell, "On the essential work of ductile fracture in polymers," *International Journal of Fracture*, vol. 32, no. 2, pp. 105–125, 1986.
- [12] R. Lach, K. Schneider, R. Weidisch, A. Janke, and K. Knoll, "Application of the essential work of fracture concept to nanostructured polymer materials," *European Polymer Journal*, vol. 41, no. 2, pp. 383–392, 2005.

- [13] D. Arencón, J. I. Velasco, V. Realinho, M. Antunes, and M. L. I. MasPOCH, "Essential work of fracture analysis of glass microsphere-filled polypropylene and polypropylene/poly(ethylene terephthalate-co-isophthalate) blend-matrix composites," *Polymer Testing*, vol. 26, no. 6, pp. 761–769, 2007.
- [14] X. L. Wang, R. K. Y. Li, Y. X. Cao, and Y. Z. Meng, "Essential work of fracture analysis for starch filled poly(propylene carbonate) composites," *Materials and Design*, vol. 28, no. 6, pp. 1934–1939, 2007.
- [15] R. E. Jones and W. L. Bradley, "Fracture toughness testing of Polyethylene pipe materials," in *ASTM STP 995*, vol. 1, pp. 447–456, 1989.
- [16] K. B. Broberg, "On stable crack growth," *Journal of the Mechanics and Physics of Solids*, vol. 23, no. 3, pp. 215–237, 1975.
- [17] Y. W. Mai and K. M. Pilko, "The essential work of plane stress ductile fracture of a strain-aged steel," *Journal of Materials Science*, vol. 14, no. 2, pp. 386–394, 1979.
- [18] K. Lozano, B. Files, F. Rodrigues-Macias, and E. V. Barrera, "Purification and functionalization of vapor grown carbon fibers and single wall nanotubes," in *Proceedings of the TMS Fall Meeting Symposium Powder Materials: Current Research and Industrial Practices*, pp. 333–340, Cincinnati, Ohio, USA, 1999.
- [19] J. Karger-Kocsis, *Polypropylene: Structure, Blends and Composites*, Vol. 3, Chapman & Hall, London, UK, 1995.
- [20] E. C. Y. Ching, R. K. Y. Li, S. C. Tjong, and Y.-W. Mai, "Essential work of fracture (EWF) analysis for short glass fiber reinforced and rubber toughened nylon-6," *Polymer Engineering and Science*, vol. 43, no. 3, pp. 558–569, 2003.
- [21] S. C. Tjong, S. A. Xu, and Y. W. Mai, "Impact fracture toughness of short glass fiber-reinforced polyamide 6,6 hybrid composites containing elastomer particles using essential work of fracture concept," *Materials Science and Engineering A*, vol. 347, no. 1-2, pp. 338–345, 2003.

Research Article

Processing and Structure of Carbon Nanofiber Paper

Zhongfu Zhao,¹ Jihua Gou,¹ and Aurangzeb Khan²

¹Department of Mechanical, Materials and Aerospace Engineering, University of Central Florida, Orlando, FL 32816, USA

²Department of Electrical and Computer Engineering, University of South Alabama, Mobile, AL 36688, USA

Correspondence should be addressed to Jihua Gou, jgou@mail.ucf.edu

Received 3 November 2008; Accepted 24 February 2009

Recommended by Alan K. T. Lau

A unique concept of making nanocomposites from carbon nanofiber paper was explored in this study. The essential element of this method was to design and manufacture carbon nanofiber paper with well-controlled and optimized network structure of carbon nanofibers. In this study, carbon nanofiber paper was prepared under various processing conditions, including different types of carbon nanofibers, solvents, dispersants, and acid treatment. The morphologies of carbon nanofibers within the nanofiber paper were characterized with scanning electron microscopy (SEM). In addition, the bulk densities of carbon nanofiber papers were measured. It was found that the densities and network structures of carbon nanofiber paper correlated to the dispersion quality of carbon nanofibers within the paper, which was significantly affected by papermaking process conditions.

Copyright © 2009 Zhongfu Zhao et al. This is an open access article distributed under the Creative Commons Attribution License, which permits unrestricted use, distribution, and reproduction in any medium, provided the original work is properly cited.

1. Introduction

A variety of nanoparticles have been incorporated into polymer resins to make nanocomposites for a wide range of applications [1, 2]. Among them, carbon nanotubes and carbon nanofibers have attracted significant research interests due to their unique characteristics and properties such as high strength and modulus, low density, high surface area, good chemical stability, high electrical and thermal conductivity, and fire resistance. Although there are different processing techniques to fabricate polymer nanocomposites, they are mainly divided into three categories: (a) solution processing [3–13], (b) melt mixing [14–17] using a batch mixer or continuous device such as an extruder, and (c) in situ polymerization [18, 19]. The mechanical and physical properties of polymer nanocomposites have large variations due to processing-related issues.

Generally, carbon nanotubes and carbon nanofibers consist of graphitic cylinders with diameters of 1–100 nm and high aspect ratios of a few micro lengths, leading to high van der Waals force between adjacent nanotubes or nanofibers. The high van der Waals forces and high aspect ratios with a combination of high flexibilities make the nanotubes and nanofibers easily aggregate. As a result, it is difficult to individually disperse the nanotubes or the nanofibers into polymer resins. The addition of a small amount of carbon

nanofibers will also significantly increase the viscosity of the resin. Particularly during the processing of fiber-reinforced polymer composites, the resin flow through the fiber mats becomes very difficult. The fiber mats will also filter out the nanotubes and nanofibers during liquid molding process such as resin transfer molding and vacuum-assisted resin transfer molding [20, 21]. In addition, the presence of the nanotubes or nanofibers can significantly modify the local crystallization behavior of polymer resins either through the direct polymer/particle interaction at the interface or the modification of temperature and stress field around and between the nanotubes or nanofibers.

A unique concept of making nanocomposites from carbon nanofiber paper has been explored [22–24]. This approach involves making carbon nanofiber paper through the filtration of the suspension of well-dispersed carbon nanofibers under controlled process conditions. Such a specialty paper has a uniform network structure formed through the entanglement of the nanofibers. The carbon nanofiber paper can be further integrated into traditional fiber reinforced composite laminates through liquid molding processes. The structural characteristics of carbon nanofiber paper such as pore size and orientation can significantly affect the penetration of polymer resins. In this study, the correlation between the morphologies and processing conditions of the paper was systematically studied. Specifically,

the effects of different types of carbon nanofiber, solvent, dispersant, and acid treatment on the microstructures of carbon nanofiber paper were examined. The processing conditions were chosen to make carbon nanofiber paper with an optimum structure.

2. Experimental

Vapor-grown carbon nanofiber was supplied from Applied Sciences, Inc., Cedarville, Ohio, USA. Two types of carbon nanofibers were used: oxidized carbon nanofiber (OXCNF) and nonoxidized carbon nanofiber (NOXCNF). Compared to NOXCNF, OXCNF had more functional groups, such as hydroxyl group ($-OH$) and carboxylic acid ($-COOH$). The OXCNF and NOXCNF were rinsed with diluted nitric acid. The acid-treated carbon nanofibers were designated as RIN-OXCNF and RIN-NOXCNF. During the rinse of carbon nanofibers, OXCNF or NOXCNF was first stirred in 2M nitric acid at room temperature for 2 hours. The solution was then filtered through a 4 μm polycarbonate membrane and rinsed with water until the nitric acid was completely removed. In this study, deionized water (WA), ethyl alcohol (AL), and acetone (AC) were used as solvents. The dispersant (DISPERBYK-191; BYK-Chemie, Wesel, Germany) was used to aid the dispersion of carbon nanofibers. The BYK had amine values of 20 mg KOH/g and acid value of 30 mg KOH/g and could work through steric stabilization of carbon nanofibers.

Carbon nanofiber paper was fabricated by using the following procedures. The as-treated or as-received carbon nanofibers of 200 mg were grinded by placing them into a mortar and adding a small amount of solvent. After grinding, they were transferred into 500 mL beaker, and 400 mL solvent was added. The suspension was sonicated using a high intensity sonicator for 20 minutes. After the initial sonication, both the solution and the probe were cooled down to room temperature. 1 mL BYK was then added to the suspension. The suspension was sonicated for another 20 minutes under the same condition. The as-prepared suspension was allowed to settle overnight. 300 mL suspension at the upper level of the beaker was collected. The remaining 100 mL suspension containing some deposits was mixed with 200 mL solvent and sonicated for another 10 minutes. The carbon nanofiber paper was made by filtering the suspension through 0.4 μm hydrophilic polycarbonate or hydrophobic Teflon membrane under a high-pressure filtration system. The carbon nanofiber paper was further dried in oven at 120°C for 2 hours. In this study, eight groups of samples were made under various combinations of different types of carbon nanofibers, solvents, BYK, suspension, or deposit, as shown in Table 1. The samples of carbon nanofiber paper were designated based on their processing conditions. For example, RIN-OXCNF-AC-SUS-BYK represents that the sample was made from RIN-OXCNF suspension in acetone, which was dispersed with an aid of dispersant BYK. OXCNF, RIN-OXCNF, NOXCNF, and RIN-NOXCNF are four types of carbon nanofibers. Three types of solvents including water, alcohol, and acetone were used. SUS

and DEP indicate the samples from the upper suspension or the deposit, respectively.

3. Results and Discussion

3.1. Effects of Solvents. OXCNFs were dispersed in water, ethyl alcohol, and acetone. It was found that OXCNF could be easily dispersed in water and alcohol but not well dispersed in acetone. The variations in the dispersion quality are due to the surface functional groups of OXCNFs. The suspension of OXCNFs in water and ethyl alcohol was stable. But carbon nanofibers easily agglomerated in acetone once the sonication was over. Both water and alcohol are more polar solvent than acetone. The oxidized carbon nanofiber has more functional groups such as OH, COOH, and so forth in the solution. Therefore, the interaction between the polar groups (i.e., OH groups on the nanofiber and OH groups of alcohol or water) leads to better quality of dispersion. Six samples of carbon nanofiber paper were made: OXCNF-WA-SUS, OXCNF-WA-DEP, OXCNF-AL-SUS, OXCNF-AL-DEP, OXCNF-AC-SUS, and OXCNF-AC-DEP. Figures 1(a)–1(e) show the scanning electron microscopy (SEM) images of OXCNF-WA-SUS, OXCNF-AL-SUS, OXCNF-AC-SUS, OXCNF-WA-DEP, and OXCNF-AL-DEP, respectively.

Figures 1(a) and 1(d) show the SEM images of OXCNF-WA-SUS and OXCNF-WA-DEP, respectively. It can be seen that no large particles can be found in Figure 1(a). However, large particles can be clearly observed in Figure 1(d). The large particles came from the aggregates of carbon nanofibers. Carbon nanofibers with smaller diameters were closely packed in OXCNF-WA-SUS, which results in a higher bulk density of OXCNF-WA-SUS, as shown in Table 2. The metal catalyst particles can be found in both OXCNF-WA-SUS and OXCNF-WA-DEP.

Similar observation was made for OXCNF-AL-SUS and OXCNF-AL-DEP, as shown in Figures 1(b) and 1(e). It is difficult to individually disperse and separate carbon nanofibers, and the deposited carbon nanofibers became the aggregates. The difference between Figures 1(d) and 1(e) indicates that it was more difficult to separate carbon nanofibers in alcohol than in water. Larger carbon nanofiber aggregates can be found in Figure 1(e). There are more carbon nanofibers with smaller diameters shown in Figure 1(a) due to better dispersion of carbon nanofibers in water. This observation also can be made by comparing their weights shown in Table 2. About 30.5 wt% carbon nanofibers were deposited in OXCNF-AL-DEP. Only about 25.5 wt% carbon nanofibers were deposited in water. From Figures 1(a)–1(c), OXCNF-WA-SUS had good network structure of carbon nanofibers, in which no large carbon nanofiber aggregates were formed, and individual nanofibers were closely packed within the paper. It seems that the structure of carbon nanofiber paper was better in OXCNF-AC-SUS than in OXCNF-AL-SUS.

3.2. Effects of Dispersant. In order to obtain better dispersion of OXCNFs in acetone, the dispersant, BYK, was used. For OXCNF-AC-SUS-BYK and OXCNF-AC-SUS, it was found

TABLE 1: Sample identification and processing conditions.

| Sample ID | Type of carbon nanofiber | Type of solvent | Use of dispersant | Suspension or deposit |
|-----------------------|--------------------------|-----------------|-------------------|-----------------------|
| OXCNF-WA-SUS | OXCNF | Water | | SUS |
| OXCNF-WA-DEP | OXCNF | Water | | DEP |
| OXCNF-AL-SUS | OXCNF | Alcohol | | SUS |
| OXCNF-AL-DEP | OXCNF | Alcohol | | DEP |
| OXCNF-AC-SUS | OXCNF | Acetone | | SUS |
| OXCNF-AC-DEP | OXCNF | Acetone | | DEP |
| RIN-OXCNF-AC-SUS | RIN-OXCNF | Acetone | | SUS |
| RIN-OXCNF-AC-DEP | RIN-OXCNF | Acetone | | DEP |
| RIN-OXCNF-AC-SUS-BYK | RIN-OXCNF | Acetone | DISPERBYK-191 | SUS |
| RIN-OXCNF-AC-DEP-BYK | RIN-OXCNF | Acetone | DISPERBYK-191 | DEP |
| RIN-OXCNF-WA-SUS | RIN-OXCNF | Water | | SUS |
| RIN-OXCNF-WA-DEP | RIN-OXCNF | Water | | DEP |
| NOXCNF-AC-SUS-BYK | NOXCNF | Acetone | DISPERBYK-191 | SUS |
| NOXCNF-AC-DEP-BYK | NOXCNF | Acetone | DISPERBYK-191 | DEP |
| RIN-NOXCNF-AC-SUS-BYK | RIN-NOXCNF | Acetone | DISPERBYK-191 | SUS |
| RIN-NOXCNF-AC-DEP-BYK | RIN-NOXCNF | Acetone | DISPERBYK-191 | DEP |

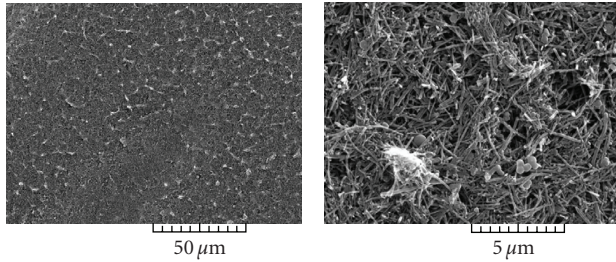
that less carbon nanofibers were deposited with the aid of the dispersant, as shown in Table 2. The dispersant or surfactant decreases the interfacial surface tension or surface energy of the solid phase like carbon nanofibers. Therefore, they can be relatively easily dissolved in the solvent. Under the same processing conditions, only 38.5 wt% of OXCNFs remained in the suspension for OXCNF-AC-SUS but 60.7 wt% of OXCNFs for OXCNF-AC-SUS-BYK. Large amount of OXCNFs were individually dispersed into acetone with the aid of BYK. Figure 2 shows the SEM images of OXCNF-AC-SUS-BYK. Compared to Figure 1(c), Figure 2 clearly indicates that more uniform network structure was formed in OXCNF-AC-SUS-BYK. In Figure 1(c), carbon nanofiber paper only consisted of straight OXCNFs with larger diameters. But there were some curved OXCNFs with smaller diameters in Figure 2. Therefore, the use of BYK could improve the dispersion of OXCNFs.

3.3. Effects of Acid Rinse. The diluted nitric acid was used to rinse carbon nanofibers. Figures 3 and 4 show the SEM images of RIN-OXCNF-AC-SUS-BYK, RIN-OXCNF-AC-DEP-BYK, RIN-OXCNF-WA-SUS, and RIN-OXCNF-WA-DEP. Compared to OXCNF-AC-SUS-BYK in Figure 2, Figure 3(a) shows uniform network structure without large OXCNF aggregates. The acid rinse improved the dispersion of OXCNFs within the paper consisting of short and small nanofibers. From Figure 1(a), it can be seen that short OXCNFs existed in bundles and filled the pores of carbon nanofiber paper. The OXCNF-WA-DEP only had 25.5 wt%, but RIN-OXCNF-WA-DEP could reach up to 38.9 wt%, as show in Table 2. Compared to Figure 1(d), Figure 4(b) shows more carbon nanofiber aggregates, although the size of carbon nanofiber aggregates in Figure 1(d) was much larger. It can be concluded that it is not necessary to treat OXCNFs with the acid rinse if the water is used as solvent. The acid

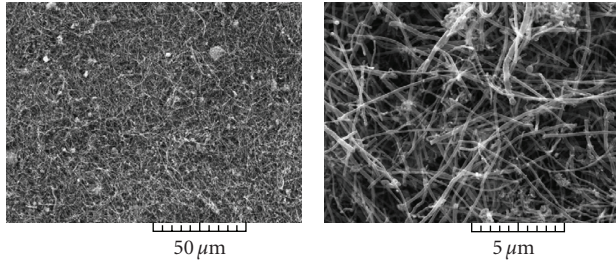
rinse could improve the dispersion of carbon nanofibers in alcohol and lead to uniform network structure.

3.4. Effects of Carbon Nanofibers. There are very few active chemical sites on the surface of NOXCNFs. Therefore, it is extremely difficult to directly disperse NOXCNFs in water and acetone. The NOXCNFs were easily aggregated after the sonication. The filtered carbon nanofiber paper had very rough surface. The NOXCNFs were deposited quickly on the bottom of the beaker in water. The NOXCNF flocules were formed in acetone. In order to obtain a stable suspension of NOXCNFs, it is necessary to use the dispersant BYK in acetone. Figure 5 shows the morphologies of NOXCNF-AC-SUS-BYK and RIN-NOXCNF-AC-SUS-BYK. For NOXCNF-AC-SUS-BYK, there were large NOXCNF aggregates, and the network structure was not uniform. But for RIN-NOXCNF-AC-SUS-BYK, the large NOXCNF aggregates disappeared, and the quality of network structures was improved. Therefore, the acid rinse enhanced the dispersion of NOXCNF in acetone.

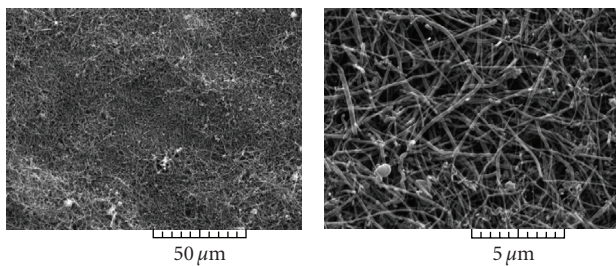
3.5. Bulk Densities of Carbon Nanofiber Paper. The bulk density is one of the important parameters of carbon nanofiber paper. The thickness, weight, weight percentage, and density of carbon nanofiber paper are shown in Table 2. The bulk densities are plotted against the sample number in Figure 6. It can be seen that all the samples made from the upper suspension had higher bulk densities than those from the deposits. This is due to the close packing of individual nanofibers uniformly dispersed in the suspension. Bars 1, 2, and 3 represent the samples made from the suspension of OXCNF in water, alcohol, and acetone, respectively. The bulk densities of these samples from the deposits decreased by following the order: water, alcohol, and acetone. The sample from the alcohol suspension has the lowest bulk



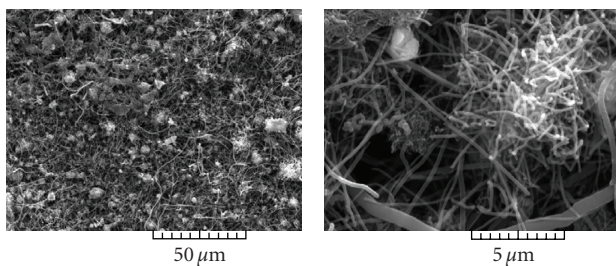
(a) OXCNF-WA-SUS



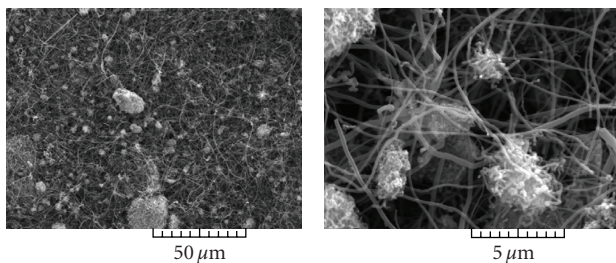
(b) OXCNF-AL-SUS



(c) OXCNF-AC-SUS



(d) OXCNF-WA-DEP



(e) OXCNF-AL-DEP

FIGURE 1: SEM images of carbon nanofiber paper: OXCNF-WA-SUS, OXCNF-AL-SUS, OXCNF-AC-SUS, OXCNF-WA-DEP, and OXCNF-AL-DEP.

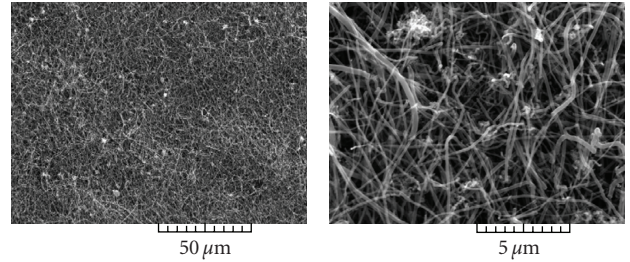
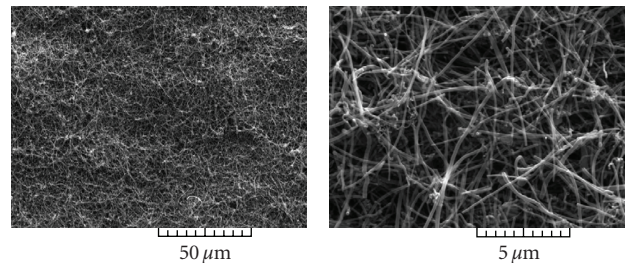
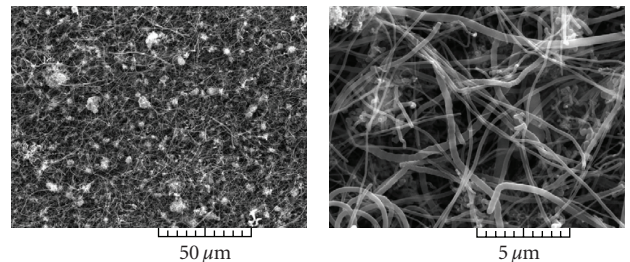


FIGURE 2: SEM images of carbon nanofiber paper: OXCNF-AC-SUS-BYK.



(a) RIN-OXCNF-AC-SUS-BYK



(b) RIN-OXCNF-AC-DEP-BYK

FIGURE 3: SEM images of carbon nanofiber paper: RIN-OXCNF-AC-SUS-BYK and RIN-OXCNF-AC-DEP-BYK.

density. This agrees very well with the SEM images shown in Figure 1. Compared to Sample 3, BYK was used for Sample 4. In Sample 5, OXCNF was rinsed with the diluted nitric acid and dispersed with the aid of BYK. Both BYK and acid rinse improved the dispersion of OXCNFs in acetone. The same phenomenon was observed for the samples made from the OXCNF aqueous solutions by comparing Samples 1 and 6. After the acid rinse, their bulk densities increased. For NOXCNF, the bulk densities of the samples from the deposits have no significant changes. However, the acid rinse increased their bulk densities for the samples from the suspension.

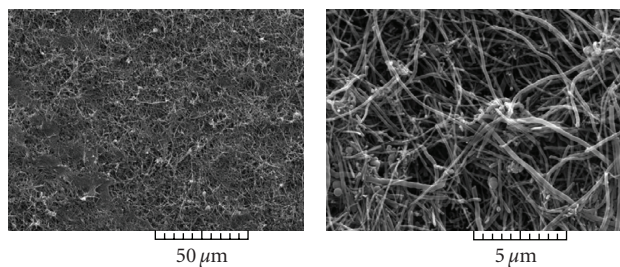
4. Conclusions

This paper systematically studied the processing-structure relationship of carbon nanofiber paper. It is clearly seen that the dispersion of carbon nanofibers in solvents played an important role in determining the network structures

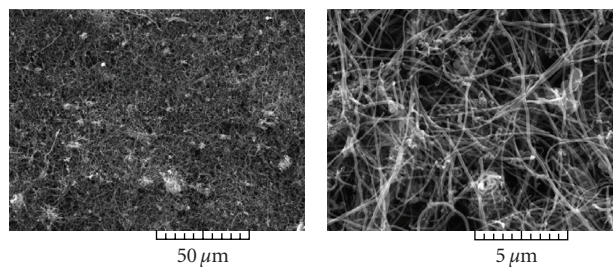
TABLE 2: Bulk densities of carbon nanofiber papers.

| Sample ID | Sample number | Thickness (mm) | Weight (mg) | Weight percentage ^(a) (wt%) | Bulk density ^(b) (g/cm ³) |
|-----------------------|---------------|----------------|-------------|--|--|
| OXCNF-WA-SUS | 1 | 0.346 | 158 | 74.5 | 0.383 |
| OXCNF-WA-DEP | | 0.149 | 54 | 25.5 | 0.304 |
| OXCNF-AL-SUS | 2 | 0.563 | 141 | 69.5 | 0.210 |
| OXCNF-AL-DEP | | 0.274 | 62 | 30.5 | 0.189 |
| OXCNF-AC-SUS | 3 | 0.256 | 77 | 38.5 | 0.252 |
| OXCNF-AC-DEP | | 0.768 | 123 | 61.5 | 0.134 |
| OXCNF-AC-SUS-BYK | 4 | 0.384 | 125 | 60.7 | 0.272 |
| OXCNF-AC-DEP-BYK | | 0.371 | 81 | 39.3 | 0.183 |
| RIN-OXCNF-AC-SUS-BYK | 5 | 0.294 | 114 | 59.1 | 0.324 |
| RIN-OXCNF-AC-DEP-BYK | | 0.288 | 79 | 40.9 | 0.231 |
| RIN-OXCNF-WA-SUS | 6 | 0.237 | 121 | 61.1 | 0.426 |
| RIN-OXCNF-WA-DEP | | 0.160 | 77 | 38.9 | 0.403 |
| NOXCNF-AC-SUS-BYK | 7 | 0.845 | 134 | 67 | 0.133 |
| NOXCNF-AC-DEP-BYK | | 0.461 | 66 | 33 | 0.120 |
| RIN-NOXCNF-AC-SUS-BYK | 8 | 0.474 | 108 | 52.7 | 0.191 |
| RIN-NOXCNF-AC-DEP-BYK | | 0.614 | 97 | 47.3 | 0.132 |

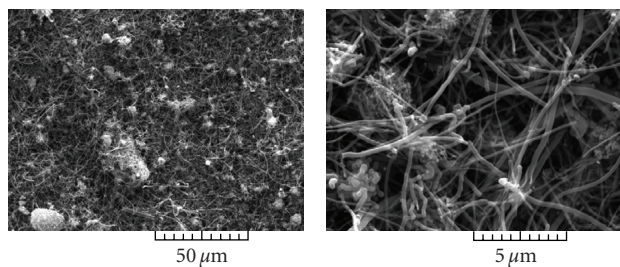
Note: (a) Total weight of carbon nanofibers from the suspension and deposit; (b) sample diameter 39 mm.



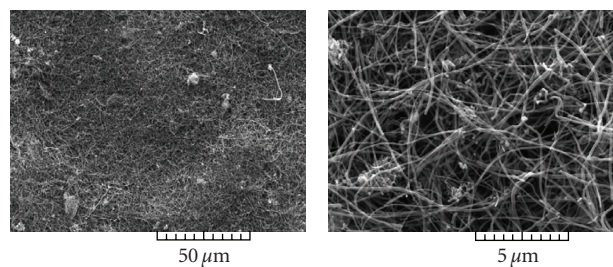
(a) RIN-OXCNF-WA-SUS



(a) NOXCNF-AC-SUS-BYK



(b) RIN-OXCNF-WA-DEP



(b) RIN-NOXCNF-AC-SUS-BYK

FIGURE 4: SEM images of carbon nanofiber paper: RIN-OXCNF-WA-SUS and RIN-OXCNF-WA-DEP.

FIGURE 5: SEM images of carbon nanofiber paper: NOXCNF-AC-SUS-BYK and RIN-NOXCNF-AC-SUS-BYK.

of carbon nanofiber paper. The good dispersion led to close packing of carbon nanofibers, which formed the uniform network structure of the paper with a higher bulk density. The variations in the dispersion quality caused the changes in the network structures and densities of carbon nanofiber paper. The types of solvents, dispersant, acid rinse, and types of carbon nanofibers significantly affected the dispersion quality. It has been found that OXCNFs were

easily dispersed in water and alcohol but not well in acetone due to the functional groups on the fiber surface. Although there were few functional groups on NOXCNFs, they were easily dispersed in acetone with the aid of dispersant. In addition, the treatment with diluted nitric acid improved the dispersion in the solvents. Therefore, the network structure of carbon nanofiber paper can be controlled and optimized by choosing appropriate processing parameters.

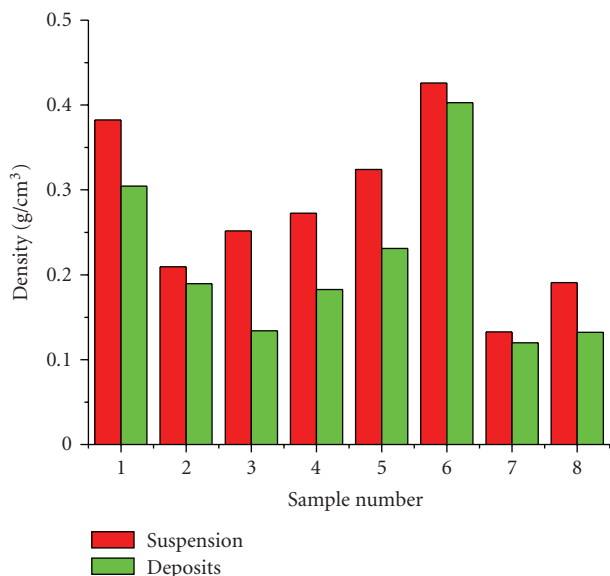


FIGURE 6: Bulk densities of carbon nanofiber papers.

Acknowledgments

This material is based upon work supported by the National Science Foundation's nanomanufacturing program under Grant no. 0757302 managed by program manager, Dr. Shaochen Chen. The acknowledgment is also made to Florida Center for Advanced Aero-Propulsion (FCAAP) program under Grant no. FSU#218007-530-024809-R010689. Any opinions, findings, and conclusions or recommendations expressed in this material are those of the authors and do not necessarily reflect the views of the National Science Foundation.

References

- [1] A. K.-T. Lau and D. Hui, "The revolutionary creation of new advanced materials—carbon nanotube composites," *Composites Part B*, vol. 33, no. 4, pp. 263–277, 2002.
- [2] E. T. Thostenson, Z. Ren, and T.-W. Chou, "Advances in the science and technology of carbon nanotubes and their composites: a review," *Composites Science and Technology*, vol. 61, no. 13, pp. 1899–1912, 2001.
- [3] D. Qian, E. C. Dickey, R. Andrews, and T. Rantell, "Load transfer and deformation mechanisms in carbon nanotube-polystyrene composites," *Applied Physics Letters*, vol. 76, no. 20, pp. 2868–2870, 2000.
- [4] D. Qian and E. C. Dickey, "In-situ transmission electron microscopy studies of polymer-carbon nanotube composite deformation," *Journal of Microscopy*, vol. 204, no. 1, pp. 39–45, 2001.
- [5] P. M. Ajayan, L. S. Schadler, C. Giannaris, and A. Rubio, "Single-walled carbon nanotube-polymer composites: strength and weakness," *Advanced Materials*, vol. 12, no. 10, pp. 750–753, 2000.
- [6] L. S. Schadler, S. C. Giannaris, and P. M. Ajayan, "Load transfer in carbon nanotube epoxy composites," *Applied Physics Letters*, vol. 73, no. 26, pp. 3842–3844, 1998.
- [7] L. Jin, C. Bower, and O. Zhou, "Alignment of carbon nanotubes in a polymer matrix by mechanical stretching," *Applied Physics Letters*, vol. 73, no. 9, pp. 1197–1199, 1998.
- [8] C. Bower, R. Rosen, L. Jin, J. Han, and O. Zhou, "Deformation of carbon nanotubes in nanotube-polymer composites," *Applied Physics Letters*, vol. 74, no. 22, pp. 3317–3319, 1999.
- [9] Z. Ounaies, C. Park, K. E. Wise, E. J. Siochi, and J. S. Harrison, "Electrical properties of single wall carbon nanotube reinforced polyimide composites," *Composites Science and Technology*, vol. 63, no. 11, pp. 1637–1646, 2003.
- [10] C. Stéphan, T. P. Nguyen, M. Lamy de la Chapelle, S. Lefrant, C. Journet, and P. Bernier, "Characterization of singlewalled carbon nanotubes-PMMA composites," *Synthetic Metals*, vol. 108, no. 2, pp. 139–149, 2000.
- [11] M. S. P. Shaffer and A. H. Windle, "Fabrication and characterization of carbon nanotube/poly(vinyl alcohol) composites," *Advanced Materials*, vol. 11, no. 11, pp. 937–941, 1999.
- [12] J. Sandler, M. S. P. Shaffer, T. Prasse, W. Bauhofer, K. Schulte, and A. H. Windle, "Development of a dispersion process for carbon nanotubes in an epoxy matrix and the resulting electrical properties," *Polymer*, vol. 40, no. 21, pp. 5967–5971, 1999.
- [13] X. Y. Gong, J. Liu, S. Baskaran, R. D. Voise, and J. S. Young, "Surfactant-assisted processing carbon nanotube/polymer composites," *Chemistry of Materials*, vol. 12, no. 4, pp. 1049–1052, 2000.
- [14] Z. Jin, K. P. Pramoda, G. Xu, and S. H. Goh, "Dynamic mechanical behavior of melt-processed multi-walled carbon nanotube/poly(methyl methacrylate) composites," *Chemical Physics Letters*, vol. 337, no. 1–3, pp. 43–47, 2001.
- [15] K. Lozano and E. V. Barrera, "Nanofiber-reinforced thermoplastic composites—I: thermoanalytical and mechanical analyses," *Journal of Applied Polymer Science*, vol. 79, no. 1, pp. 125–133, 2001.
- [16] K. Lozano, J. Bonilla-Rios, and E. V. Barrera, "A study on nanofiber-reinforced thermoplastic composites (II): investigation of the mixing rheology and conduction properties," *Journal of Applied Polymer Science*, vol. 80, no. 8, pp. 1162–1172, 2001.
- [17] R. Haggenueller, H. H. Gommans, A. G. Rinzler, J. E. Fischer, and K. I. Winey, "Aligned single-wall carbon nanotubes in composites by melt processing methods," *Chemical Physics Letters*, vol. 330, no. 3–4, pp. 219–225, 2000.
- [18] Z. J. Jia, Z. Y. Wang, C. L. Xu, et al., "Study on poly(methyl methacrylate)/carbon nanotube composites," *Materials Science and Engineering A*, vol. 271, no. 1–2, pp. 395–400, 1999.
- [19] C. Park, Z. Ounaies, K. A. Watson, et al., "Dispersion of single wall carbon nanotubes by in situ polymerization under sonication," *Chemical Physics Letters*, vol. 364, no. 3–4, pp. 303–308, 2002.
- [20] F. H. Gojny, M. H. G. Wichmann, B. Fiedler, W. Bauhofer, and K. Schulte, "Influence of nano-modification on the mechanical and electrical properties of conventional fibre-reinforced composites," *Composites Part A*, vol. 36, no. 11, pp. 1525–1535, 2005.
- [21] F. H. Gojny, M. H. G. Wichmann, U. Köpke, B. Fiedler, and K. Schulte, "Carbon nanotube-reinforced epoxy-composites: enhanced stiffness and fracture toughness at low nanotube content," *Composites Science and Technology*, vol. 64, no. 15, pp. 2363–2371, 2004.
- [22] J. Gou, S. O'Braint, H. Gu, and G. Song, "Damping augmentation of nanocomposites using carbon nanofiber paper," *Journal of Nanomaterials*, vol. 2006, Article ID 32803, 7 pages, 2006.

- [23] J. Gou, "Single-walled nanotube bucky paper and nanocomposite," *Polymer International*, vol. 55, no. 11, pp. 1283–1288, 2006.
- [24] J. Gou, Z. Liang, and B. Wang, "Experimental design and optimization of dispersion process for single-walled carbon nanotube bucky paper," *International Journal of Nanoscience*, vol. 3, no. 3, pp. 293–307, 2004.

Research Article

Bulk Behavior of Ball Milled AA2124 Nanostructured Powders Reinforced with TiC

Hanadi G. Salem,¹ Sherif El-Eskandarany,² Amr Kandil,² and Hassan Abdul Fattah²

¹ Department of Mechanical Engineering, The Yousef Jameel Science and Technology Research Center, The American University in Cairo, AUC Avenue, New Cairo 11835, Egypt

² Department of Mining, Metallurgy and Petroleum Engineering, Al-Azhar University, Cairo, Egypt

Correspondence should be addressed to Hanadi G. Salem, hgsalem@aucegypt.edu

Received 22 November 2008; Accepted 9 April 2009

Recommended by Alan K. T. Lau

In the current research work, a top-down approach was employed for the refinement of a micron scale AA2124 alloy powder $40\ \mu\text{m}$ in average size using high-energy ball milling up to 60 hours. The produced nanopowders were investigated compared to the micron gas atomized powder both in the monolithic and the reinforced composite states. $1\ \mu\text{m}$ powder of TiC with internal structure $<100\ \text{nm}$ was used for the reinforcement of the 2124-Al matrices. Milling time of 36 hours produced a $<100\ \text{nm}$ nanopowders with internal structure size $<20\ \text{nm}$. The nanopowder monolithic consolidates exhibited compressive strength of 388 MPa compared to 313 MPa for micronpowder one. Addition of TiC nanostructured powder to the nanopowder consolidated matrix resulted in increase of 130% in compressive strength compared to that produced for the microscale one. Nanopowder of Alalloys produced by mechanical milling reinforced with 10 wt% TiC is recommended for products suitable for high wear and erosion resistance applications. Peak aging increased the hardness and compressive strength of the as compacted micronpowder matrices by an average of 188% and 123%, while increased that of the nanopowder matrices by an average of 110% and 117%, respectively.

Copyright © 2009 Hanadi G. Salem et al. This is an open access article distributed under the Creative Commons Attribution License, which permits unrestricted use, distribution, and reproduction in any medium, provided the original work is properly cited.

1. Introduction

Composite materials are known for their multiple functionalities due to the ability of tailoring the composite properties through controlling the type, composition, and morphology of the matrix and reinforcement. Metal Matrix Composite (MMC) has been developed to meet specific properties that cannot be met by a monolithic material regardless of its composition or processing technique (thermomechanical treatment). MMC can be tailored in different methods depending on the type and shape of the reinforcing phase (dispersion, particulate, whiskers, or fiber) and the consolidation technique produced to produce the bulk product [1]. The sintering behavior of metal matrix nanocomposites has been investigated for different matrices such as Ti [2], Cu [3], and Al-matrices [1, 4–9] with various ceramic reinforcements. Ti and Al-powders suffer from the formation of an oxide stable and brittle film, which strongly influences

the consolidation behavior of the produced consolidates and hence their mechanical and physical properties [2].

Metal matrix composites reinforced with ceramic reinforcements have been extensively studied over the last two decades for their significant use in aerospace aircraft, automobile, and military applications [4–9]. Reinforcement of micron scale ceramic particles used to improve the yield and ultimate strength of the matrix metal on the expense of losing toughness and ductility. Al-composites exhibit high specific strength and modulus, low density. AA2024 metallic powders became of great interest as matrices suitable for particulate reinforcement with ceramic powders especially SiC [10–13].

Carbides, oxides, and nitrides powder have been used extensively for the reinforcement of Alalloys. In specific, SiC and Al_2O_3 were the commonly used ceramic reinforcements. TiC was not investigated enough as a ceramic reinforcement to Alalloys; however, it has been receiving much attention

TABLE 1: Chemical composition (wt%) of the AA2124 metallic matrix and TiC powders.

| Matrix Powder | Cu | Mg | Mn | Si | Fe | Al | |
|----------------------|---------|---------|---------|----------------|----------------|---------|---------|
| AA2124 | 3.8–4.0 | 1.4–1.6 | 0.5–0.7 | 0.1max | 0.1max | Balance | |
| Reinforcement Powder | Total C | Free C | Fe | N ₂ | O ₂ | Wax | Ti |
| TiC | 19.71 | 0.16 | 0.20 | 0.30 | 0.87 | 0.15 | Balance |

lately for its high melting temperature (3373 K), low thermal coefficient of expansion, extraordinary hardness, excellent wear, and abrasion resistance [14]. The MMC processing parameters have a significant effect on the properties of the produced bulk product. Amongst those parameters, we have type size and shape of both the metallic matrix and the reinforcement particles, as well as the consolidation technique, pressure, temperature, and time. Many studies focused on the effect of the particle size of the matrix relative to the reinforcement within the microscale [4–9]. Other studies focused on the powder consolidation process including hot compaction, Hot and cold isostatic pressing followed by sintering and recently, plasma activated sintering [8, 9].

Nanostructured materials exhibit relatively high interfacial energy compared to microstructural materials. The amount of energy stored by the nanostructured materials depends very strongly on the sensitization and processing techniques used for producing Bulk nanostructures material (BNSM). Several techniques have been employed for the synthesis of nanopowders, such as powder atomization and mechanical milling [15–17]. Mechanical milling especially ball milling produces nanopowders with very high stored energy induced by the continuous impact of the powder particles with stainless steel balls. The nature of interaction of the hardened balls and powder particles results in the strain hardening of the particles followed by their fragmentation into finer ones [18]. The amount of stored energy depends on the type of material, the milling time, speed, and temperature. For Alalloys, grain size of 20nm was reported by Lin et al. [19], which was measured using XRD patterns and observed by TEM.

Nanoscale materials have been the subject of major interest in recent years due to the anticipated ultrahigh strength and toughness combination that can be achieved in contrast to materials with conventional meso and microscale structures [1–3]. Reinforcement with nanoscale ceramic powders or the use of nanostructured powders of both the matrix and reinforcement producing nanocomposites derived the attention of the researchers to produce ultrahigh strength/tough MMCs. The key issue lies in the optimization of the processing parameters suitable for the production of BNSM with superior properties suitable for high and cryogenic temperature applications. It has been reported that extrusion of a cryomilled nanostructured Al-Mg alloy with grain size of 20–30 nm resulted in grain size coarsening up to 90 nm [19]. The degree of grain size coarsening is significantly affected by the alloying elements in the Al alloy, which controls the thermal stability of the powder during the consolidation stages.

Consolidation of bulk products starting from nanopowders represents an additional challenge for materials designed with superior properties. BNSM produced from the consolidation of mechanically milled powders could produce products with promising superior properties due to the relatively produced fine high energetic hard powders. On the other hand, the high hardness induced in the milled powder particles retards the particles' deformation during the compaction stages that is necessary for filling the empty spaces formed in between the particles to enhance consolidation. Accordingly, this research aims for the production of sound BNS consolidates of nanopowders with improved mechanical properties over those of the micron powder of the same material. This involves the fabrication of a nanoscale AA2124 powder by mechanical milling of a microscale as-received powder using high-energy ball milling. Influence of the hot compaction parameters on the consolidation behavior of the milled powders compared to the as-received one is investigated. Effect of ceramic nanopowders reinforcement additions on the consolidation behavior of both matrices is also investigated.

2. Materials and Experimental Procedure

In the current research, a top-down approach was employed for the refinement of a gas atomized micronpowders of AA2124 alloy with particle size ranging between 5–85 μm with an average size of 40 μm . The as-received AA2124 and TiC powders were supplied by the Aluminum powder Company limited (APC) and Mitsuwa Chemicals Co. LTD, respectively. The chemical composition for the Al 2124 powder and TiC is shown in Table 1. The TiC particle size ranged between 0.85–5 μm with an average size of 1.0 μm . The refinement process was conducted using a FRITCH high-energy ball milling up to 60 hours at 500 rpm in agate jars with ball-to-powder ratio of 30 : 1. The ball milling investigation intervals were 6, 12, 24, 36, 48, and 60 hours. Density measurement and the effect of the sample aspect ratio h/d (height-to-diameter ratio) were characterized for the compact produced from powders milled for 24 and 36 hours compared to the as-received one. Influence of the matrices powder size and mechanical properties on the TiC ceramic reinforcement distribution was investigated for the 0-hour powders (as-received micronpowder) and powders milled for 24 hours (nanopowders). A turbula mixer was employed for the production of mixtures of 5, 10, and 20 wt% of the 1 μm TiC powder in both matrices.

X-ray diffraction was used to determine the crystallite size of the milled powders compared to the as-received one. The X-Ray diffractometer used is a Diano Co, energized at

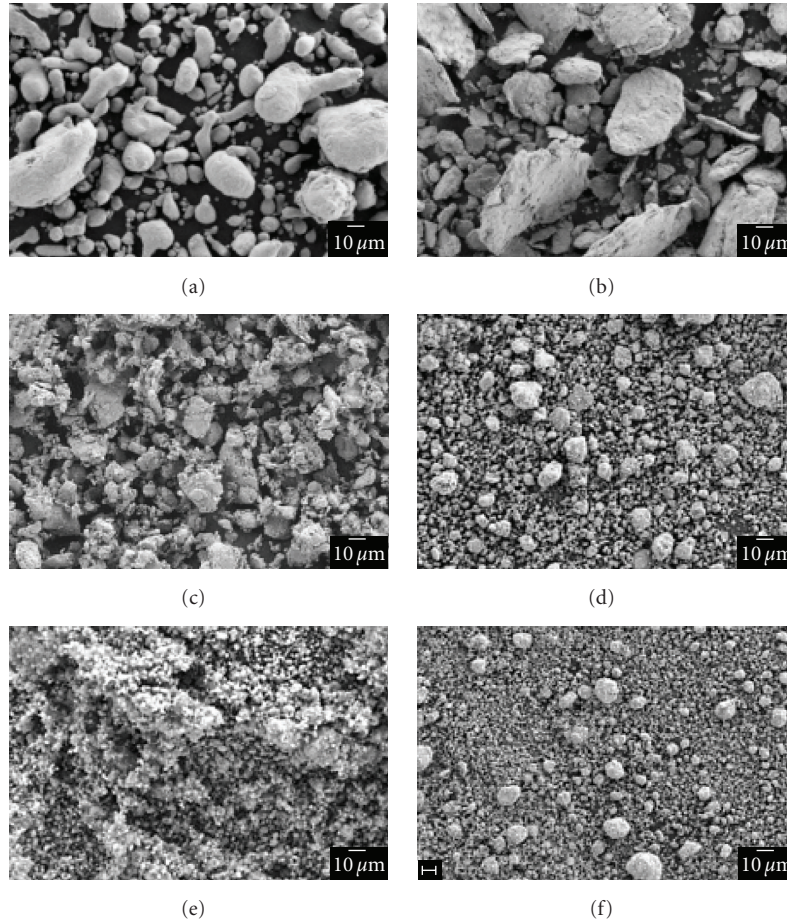


FIGURE 1: AA2124 particle morphology evolution with increasing milling time (a) 0 hour, (b) 6 hours, (c) 12 hours, (d) 24 hours, (e) 36 hours, and (f) 60 hours.

45 kV and 10 mA with a dead time of less than 10^{-6} seconds. A step scanning mode using Ni-filter $\text{CuK}\alpha$ radiation was used to determine the crystallite size and to trace any structural changes that might have taken place during the refinement of the AA2124 powder during milling. A Leo high resolution field emission scanning electron microscope (SEM) was employed to characterize the milled powder morphology and the topology of the compact samples.

The as-received and milled powders were consolidated into compacts using cold and hot unidirectional pressing at 624 MPa with a pressing holding time of 30 minutes. Tool steel die with an inner diameter of 20 mm was used to consolidate the samples at 480°C (0.75Tm). Height-to-diameter aspect ratios (h/d) of 0.25, 0.5, and 1.0 for the compact samples were investigated for the micron (as-received) and nanoscale (24 hours MT) matrices with and without TiC additions. A Licka optical microscope was used to investigate the microstructural evolution of the hot compacts (HCs) as a function of the various compaction parameters. Vickers microhardness was used to determine hardness of the consolidates using a Mitutoyo microhardness tester. The VHN measurements was conducted at 200 gm for 15 seconds of dwell time. A minimum of 5 indentations

were measured per condition. Compressive strength of the produced consolidates was evaluated using round 20 mm diameter and 5 mm height discs. A 50 tons MTS Universal testing machine was employed for conducting the compression tests at a cross-head speed of 0.5 mm/min. A minimum of 3-samples per condition was tested for compression, the average of which was reported.

3. Results and Discussion

In the current work, particle morphology and structure size were characterized for the ball milled as-received AA2124 powder for periods of 6, 12, 24, 36, 48, and 60 hours. Densification of the compact AA2124 powders was characterized for the 0, 24, and 36 hours milling times.

3.1. Influence of Mechanical Iteration on the AA2124 Micron-powders. Figure 1 shows the SEM images of the milled powders after 0, 6, 12, 24, 36, 48, and 60 hours of milling time. The as-received microscale Al-powder was made of irregular shaped particles with maximum size of $85\ \mu\text{m}$ and about 60 vol.% of the particles with sizes $<40\ \mu\text{m}$ (Figure 1(a)).

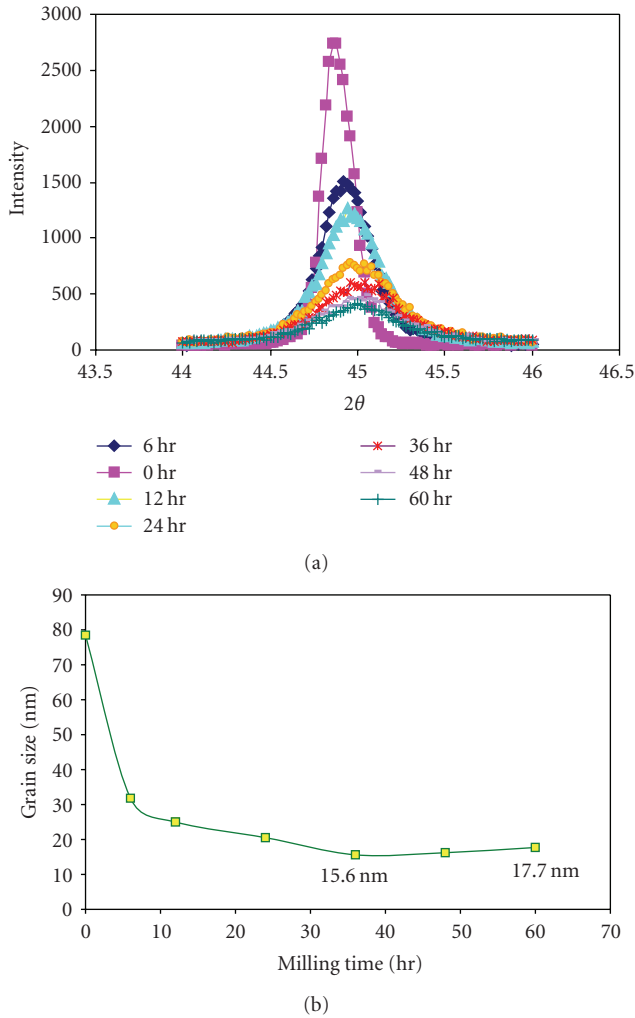


FIGURE 2: Effect of milling time on (a) X-ray diffraction $(200)_{Al}$ peak and (b) crystallite size.

Figure 2 shows the corresponding XRD patterns for the powders as a function of the milling time (MT). After 6 hours of MT, the powder particles were severely deformed and agglomerated into disc-like flaky particles with 6–63 μm in size and 2–12.7 μm in thickness. This was a result of the repeated welding during milling. This agrees with the observations made by Chen et al. who investigated the effect of milling time on Ni-Al alloys [20]. Further milling resulted in increased deformation and strain hardening, and hence the agglomerated discs were disintegrated into fragments of finer cluster ranging between 1–30 μm in size (Figure 1(c)). Milling up to 24 hours produced spherical-shaped clusters of particles ranging between 5–45 μm . Those clusters were made of very fine particles <300 nm in size, which were revealed easily at higher magnifications. Some of the refined powder was also observed separately scattered between the clusters (Figure 1(d)). Increasing the MT up to 36 hours produced ultrafine feathery like-shaped nanoscale powder <100 nm in size that was agglomerated in clusters ranging between 2–30 μm in size (Figure 1(e)). Milling the

Al-powder for 48 followed by 60 hours did not result into further reduction of the individual particles' size below that produced at 36 hours; however, the cluster morphology developed into a more spherical well-defined clusters ranging between 0.3–11 μm in size as shown in Figure 1(f). X-ray diffraction peaks from the $(200)_{Al}$ planes show a significant decrease in intensity as well as broadening with increasing the MT from 0 to 60 hours.

To determine the powder grain size (D), broadening of X-ray diffraction peaks from the $(200)_{Al}$ planes was employed for substitution in Scherrer's equation [5, 21]. Figure 2 shows the effect of milling time on the intensity and broadening of the $(200)_{Al}$ peaks at $2\theta = 44^\circ$. Increasing the MT to 6 hours resulted in a significant refinement of the crystallite size from an average of 78-to-32 nm as shown in Figure 2(b). Further milling resulted in a gradual refinement in the crystallite size to a minimum of 15.6 nm at 36 hours of milling time. Increasing the MT above 36 hours did not result into further structural refinement. The observed slight increase in crystallite size up to 17.7 nm although insignificant could be due to the heat generated during the long period of MT up to 60 hours, which may result into coarsening of the nanoscale structure. Milling beyond 60 hours is necessary to trace the structural behavior with increasing MT.

3.2. Influence of the Powder Particle Morphology and Its Grain Size on the Green Compact Properties. The effect of particle size on the compaction relative density of the compacts was investigated. Milling times of 0, 24, and 36 were selected for this analysis. Figure 3 shows high magnification SEM images for the powders, which reveals the internal structure refinement of the powder as a function of milling time. The as-received powder (Figure 3(a)) shows that the powders have smooth surfaces with orange skin-like topology, which represents a typical morphology for the gas atomized powders. The average size of the observed internal structures was about 350 nm. Finer particles do not reveal their internal structure which could be due to being much finer than that measured for the coarser particles. Powder milled for 24 hours shows clusters of fine particles with evidence for excessive deformation. Fine grains <88 nm in size were revealed (marked by arrows in Figure 3(b)). Increasing the milling time to 36 hours revealed the formation of much finer clusters heavily deformed and very fine internal structure <40 nm in size (marked by arrows in Figure 3(c)). This agrees to a great extent with the crystallite size measurements produced by EDX analysis (Figure 2(a)).

Cold compaction was conducted in a die 20 mm in diameter for powder volumes that produced h/d ratios of 0.25, 0.5, and 1.0 at a constant pressure of 624 MPa for 30 minutes. Effect of particle size on the extent of densification was determined by Archimedes' principle using three randomly selected samples [22]. Figure 4 shows the effect of milling time on the degree of densification as a function of h/d ratio. Obviously, increasing the MT led to a decrease in the powders' particle size from an average of 40 μm -to-90 nm produced green compacts with a lower

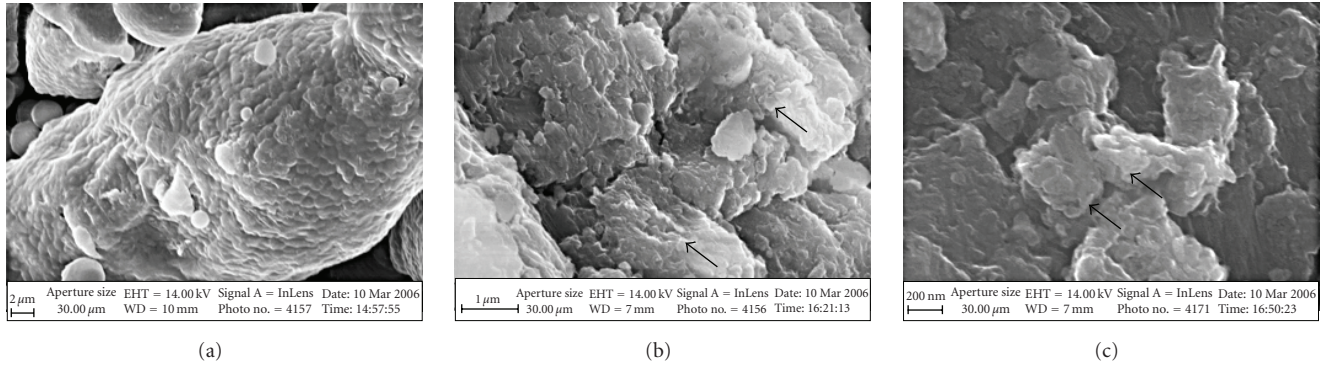


FIGURE 3: SEM micrographs for the (a) as-received powder, (b) 24 hours MT, and (c) 36 hours MT.

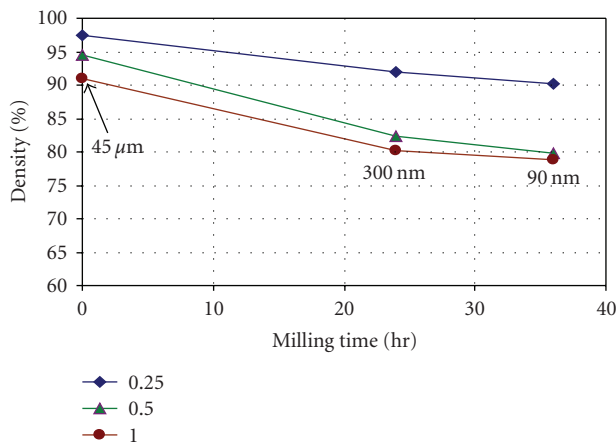


FIGURE 4: Effect of MT on the relative change in density of GC produced at compaction pressures of 624 MPa for 30 minutes and h/d ratios of 0.25, 0.5, and 1.0.

density regardless of the h/d ratio. On comparing the effect of h/d ratio on the percent decrease in density for the 40 μm (24 hours) and 90 nm (36 hours) particle sizes, about 13.4% and 7.5% were measured for h/d ratio of 0.25 and 1.0, respectively. This indicates that smaller h/d ratio not only produced higher green compact densities but also improved the densification of the nanoscale particles compared to the microscale one.

Figure 5 shows high resolution SEM images at low and high magnifications for the 40 μm (0 hour), 300 nm (24 hours) and 90 nm (36 hours) green compact powder at h/d ratio of 0.25. It is observed that the 0 hour particles formed large porosity at triple points although finer particles were entrapped between the bigger ones. The 36 hours milled powder shows more uniform distribution of the pores in between the fragmented hard fine particles. For the 24-hour milled powders, particle refinement increased the particle-to-particle contact surfaces, which reduced porosity. Higher magnification images revealed clearly the internal structure of the as-received 0 hour powders, which was about 500 nm in average size. On the other hand the milled powders for 24 and 36 hours images did not reveal the internal

structure due to the intensity of plastic deformation induced by milling. The nanopowder green compaction behavior can be attributed to the resistance of the strain hardened nanopowders to the imposed pressure compared to that of the micronpowder, which agrees with the observations made by Srivatsan et al. [23].

3.3. Effect of TiC-Wt% Reinforcement Additions on the Micro and Nanopowder AA2124 Matrices. The consolidation behavior of the as-received gas atomized micronpowder (40 nm particle size with 78 nm crystallite size) and the 24-hour milled nanopowders (300 nm particle size with 20 nm crystallite size) were mixed with 0, 5, 10, and 20 TiC wt% nanostructured powders. Figure 6 shows SEM micrographs at low and high magnifications for the TiC powder. The TiC particles are random in shape and range between 140 nm-5 μm in size.

Characterization of the consolidation behavior of the produced nanocomposites was conducted for the green and hot compacts. After mixing of the powders, a compaction load of 624 MPa for 30 minutes and 0.25 h/d ratio were used for cold compaction. Figure 7 shows the effect of adding TiC nanostructured powder on the degree of densification of the AA2124 micro and nanopowders after cold compaction. It is clear that the observed decrease in density with the refinement of the powder from the micron to the nanoscale level of the bare matrix (Figure 4) was carried over to the produced densities of the reinforced condition for both the green and hot compacts. Hot compaction of the unreinforced matrices, however, resulted in a significant increase in density of both powders, especially for the nanoscale one. A 7% versus 2.4% increase in relative density was measured for the nano and microscale powders by hot compaction, respectively. It is suggested that powder milling for 24 hours resulted in the strain hardening of the produced powders, which hindered the deformation of the powder particles under the applied load used during cold compaction which resulted in the measured low density (92%). Conversely, the as-received micronpowder produced by gas atomization is expected to be relatively soft, which facilitated the deformation and hence resulted in filling of the empty spaces between the individual powder particles. This could be sustained by the observations

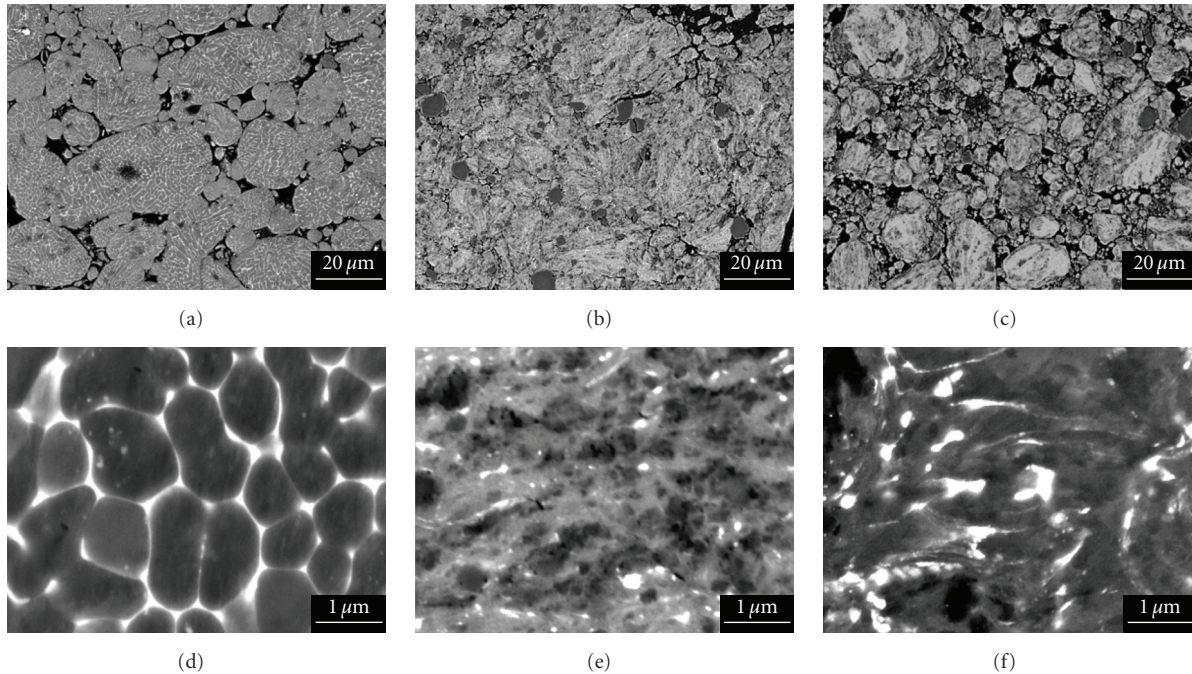


FIGURE 5: SEM images at low and high magnifications for the (a) 40 μm , (b) 300 nm, and (c) 90 nm green compact powders with 0.25 h/d ratio, respectively.

made in Figures 5(a) and 5(b). Heating of the nanopowders under pressure allowed for the sliding of fine individual nanoparticles and the small clusters to slide in between the coarser clusters, which enhances the densification of the produced hot compacts.

5 wt% addition of TiC did not result in a noticeable change in the densification degree for both types of hot compact matrices. However, increasing the TiC content resulted in a significant decrease in relative density as shown in the figure. Further addition of TiC to both matrices resulted in deterioration in density of the produced compacts; although, hot compactions resulted in a significant enhancement in density. 9% and 7.4% increase in density was achieved by hot compaction of the nano and microscale reinforced matrices with 20 wt% TiC, respectively.

Figure 8 shows the SEM micrographs for the microscale and nanoscale Al matrix green compacts reinforced with 0, 5, 10, and 20 wt% TiC. It was observed that reinforcement of the AA2124 matrices with 5 wt% TiC resulted in the formation of isolated large voids especially in the microscale particles, which explains the significant decrease in density. It is clear that local diffusion between the microparticles without reinforcement (Figures 8(a)–8(d)) was reduced significantly due to the accumulation of the TiC fine particles on the surface of the Al matrix particles. The difference in particle size of the TiC particles compared to the Al matrix particles promoted the lack of uniform distribution of the reinforcement within the matrix and hence resulted in the observed drop in density that was observed in Figure 7. Conversely, the nanoscale Al matrix did not suffer a significant drop in density by adding TiC particles compared

to the unreinforced condition (Figure 8(e)) due to the size compatibility with the matrix fine agglomerates, which can be observed at higher magnification images shown in Figures 8(f)–8(h).

In the microscale matrix composite green compacts (Figures 8(b) and 8(c)) the observed pores were formed between the individual particles, while in the nanopowder matrix two types of pores were observed (a) large interagglomerate pores and (b) small pores between the individual nanoparticles (Figures 8(f) and 8(g)). It is clear that localization of the reinforcement is occurring between the particles of the nanoparticles and the agglomerates of the nanopowder clusters. This agrees with the findings of Srivatsan et al. [23]. Previous investigations revealed that a green compact densification can increase if the applied pressure during compaction breaks down the agglomerates, which produces homogeneous small interparticle pore distribution. This in turn will improve the consolidate properties. Breaking down of the agglomerated cluster depends on the powder fabrication method, which controls the degree by which the agglomerated clusters resist deformation [23].

The observed decrease in density with addition of TiC to the nanopowder matrix disagrees with the produced increase in density observed by El-Eskandarany, who investigated the effect of adding SiC to Al matrix [8]. This could be explained by the difference in processing of the nanocomposites in both cases. El-Eskandarany produced the nanoscale composite through the simultaneous ball milling of SiC reinforcing particles with the Al matrix and produced Al/SiC nanocomposite particles made out of uniformly distributed nanoparticles of the reinforcement phase encapsulated within Al

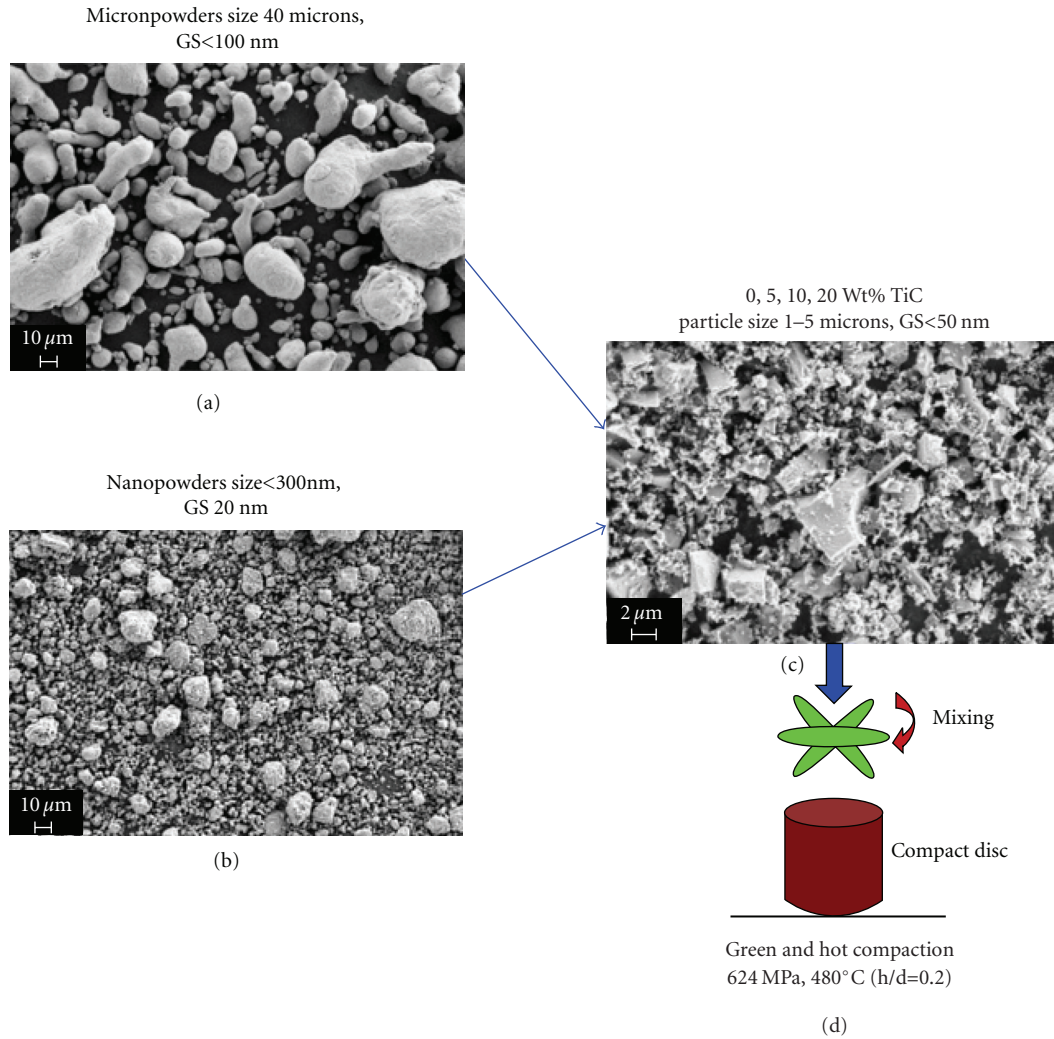


FIGURE 6: SEM images for (a) as-received microcrystalline micronpowder, (b) Nanocrystalline nanopowders milled 24 hours, (c) TiC powder, and (d) compaction conditions of the produced mixtures.

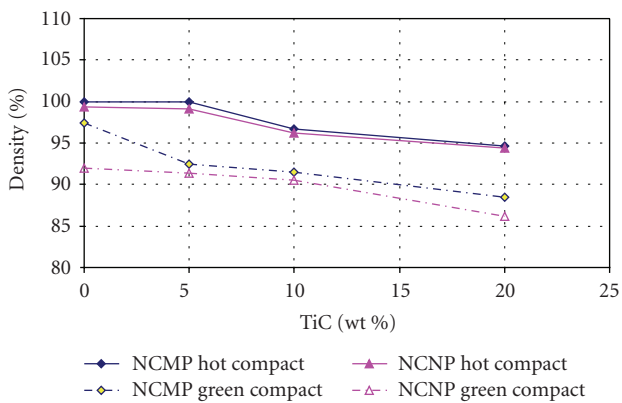


FIGURE 7: Effect of TiC addition on the density variation of the micro and nanopowder matrices green and hot compacts.

matrix. Hence the densification process is expected to be different from that used in the current research, where the Al

matrix was first refined via ball milling into the nanopowder matrix followed by mixing it with the TiC particles. This could have resulted in the segregation of the reinforcing particulates along the boundaries between the Al matrix nanoparticles. As a result a lack of diffusion between the particles occurred and hence increased the void volume fraction. This was confirmed through investigation of the green compact specimens using SEM.

In order to investigate the mechanical behavior of HC micronpowder versus the nanopowder with and without TiC reinforcement, microhardness testing was conducted. Note, the microhardness testing investigates the particle-to-particle bond strength regardless of the densification degree, since the performed indentations were conducted only in dense consolidated regions on the surface of the specimen. Figure 9 shows the effect of TiC additions on the VHN-values produced for both the micro and nanoscale hot compacts matrices.

It is observed that the hardness of the monolithic nanopowder HC is higher than that of the micron one by

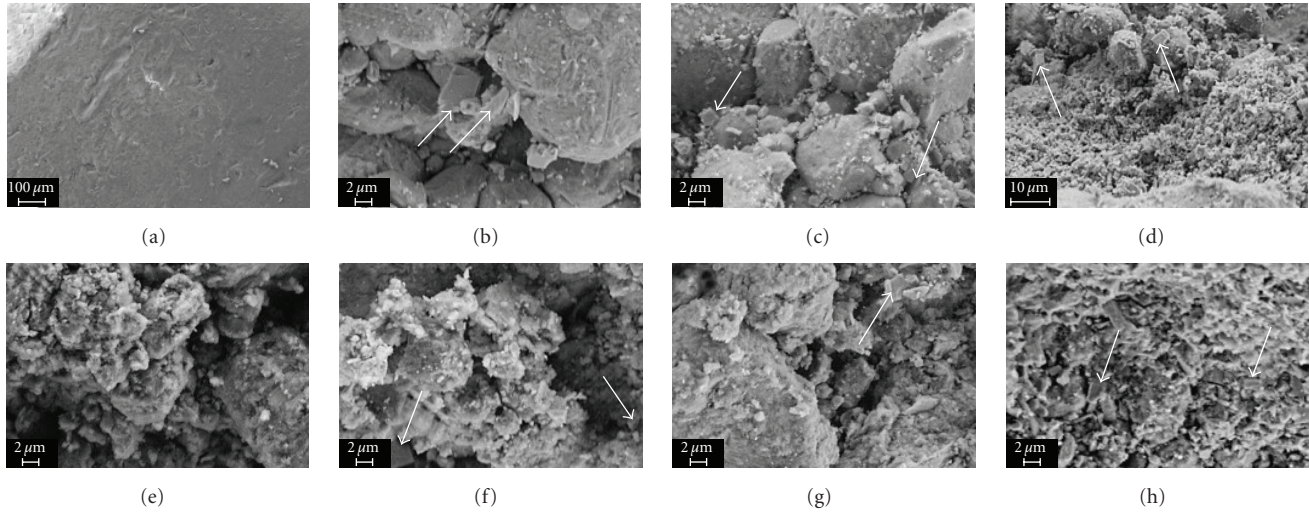


FIGURE 8: High magnification SEM micrographs for the micro (a)–(d) and nanoscale (e)–(h) green matrices reinforced with 0, 5, 10, and 20 wt% TiC, respectively. Arrows point at TiC particles.

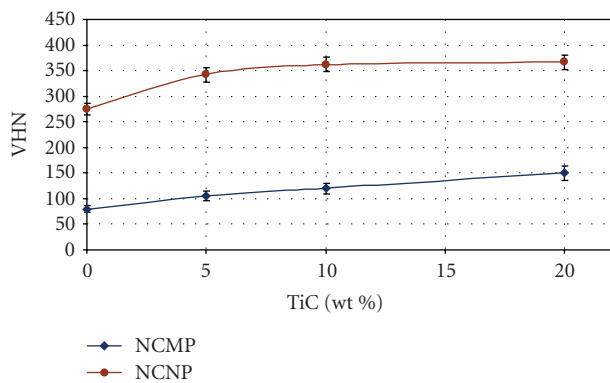


FIGURE 9: A graph showing the Effect of TiC addition on the microhardness for the as-received micron and nanopowder consolidated HC.

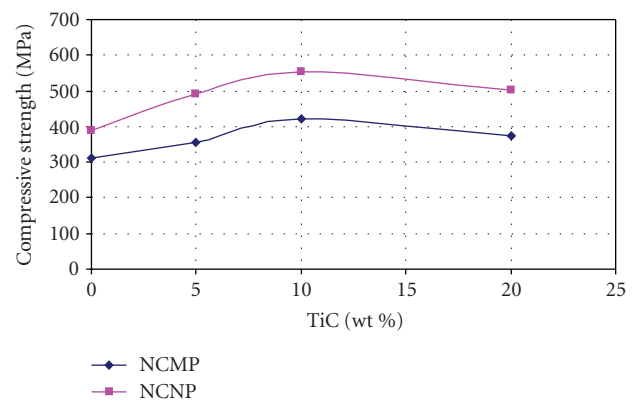


FIGURE 10: Compressive strength of HC micro and nanopowder consolidates as a function of TiC additions.

343%. Similar observations were made by Chen et al., on nanocrystalline NiAl milled powders [20]. Addition of 5 wt% TiC to the nanopowder HC resulted in a 124% increase in hardness of the monolithic one compared to an increase of 132% for the micronpowder HC. Increasing the TiC-content beyond 5 wt% did not result in a noticeable increase in hardness, especially for the nanopowder compacts, while a gradual increase in hardness was observed for the micronpowder matrix reinforced with up to 20 wt%.

The compressive strength measured for the AA2124/TiC composite materials obtained by hot compaction for the micro and nanopowder compact matrices with and without TiC reinforcement is displayed in Table 2 and Figure 10. It is observed that refinement of the micronpowder to the nanoscale level by ball milling produced hot compact discs not only with significantly enhanced hardness values, but also with enhanced compressive strength. The nanopowder monolithic consolidates exhibited compressive strength of 388 MPa compared to 313 MPa for micronpowder one,

TABLE 2: Effect of TiC additions to the micron and nanopowder matrices.

| TiC wt% | Compressive strength (MPa) (micronpowder matrices) | Compressive strength (MPa) (nanopowder matrices) |
|---------|--|--|
| 0 | 313.66 | 389 |
| 5 | 357.84 | 493.23 |
| 10 | 415.55 | 538.57 |
| 20 | 373.65 | 507.47 |

which represents a 123% improved compressive strength. Addition of TiC nanostructured powder up to 20 wt% to the nanopowder consolidated matrix resulted in an average increase of 130% in compressive strength compared to that produced for the microscale one. From the diagram it is obvious that 10 wt% TiC produced the highest compressive strength for both matrices, which decreased with increasing the content up to 20 wt%.

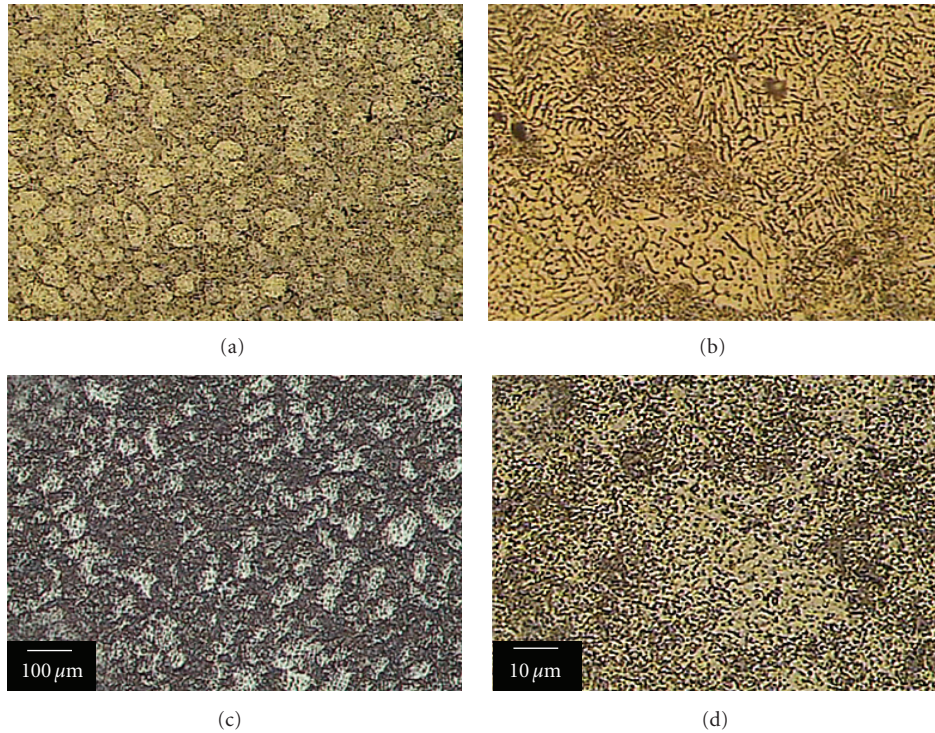


FIGURE 11: Optical micrographs at low and high magnifications showing the microstructure of the hot compact discs produced for the monolithic (a), (b) micronpowder and (c), (d) nanopowder HC AA2124.

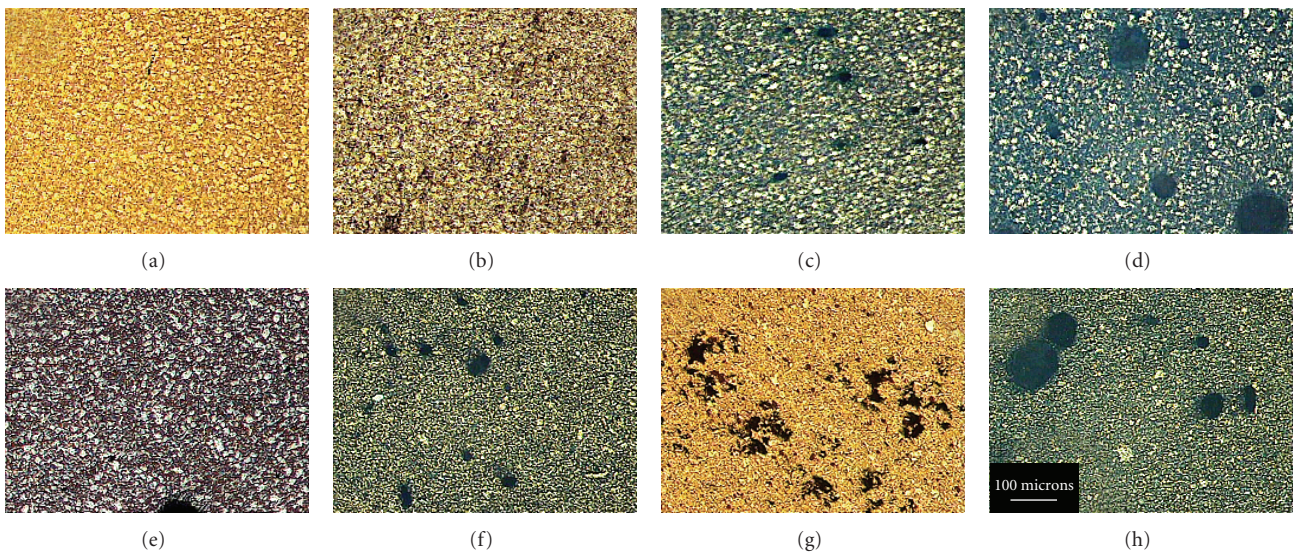


FIGURE 12: OM micrographs showing low magnification images for the (a)–(d) micronpowder 0, 5, 10, and 20%, and (e)–(h) nanopowder 0, 5, 10, and 20% consolidated HC matrices, respectively.

Investigation of the hot compacts microstructure at low and high magnification (Figure 11) explained the difference in VHN-values for both matrices. The consolidated micronpowder particle size was measured to be $<50\ \mu\text{m}$ (Figure 11(a)) for the grain size $2\ \mu\text{m}$ in average size (Figure 11(b)). On the other hand, the ultrafine structure size produced by hot compaction of the nanopowders was

not revealed by optical microscopy as shown in Figures 11(c), 11(d). This suggests the possibility of retaining the nanoscale internal structure but as well as the nanoscale refined powder produced by 24 hours of MT. High strain hardening and stored energy in the nanostructure induced by the prior high-energy ball milling explain the observed improvement in hardness and compressive strength over the

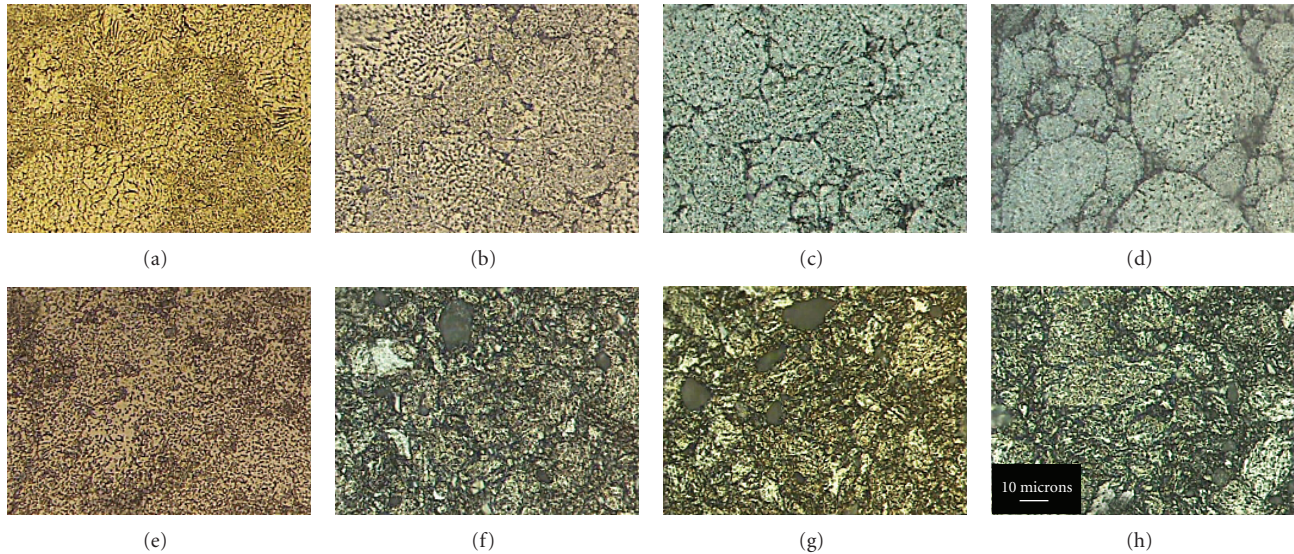


FIGURE 13: OM micrographs showing high magnification images for the (a)–(d) micronpowder 0, 5, 10, and 20%, and (e)–(h) nanopowder 0, 5, 10, and 20% consolidated HC matrices, respectively.

micronpowder consolidates. Additional investigations using transmission electron microscopy (TEM) is essential for the observation of the produced nanoscale structure along with the dislocation density after sintering.

Figure 12 shows the microstructural evolution as a function of TiC additions at magnifications images for the micron and nanopowder matrices, respectively. TiC-content increase within the micronpowder matrices above 5 wt% shows an increase in the voids size and volume fraction as shown in the low magnification images (Figures 12(c)–12(d)). For the nanopowder HC matrices, TiC addition even with 5 wt% resulted in the formation of isolated voids which coalesced into larger voids and cavities when TiC content increased to 10% and 20% as shown in Figures 12(e)–12(f). Cavity and void formation was persistent in both matrices, especially for the AA2124/20%TiC composite. It is suggested that the difference in thermal coefficient of expansion between the AA2124 matrices and the TiC resulted in the observed voiding during the cooling stage after HC.

Figure 13 shows that higher magnification images show an increase in preferential clustering of the reinforcement phase along the matrix particles' boundaries and triple points with the increase in TiC-content as shown in Figures 13(a)–13(d). Reinforcement segregation between the interstices of the relatively coarse micronpowder matrix particles during the compaction stage resulted in the formation of the reinforcement network particles along the matrix boundaries. The relative particle size (RPS) ratio of the matrix-to-reinforcement could be the cause of the observed segregation. Similar conclusions were depicted by Prasad et al. who investigated the effect of the RPS ratio of AA2124-to-SiC [6]. Their studies showed that lower RPS ratio results in enhanced distribution of the reinforcement phase within the matrix and hence results into higher densification and improved mechanical properties.

Comparing the reinforced nanopowder HC matrices (Figures 13(e)–13(h)) with that of the micronpowder one (Figures 13(a)–13(d)), it is clear that the TiC particles were uniformly distributed within the nanopowder matrix with no signs of clustering along the matrix boundaries or triple points. An extremely strained matrix kinking around the TiC particles is shown at higher magnifications in the areas free from voids and cavities. It is worth noting that RPS ratios of 45 : 1 and 8 : 1 were measured for the micronpowder and nanopowder HC matrices, respectively, compared to those of the TiC reinforcement. Many studies were conducted on the effect of RPS ratio on Al-base alloys reinforced with ceramic particles [6, 24, 25].

The observed intense matrix deformation around the TiC particles in addition to the strain hardening effect induced by ball milling of the matrix powder explains the exhibited increase in VHN values and compressive strength measured for the Nanopowder consolidated matrices compared to the micronpowder one. AA2124 is a precipitation-hardenable alloy that contains different kind of second phase particles most important of which is the Cu-rich phases which are responsible for the strengthening of the alloy on aging [1]. It is suggested that the diffusion mean free path of the Cu element is strongly affected by the reinforcement distribution within the matrix. The higher the RPS ratio, the higher the diffusion mean free path of Cu within the matrix which results in the segregation of the Cu rich phase within the reinforcement clusters and hence poor properties.

Further investigation is required to understand the consolidation behavior and deformation mechanism of the nanopowder matrix compared to the micropowder one with and without reinforcement. One of the major causes that might have contributed to the formed cavities is the problem of entrapped air pockets within the individual particles and agglomerates. The powder compaction stage was done

TABLE 3: Effect of aging at 175°C on peak aging time, hardness, and compressive strength.

| TiC (wt.%) | Micronpowder matrices | | | Nanopowder matrices | | |
|------------|-----------------------|-----|-----------------------|-----------------------|-----|-----------------------|
| | Peak aging time (min) | VHN | σ_{Comp} (MPa) | Peak aging time (min) | VHN | σ_{Comp} (MPa) |
| 0 | 560 | 190 | 377 | 530 | 305 | 458 |
| 5 | 430 | 195 | 453 | 360 | 365 | 540 |
| 10 | 300 | 220 | 508 | 270 | 375 | 636 |
| 20 | 190 | 242 | 464 | 180 | 425 | 624 |

in open air without the use of vacuum or inert gas. A much improved consolidation behavior is expected under controlled atmosphere. Moreover, metal forming after cold or hot compaction will without doubt increase density and hence enhance the mechanical behavior of the consolidated bulk specimens.

Investigation of the effect of aging time at 175°C was also investigated for the micron and nanopowder matrices in the monolithic and reinforced conditions. Table 3 shows the peak aging time for each condition as well as the exhibited VHN-values and compressive strength.

From Table 3, it is clear that increasing content of TiC to both matrices resulted in decreasing the peak aging duration from about 9 to 3 hours for the matrices reinforced with 0 up to 20 wt% TiC, respectively. On the other hand, the peak aging time recorded for the micron and nanopowder matrices was almost the same for all conditions. Peak aging increased the hardness of the as compressed micronpowder matrices (Figure 9) by an average of 188%, while increased that of the nanopowder matrices by an average of 110%. In addition, peak aging resulted in increasing the compressive strength of the micron and nanopowder matrices was 123% and 117% in average, respectively. This indicates that solution heat treatment at 500°C for 1 hour followed by peak aging at 175°C for hours did not result in the loss of the mechanical properties of the milled powders, but rather enhanced the mechanical properties. In order to explain the nanopowder mechanical behavior post solutionizing and aging structural evolution compared to that of the micronpowder matrices with and without reinforcement microstructural investigation is currently under investigation.

Comparing the continuously cast and rolled sheets of AA2124-T851 properties with those produced for the investigated 24 hours milled powder consolidates in the T6 temper condition, it is found that a hardness of 146 HV versus 309 HV is produced, respectively. In addition, the hot compact nanopowders reinforced with only 10 wt% TiC displayed compressive strength that is higher (636 MPa) than MMC of AA2124 micronpowder (75 μ m particle size) reinforced with either 10% BN or 15% Al₂O₃ processed by a combined cold uniaxial compaction followed by conventional extrusion at 480°C with an extrusion ratio of 3.25 : 1 [26]. This indicates a significant improvement in the load bearing capacity and durability of the fabricated Al-based nanocomposites, especially for applications that requires high performance at relatively high operating temperatures.

4. Conclusions

In the current paper, we have what follows.

- (1) Nanocrystalline-nanopowders <100 nm in particle size and 20 nm internal structural size were fabricated successfully by high-energy ball milling from a 40 μ m particle sized AA2124 powder with internal structure ranging between 53–300 nm in average size.
- (2) The consolidation behavior of the micro and nano consolidated matrices was characterized in the monolithic condition and with addition of TiC ceramic nanostructured particles.
- (3) The green compact densities of the nanoscale powder decreased to 92% compared to 97% for the micronpowder as-received powder. This was due to the resistance of the strain hardened agglomerates to the applied pressure used for compaction.
- (4) The degree by which the density decreased with the addition of 5 wt% TiC to the matrix was much lower for the nanoscale consolidated matrix compared to the micronpowder consolidated one due to the low RPS ratio between the matrix and the reinforcement, which promoted uniform distribution of the TiC particles within the matrix agglomerates.
- (5) Increasing TiC content up to 10 wt% results in the formation of large voids and cavities, which reduces the compressive strength of the produced compacts, although hardness increases with TiC addition regardless of the content.
- (6) Hardness and compressive strength increased by peak aging at 175°C for monolithic and composite consolidated nanostructured AA2124, which qualifies them for high performance load bearing light weight applications.
- (7) Based on the current research nanopowder of Al-alloys produced by 24 hours mechanical milling of gas atomized micronpowders reinforced with 10 wt% TiC is recommended for products suitable for high wear and erosion resistance applications.
- (8) Further investigation is required using TEM for microstructural analysis on the nanoscale level. In addition, investigation of the compressive strength of the produced compacts with and without heat treatment is also planned.

Acknowledgment

The authors of the work would like to acknowledge the Yousef Jameel Science and Technology Research Center (YJ-STRC) at the American University in Cairo, Egypt for the financial support of the current research.

References

- [1] J. C. Malas, S. Venugopal, and T. Seshacharyulu, "Effect of microstructural complexity on the hot deformation behavior of aluminum alloy 2024," *Materials Science and Engineering A*, vol. 368, no. 1-2, pp. 41–47, 2004.
- [2] V. V. Dabhade, T. R. Rama Mohan, and P. Ramakrishnan, "Sintering behavior of titanium-titanium nitride nanocomposite powders," *Journal of Alloys and Compounds*, vol. 453, no. 1-2, pp. 215–221, 2008.
- [3] J. Robertson, J.-T. Im, I. Karaman, K. T. Hartwig, and I. E. Anderson, "Consolidation of amorphous copper based powder by equal channel angular extrusion," *Journal of Non-Crystalline Solids*, vol. 317, no. 1-2, pp. 144–151, 2003.
- [4] S.-Y. Chang, K.-S. Lee, S.-H. Choi, and D. H. Shin, "Effect of ECAP on microstructure and mechanical properties of a commercial 6061 Al alloy produced by powder metallurgy," *Journal of Alloys and Compounds*, vol. 354, no. 1-2, pp. 216–220, 2003.
- [5] S. H. Hong and K. H. Chung, "Effects of vacuum hot pressing parameters on the tensile properties and microstructures of SiC-2124 Al composites," *Materials Science and Engineering A*, vol. 194, no. 2, pp. 165–170, 1995.
- [6] V. V. Bhanu Prasad, B. V. R. Bhat, Y. R. Mahajan, and P. Ramakrishnan, "Structure-property correlation in discontinuously reinforced aluminium matrix composites as a function of relative particle size ratio," *Materials Science and Engineering A*, vol. 337, no. 1-2, pp. 179–186, 2002.
- [7] Z. Z. Chen and K. Tokaji, "Effects of particle size on fatigue crack initiation and small crack growth in SiC particulate-reinforced aluminium alloy composites," *Materials Letters*, vol. 58, no. 17-18, pp. 2314–2321, 2004.
- [8] M. S. El-Eskandarany, "Mechanical solid state mixing for synthesizing of SiCp/Al nanocomposites," *Journal of Alloys and Compounds*, vol. 279, no. 2, pp. 263–271, 1998.
- [9] M. S. El-Eskandarany, "Structure and properties of nanocrystalline TiC full-density bulk alloy consolidated from mechanically reacted powders," *Journal of Alloys and Compounds*, vol. 305, no. 1-2, pp. 225–238, 2000.
- [10] M. S. El-Eskandarany, T. J. Konno, M. Omori, et al., "Formation of refractory WC compound by mechanical solid state reduction," *Journal of the Japan Society of Powder and Powder Metallurgy*, vol. 43, no. 11, pp. 1368–1373, 1996.
- [11] M. S. El-Eskandarany, T. J. Konno, M. Omori, et al., "Morphological and structural studies of mechanically alloyed Ti₄₄C₅₆ powders," *Metallurgical Transactions A*, vol. 27, p. 4210, 1996.
- [12] X.-M. He, W.-Z. Li, and H.-D. Li, "Therapeutic application of molecular adsorbents recirculating system (MARS) in chronic severe hepatitis patients complicated with multiorgan failure," *Journal of Materials Research*, vol. 9, p. 2355, 1994.
- [13] S. Xiang, K. Matsuki, N. Takatsuji, et al., "Microstructure and mechanical properties of PM 2024Al-3Fe-5Ni alloy consolidated by a new process, equal channel angular pressing," *Journal of Materials Science Letters*, vol. 16, no. 21, pp. 1725–1727, 1997.
- [14] Y. Kim and J.-C. Lee, "Processing and interfacial bonding strength of 2014 Al matrix composites reinforced with oxidized SiC particles," *Materials Science and Engineering A*, vol. 420, no. 1-2, pp. 8–12, 2006.
- [15] K. I. Elkhodary, H. G. Salem, and M. A. Zikry, "Equal channel angular pressing of canned 2124-Al compacts: processing, experiments, and modeling," *Metallurgical and Materials Transactions A*, vol. 39, no. 9, pp. 2184–2192, 2008.
- [16] H. G. Salem and M. Shamma, "Effect of the compaction parameters and canning material of nanostructured Al-powder consolidated via intense plastic straining process," in *Proceedings of the ASME 2nd Multifunctional Nanocomposites and Nanomaterials Conference and Exhibition (MN '08)*, pp. 129–142, Sharm El Sheikh, Egypt, January 2008, CD-ROM.
- [17] A. A. Sadek and H. G. Salem, "Construction of consolidation maps of Pre-ECAE hot compact nanocrystalline-micron powders," in *Proceedings of the ASME 2nd Multifunctional Nanocomposites and Nanomaterials Conference and Exhibition (MN '08)*, pp. 39–46, Sharm El Sheikh, Egypt, January 2008, CD-ROM.
- [18] B. Farrokh and A. S. Khan, "Grain size, strain rate, and temperature dependence of flow stress in ultra-fine grained and nanocrystalline Cu and Al: synthesis, experiment, and constitutive modeling," *International Journal of Plasticity*, vol. 25, no. 5, pp. 715–732, 2009.
- [19] Z. Lin, S. L. Chan, and F. A. Mohamed, "Effect of nano-scale particles on the creep behavior of 2014 Al," *Materials Science and Engineering A*, vol. 394, no. 1-2, pp. 103–111, 2005.
- [20] T. Chen, J. M. Hampikian, and N. N. Thadhani, "Synthesis and characterization of mechanically alloyed and shock-consolidated nanocrystalline NiAl intermetallic," *Acta Materialia*, vol. 47, no. 8, pp. 2567–2579, 1999.
- [21] G. W. Dieter, *Mechanical Metallurgy*, McGraw-Hill, New York, NY, USA, 3rd edition, 1990.
- [22] C. Suryanarayana and M. Norton, *X-Ray Diffraction: A Practical Approach*, Plenum Press, New York, NY, USA, 1998.
- [23] T. S. Srivatsan, B. G. Ravi, M. Petraroli, and T. S. Sudarshan, "The microhardness and microstructural characteristics of bulk molybdenum samples obtained by consolidating nanopowders by plasma pressure compaction," *International Journal of Refractory Metals and Hard Materials*, vol. 20, no. 3, pp. 181–186, 2002.
- [24] C. Raghunath, M. S. Bhat, and P. K. Rohatgi, "In situ technique for synthesizing Fe-TiC composites," *Scripta Metallurgica et Materialia*, vol. 32, no. 4, pp. 577–582, 1995.
- [25] K. Shin, D. Chung, and S. Lee, "The effect of consolidation temperature on microstructure and mechanical properties in powder metallurgy-processed 2XXX aluminum alloy composites reinforced with sic particulates," *Metallurgical and Materials Transactions A*, vol. 28, no. 12, pp. 2625–2636, 1997.
- [26] M. Haouaoui, I. Karaman, H. J. Maier, and K. T. Hartwig, "Microstructure evolution and mechanical behavior of bulk copper obtained by consolidation of micro- and nanopowders using equal-channel angular extrusion," *Metallurgical and Materials Transactions A*, vol. 35, no. 9, pp. 2935–2949, 2004.